# Molecular ordering of ionic liquids at a sapphire hard wall

A high energy x-ray reflectivity study

Heiko Schröder
Stuttgart, 2009
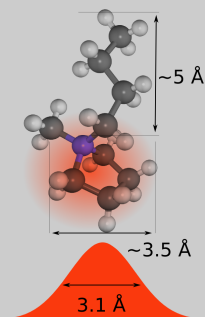
Max-Planck-Institut
für Metallforschung
Stuttgart
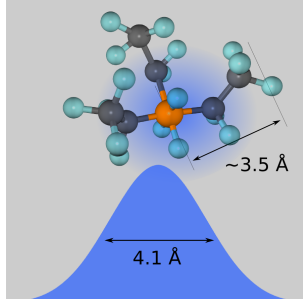
Institut für Theoretische
und Angewandte Physik
Universität Stuttgart

Molecular ordering of ionic liquids at a sapphire hard wall

A high energy x-ray reflectivity study

Vorgelegt von

HEIKO SCHRÖDER

aus Arnsberg, Westfalen

Preface

Ionic liquids are a fascinating materials class that finds more and more its way into today's and tomorrow's technological processes. This makes their interfaces with solid media a system of high technological and scientific relevance. To access such buried ionic liquid-solid interfaces is experimentally challenging, and only few experimental techniques are available. Over the last years, the Department Dosch at the Max Planck Institute for Metals Research has gathered outstanding experience in probing solid-liquid interfaces with high energy x-ray reflectivity. The objective of this thesis was to make use of this expertise to develop both an experimental setup and the analytical tools to elucidate the structure of ionic liquids at a charged sapphire hard wall. Owing to the vast number of available ionic liquids, one particular anion was chosen as the starting point for a systematic investigation of the interfacial structure on adjustable parameters, such as cation type, temperature, and doping concentration in binary mixtures with molecular solvents. I hope that the outcome of these efforts is a fruitful contribution towards a better understanding of ionic liquid interfaces and towards harnessing these liquids' intriguing properties in future applications.

The thesis is divided into four main parts that start after the German language summary. **Part I: On ionic liquids** acquaints the reader with ionic liquids and their interfaces in general, and with the investigated systems and the research focus in particular. **Part II: Technical and experimental details** summarizes the theoretical background in x-ray diffraction necessary for the understanding of the experimental methods, gives an overview over the sample environment, including the high energy x-ray setup at beamline ID15 at the European Synchrotron Radiation Facility (ESRF) in Grenoble, and discusses the data acquisition methods. **Part III: Results and discussion** is largely organized in two blocks, temperature-dependent cation variation and the impact of doping, after which the remaining results are briefly discussed. **Part IV: Conclusions** summarizes the main achievements of this work, draws conclusions, and gives an outlook on future research prospects.

Contents

Deutsche Zusammenfassung

Im Rahmen der vorliegenden Doktorarbeit wurde die Grenzfläche ionischer Flüssigkeiten (*ionic liquids*, IL) zu glatten Saphirsubstraten mittels hochauflösender Röntgenreflektometrie untersucht. Dank eines dafür optimierten Messaufbaus an der Europäischen Synchrotronstrahlungsquelle (ESRF) in Grenoble, Frankreich, konnten Ladungsdichteoszillationen auf molekularer Ebene beobachtet werden, die mehrere nm in das Volumen der Flüssigkeiten hineinreichen. Deren Abhängigkeit von verschiedenen Parametern wie Temperatur, Kationengröße oder Konzentration in binären Mischungen wurde systematisch bestimmt und so ein besseres Verständnis dieser Grenzflächenphänomene erlangt [1, 2].

Motivation

Ionische Flüssigkeiten gehören zu den meist erforschten Materialien der letzten Jahre. Sie grenzen sich begrifflich von herkömmlichen Salzschmelzen durch ihre niedrigen Schmelzpunkte unter $100°C$ ab[1], was sowohl ihre wissenschaftliche Ergründung als auch ihren Einsatz in industriellen Prozessen und technischen Anwendungen enorm erleichtert. Während es zu Beginn des vorigen Jahrhunderts erstmals gelang, Salze mit moderaten Schmelzpunkten zu synthetisieren [3], existieren heute Hunderte kommerziell erhältlicher ionischer Flüssigkeiten, die ihre niedrigen Schmelzpunkte zumeist der Einbindung organischer Strukturen in die Ionen verdanken. Das rege Interesse an ihnen rührt von ihrer rein ionischen Natur her, wodurch sie im Vergleich zu wässrigen Systemen eine Reihe außergewöhnlicher Eigenschaften besitzen und den Grenzfall einer elektrolytischen Lösung unendlicher Konzentration darstellen. Ionische Flüssigkeiten im allgemeinen zeichnen sich durch einen zu vernachlässigen Dampfdruck, einen großen flüssigen Temperaturbereich, gute Lösemitteleigenschaften, ihre intrinsische Leitfähigkeit und weite elektrochemische Fenster aus. Daraus leitet sich eine Vielzahl potentieller Anwendungen ab, von Elektrolyten in Brennstoffzellen zu Katalysatoren und Schmiermitteln (siehe auch Abb. 1.1). Ihre erstaunlichste Eigenschaft als Materialklasse ist allerdings ihre Vielseitigkeit: Die immense Anzahl denkbarer Kation/Anion-Kombinationen eröffnet die Möglichkeit, für bestimmte Anwendungen gezielt ionische Flüssigkeiten mit passenden Eigenschaften zu entwickeln. Da bei vielen Anwendungen Grenzflächen ionischer Flüssigkeiten zu Festkörpern eine wichtige Rolle spielen, könnte ein detailliertes Verständnis der

---

[1] Viele ionische Flüssigkeiten sind bereits unter normalen Umgebungsbedingungen flüssig. Im Englischen ist daher auch die Bezeichnung *room temperature ionic liquids* geläufig.

Grenzflächenstruktur und ihrer Abhängigkeit von äußeren Parametern entscheidend zum Durchbruch dieser faszinierenden Materialien auf einer Vielzahl technologischer Felder beitragen.

Material und Methoden

Röntgenreflektometrie ist ein ideales Werkzeug zur strukturellen Untersuchung glatter Grenzflächen. Gewöhnlich treffen Röntgenstrahlen in flachem Winkel auf eine Oberfläche, und die reflektierte Intensität wird in Abhängigkeit des vertikalen Impulsübertrags aufgezeichnet. Das Elektronendichteprofil senkrecht zur Oberfläche steht in direktem Bezug zur resultierenden Reflektivitätskurve und kann aus letzterer mittelbar über Inversionsalgorhythmen wie dem Parratt-Formalismus rekonstruiert werden. Im Falle verborgener fest/flüssig-Grenzflächen wie der ionischer Flüssigkeiten an Saphir muss jedoch zunächst das Volumen der Flüssigkeit von den Röntgenstrahlen durchdrungen werden, was den experimentellen Zugang aufgrund hoher Absorptionsverluste stark erschwert. Ein vom Max-Planck-Institut für Metallforschung in Kooperation mit der ESRF entwickeltes Präzisionsinstrument (*High Energy Micro-Diffraction* instrument, HEMD) ermöglicht mittels fokussierter, hochenergetischer Röntgenstrahlung erheblich höhere Signal-zu-Rauschen-Verhältnisse. In Verbindung mit den hohen Röntgenintensitäten, die eine moderne Synchrotronstrahlungsquelle der dritten Generation wie die ESRF zur Verfügung stellt, lassen sich so Strukturen im Bereich von wenigen Å auflösen.

Bei den Experimenten kam ein eigens dafür entwickelter Messaufbau zum Einsatz, der Messungen unter Vakuum bei Drücken bis $10^{-6}\,\mathrm{mbar}$ und in einem Temperaturbereich von ca. $-60°\mathrm{C}$ bis $300°\mathrm{C}$ zuließ (siehe Abb. 5.4). Als Substrate wurden atomar glatte Al_2O_3-Plättchen ($6 \times 10 \times 0,33\,\mathrm{mm}^3$) verwendet, auf die die Flüssigkeiten unmittelbar vor den Experimenten mit Hilfe einer Eppendorf-Pipette aufgebracht wurden.

Sämtliche Messreihen dieser Arbeit wurden an einer Gruppe ionischer Flüssigkeiten durchgeführt, die auf einem speziellen Anion basieren: Tris(penatafluoroethyl)trifluorophosphat ($[\mathrm{fap}]^-$, siehe Abb. 3.2). In Vorabversuchen am Volumenkörper wies diese Gruppe die höchsten Streuquerschnitte im experimentell zugänglichen Bereich des Impulsübertrags auf, weshalb sie sich als Ausgangspunkt für eine systematische Parametervariation anbot. Neben den Auswirkungen von Temperaturänderungen auf die Grenzflächenstruktur wurde anhand von vier verschiedenen Kationen (Abb. 3.3) der Einfluss der Kationenart und der Länge von Seitenketten untersucht. Darüber hinaus wurden das Abschirmverhalten von Lösungsmitteln und atomaren Anionen jeweils in Abhängigkeit von ihrer Konzentration ermittelt und erforscht, ob elektrische Felder die Grenzflächenstruktur beeinflussen. Komplementär zu den Reflektivitätsmessungen wurden Röntgenstreudaten am Volumenkörper der Flüssigkeiten aufgenommen und Aufladungseffekte an der Grenzfläche mittels eines kombinierten Röntgen/Kelvinmethode-Experiments analysiert.

Ergebnisse und Diskussion

Die Reflektivitätsdaten sämtlicher IL/Saphir-Grenzflächen weisen Strukturen auf, die für eine Lagenbildung senkrecht zur Grenzfläche charakteristisch sind. Um diese Beobachtungen quantifizieren zu können, wurde ein Lagenmodell zur Parametrisierung des Elektronendichteprofils senkrecht zur Grenzfläche entwickelt. Eine Parameteranpassung ergab physikalisch plausible Werte bei exzellenter Übereinstimmung mit den Daten. Alle untersuchten Systeme weisen demnach eine ausgeprägt oszillierende Lagenstruktur aus alternierenden Kationen- und Anionenlagen auf, die mit einer Kationenlage beginnt und exponentiell Richtung Volumenkörper abklingt. Sowohl steigende Temperaturen als auch steigende Lösungsmittelkonzentrationen führen zu einer Abnahme der Grenzflächenordnung.

Im folgenden wird eine Übersicht über die einzelnen Reflektivitätsstudien und übrigen Experimente gegeben.

Strahlungsinduzierte Effekte

Der Einfluss von Strahlungseffekten auf die Grenzflächenstruktur wurde gründlich untersucht. Eine wiederholte Aufnahme von Messkurven entlang derselben Substratfläche führte zu einem Ausschmieren der charekteristischen Strukturen in den Reflektivitätsdaten, was auf eine strahlungsinduzierte, lateral zufällig verteilte Zerstörung der Interferenzmuster hindeutet. Die Veränderungen in den Reflektivitätskurven folgen einer exponentiellen Sättigungsfunktion mit einer Zeitkonstante in der Größenordnung von $10^2\,$s bis $10^3\,$s – abhängig sowohl vom System als auch von der Temperatur. Allerdings handelt es sich um einen stark lokalisierten Strahlenschaden, der sich nicht in noch unbestrahlte Regionen der Grenzfläche ausbreitet. Daher konnten mithilfe eines sorgfältig abgestimmten Messprotokols Einflüsse auf die akquirierten Daten vermieden werden.

Davon unabhängig durchgeführte *in situ*-Kelvinmethodenmessungen der Saphiroberfläche mit und ohne Bestrahlung wiesen einen starken Aufladungseffekt des Röntgenstrahls nach: Sowohl an Luft als auch mit ionischer Flüssigkeit bedeckt verringerte sich das Oberflächenpotential des Substrats unmittelbar nach Beginn der Bestrahlung merklich, was auf eine strahlunsinduzierte negative Oberflächenladung hindeutet.

Der Einfluss von Kationenart und Temperatur auf die Grenzflächenordnung

Insgesamt vier verschiedene Kationen wurden in Verbindung mit dem [fap]$^-$-Anion untersucht: Zwei Imidazolium-basierte, [hmim]$^+$ und [c$_{18}$mim]$^+$, ein Pyrrolidinium-basiertes, [bmpy]$^+$, und ein vierfach substituiertes Ammonium-Ion, [tba]$^+$. Drei davon, [bmpy]$^+$, [hmim]$^+$ und [tba]$^+$, haben eine vergleichbare räumliche Ausdehnung, und die Reflektivitäten der entsprechenden ionischen Flüssigkeiten waren in sehr guter Übereinstimmung mit dem eigens entwickelten binären Lagenmodell, dem *binary distorted crystal model*. Letzteres beschreibt die lateral gemittelten Elektronendichteprofile der Anionen und Kationen als Gaußverteilungen, deren Standardabweichungen mit zunehmender Entfernung von der Grenzfläche zunehmen. Daraus folgend ergeben sich für das gesamte Dichteprofil

der Flüssigkeit exponentiell gedämpfte Ladungsdichteoszillationen senkrecht zur Grenz-
fläche. Obwohl auch andere Ansätze auf Konsistenz mit den Messdaten überprüft wurden,
konnte die Grenzflächenstruktur eindeutig auf symmetrisch angeordnete, alternierend ge-
ladene Lagen zurückgeführt werden, wobei die erste Lage an der Grenzfläche stets positiv
geladen ist. Die Grenzflächenordnung zerfällt auf einer Längenskala von ein bis zwei Dop-
pellagenabständen und reicht einige nm in den Volumenkörper der Flüssigkeiten hinein.
Moleküldynamiksimulationen ionischer Flüssigkeiten an geladenen Grenzflächen gelan-
gen genauso wie um kurzreichweitige Wechselwirkungen erweiterte feldtheoretische An-
sätze zu ähnlichen Strukturen, wohingegen die klassische Poisson-Boltzmann-Theorie die
beobachteten Phänomene nicht erklären kann.

Das vierte Kation, $[c_{18}mim]^+$, weist eine von der der anderen drei stark abweichende
Geometrie auf. Seine viermal längere Seitenkette trennt es in einen geladenen Imidazolium-
Teil („Ringteil") und eine elektrisch neutrale Seitenkette („Rumpfteil") auf, weshalb es
kaum plausibel wäre, das Kation mit einer einzigen Gaußverteilung zu beschreiben. Dem-
entsprechend erwies sich der obige Modellansatz als unzureichend, um die Daten anzu-
passen. Allerdings konnten die am stärksten ausgeprägten Strukturen in der Reflektivitäts-
kurve zufriedenstellend mit einem erweiterten Modell reproduziert werden, das den Rumpf-
teil des Kations als homogene Hintergrundlage beschreibt und eine Asymmetrie zwischen
den geladenen Gaußverteilungen zulässt. Obwohl dieser grobe Ansatz die intramolekula-
re Struktur innerhalb des Kations nicht berücksichtigt, gewährt er doch Einblicke in die
generische Anordnung hoch anisotroper ionischer Flüssigkeiten an festen Grenzflächen.
So stimmt der Abstand zwischen den geladenen Ebenen senkrecht zur Grenzfläche un-
gefähr mit den entsprechenden Abständen bei den anderen drei ionischen Flüssigkeiten
überein, was ihrer strukturellen Verschiedenheit zum Trotz auf gleichartige und ähnlich
starke Ladungskopplungsmechanismen in allen vier Systemen schließen lässt.

Ein Temperatureffekt wurde lediglich bei der $[bmpy]^+$-basierten Flüssigkeit beobach-
tet. Hier nimmt mit steigender Temperatur die Zerfallslänge der Grenzflächenordnung li-
near um etwa 40% über einen Temperaturbereich von $125\,\mathrm{K}$ ab. Die induzierte Änderung
der Entropie ist dabei von vergleichbarer Größe wie die Energiedifferenz zwischen zwei
strukturell völlig verschiedenen Pyrrolidiniumkonformern, weshalb Verschiebungen im
Gleichgewicht zwischen diesen Konformern als Auslöser für die entropiebedingte Abnah-
me an Grenzflächenordnung plausibel erscheint. Ausgehend von Näherungen erster Ord-
nung für die Kapazität der elektrischen Doppellage (EDL) könnte der Temperatureffekt
– in Übereinstimmung mit Voltametriestudien – einem Anstieg der EDL-Kapazität zuge-
ordnet werden. Dem widerspricht allerdings, dass für das Imidazolium-Kation ähnlicher
Größe, $[hmim]^+$, kein vergleichbarer Temperatureffekt beobachtet werden konnte. Eine
heuristische Erklärung für das unterschiedliche Temperaturverhalten ist das Fehlen ähn-
licher konformaler Änderungen bei $[hmim]^+$. Dies unterstreicht die Bedeutung sterischer
Effekte auf die Grenzflächenordnung.

Die Streuexperimente am Volumenkörper weisen auf eine hohe Korrelation zwischen
den Lagenabständen an der Grenzfläche und den am stärksten ausgeprägten Volumenkor-
relationen der ionischen Flüssigkeiten hin. Folglich erscheint die Ordnung an Grenzflä-
chen größtenteils bestimmt durch Volumeneigenschaften. In Übereinstimmung mit dem

Temperaturverhalten an Grenzflächen zeigte auch bei den Volumenkorrelationen lediglich das [bmpy]$^+$-basierte System einen über die thermische Ausdehnung hinausgehenden Temperatureffekt. Die Verbreiterung des entsprechenden Korrelationssignals mit steigender Temperatur ist dabei vergleichbar mit der Abnahme an Grenzflächenordnung über denselben Temperaturbereich.

Abschirmeffekte in binären Mischungen

Zwei unterschiedliche Ansätze wurden verfolgt, um den Einfluss von elektrostatischer Abschirmung auf die Ordnung an IL-Grenzflächen zu untersuchen: Zum einen wurden Mischungen mit zwei verschiedenen Lösungsmitteln, Propylencarbonat (PC) und Triethylenglykol (TEG), in Abhängigkeit von der Lösungsmittelkonzetration untersucht, zum anderen wurden unterschiedlich hohe Anteile des [fap]$^-$-Anions mit atomaren Pendants ersetzt. Beide Ansätze führten in ihrer Tendenz zu einer Abschwächung der Lagenstrukturen in den Reflektivitätsdaten; allerdings waren lediglich die Lösungsmittel-Datenreihen von ausreichender Konsistenz, um eine notwendige Erweiterung des Strukturmodells sinnvoll zu verifizieren. Eine Einbindung der Lösungsmittel als homogen verteilte konstante Lage senkrecht zur Grenzfläche führte ohne die Einführung neuer Paramter zu einer Anpasung, die in hervorragender Übereinstimmung mit den Messdaten ist. Eine erhöhte Lösungsmittelkonzetration innerhalb der ersten Doppellage führte dabei nicht zu einer Verbesserung der Anpassung, was auf sogenannte *overscreening*-Effekte als Hauptauslöser für die beobachteten Ladungsdichteoszillationen hindeutet.

Da sowohl die Ordnungsstärke als auch der Lagenabstand mit zunehmender Lösungsmittelkonzentration abnehmen, scheinen sich die Lösungsmittelmoleküle bevorzugt innerhalb der ionischen Lagen anzuordnen und so identisch geladene Ionen voneinander abzuschirmen. Dies hat eine Schwächung der Ionenassoziation und damit der Ordnungsstärke zur Folge. Zur gleichen Zeit verringert die Coulomb-Anziehung zwischen den gedehnten Ionen den Abstand benachbarter Ionenlagen zueinander. Parallel zur Ordnung an der Grenzfläche nehmen auch die Korrelationen im Volumen der Mischungen mit steigender Konzentration ab, ohne sich jedoch räumlich auszudehnen, was konsistent zu Simulationsergebnissen ist, die eine Aggregation von Lösungsmittelmolekülen innerhalb des Ionennetzwerks ohne Ausbildung eigener Strukturen voraussagen. Anders als in Simulationen beobachtet liefert die lineare Abnahme der Ordnungsstärke aber keine Hinweise auf die Existenz verschiedener Lösungsstadien (*solvation regimes*).

Den strukturellen Unterschieden zum Trotz konnte das erweiterte Modell auf beide Lösungsmittelsysteme angewendet werden. Es erscheint daher plausibel, dass die beobachteten Abschirmungsphänomene generische Mechanismen repräsentieren. Die verschieden starke Abschirmkraft von PC und TEG hebt allerdings auch die wichtige Rolle von sterischen und lokalen Effekten hervor. Der bei weitem stärkere Einfluss von TEG auf die Grenzflächenstruktur rührt wahrscheinlich von dessen stangenartiger Form mit alternierenden polaren und unpolaren Stellen her, die eine Einbindung in das Ionennetzwerk der ionischen Flüssigkeit erschwert.

Fazit

Hochauflösende Röntgenreflektometrie ermöglichte es, die verborgene Grenzfläche ionischer Flüssigkeiten an Saphir mit vormals unerreichter Auflösung zu vermessen. Faszinierende Eigenschaften der Grenzflächenordnung von $[fap]^-$-basierten ionischen Flüssigkeiten an einer geladenen Wand konnten offengelegt werden, so zum Beispiel die Ausbildung alternierender Anionen- und Kationenlagen, die mehrere nm in den Volumenkörper hineinreichen. Da die Ergebnisse dieser Arbeit den ersten verlässlichen Nachweis von statischen Ladungsdichteoszillationen ionischer Flüssigkeiten an geladenen Oberflächen darstellen, liefern sie wertvolle Eingaben hin zu einem besseren theoretischen Verständnis der elektrischen Doppellage in unverdünnten ionischen Systemen.

Die Reichweite und Art der beobachteten Lagenstrukturen wiesen trotz der strukturell völlig verschiedenen Kationen charakteristische Übereinstimmungen bei allen vier untersuchten ionischen Flüssigkeiten auf. Daher ist davon auszugehen, dass es sich bei dieser Lagenbildung um eine generische Eigenschaft komplexer ionischer Flüssigkeiten an Grenzflächen handelt. Allerdings zeigt das auf konformelle Differenzen zurückgeführte unterschiedliche Temperaturverhalten die Bedeutung sterischer Effekte für die Strukturen sowohl an Grenzflächen als auch im Volumenköper auf. Gleiches gilt für die Abschirmkraft von Lösungsmitteln in binären Mischungen.

Zwar gewähren die lateral gemittelten Dichteprofile keine Einblicke in lokale Wechselwirkungen auf Molekülebene; dafür bieten sie aber einen experimentellen Bezugspunkt bei der Validierung von zukünftigen Simulationen und könnten so dabei helfen, neue Molekülpotentiale zu entwickeln, die es schlussendlich erlauben, die den Beobachtungen zugrundeliegenden Mechanismen auf molekularer Ebene abzubilden.

Resümierend lässt sich sagen, dass ionische Flüssigkeiten an geladenen Oberflächen komplexe Ordnungsphänomene zeigen und die systematische Variation von verschiedenen Parametern einen Zugang bietet, die zugrundeliegende Physik auf molekularer Ebene zu ergründen. Die stetig zunehmende Zahl kommerziell erhältlicher ionischer Flüssigkeiten erlaubt es in zunehmendem Maße, spezifische Aspekte der Ordnung an Grenzflächen zu untersuchen. Dies wird in Verbindung mit Molekulardynamiksimulationen derselben Systeme und neuen theoretischen Ansätzen zu einer Vertiefung unseres Verständnisses ionischer Flüssigkeiten an Grenzflächen führen und eine Triebfeder bei der Entwicklung neuer Anwendungen sein. Die Ergebnisse dieser Arbeit stellen einen Schritt in diese Richtung dar.

Part I

On ionic liquids

Chapter 1

Introduction

Ionic liquids, or room temperature ionic liquids (RTILs), constitute one of the most widely investigated materials groups today, their enormous range of possible applications fascinating both academic and industrial researchers around the world. This chapter is meant to introduce the reader to the world of these peculiar liquids. First, a short account on the history of ionic liquids from conventional high temperature molten salts towards the development of highly functionalized 3rd generation RTILs is given, before some of their most intriguing properties along with promising applications are reviewed.

1.1   History of molten salts

There are several definitions of what it takes to be an ionic liquid. Literally, every liquid with solely ionic constituents is an ionic one, thus including molten inorganic salts like alkali halides with melting points typically above 600°C. Nowadays, the most widely used definition considers salts with an organic cation and melting points below the boiling temperature of water as ionic liquids. I will stick to this convention throughout this work with the expressions ionic liquid and room temperature ionic liquid being mutually exchangeable.

Liquids of purely ionic nature have intrigued both scientists and engineers ever since for their vastly differing properties in contrast to aqueous or molecular systems. Aside from different interactions and bonding forces, they also constitute an electrolyte solution of infinite concentration giving them superior performance in electrochemical processes. For high temperature molten salts, the high melting points several hundred kelvin above room temperature limited both their scientific investigation and their incorporation in technological applications such as energy storage in battery devices. This problem set ground for scientists to come up with low melting salts, e.g. by including organic ionic species. In 1914, the first synthesis of an ionic liquid by modern definitions, ethylammonium nitrate ($[EtNH_3]^+[NO_3]^-$), was reported [3]. Although it is widely agreed upon as the starting point of the new materials class of ionic liquids, this paper did not receive much resonance in the scientific world at its time. The thread was taken up again in 1948 when first

applications for aluminum chloride-based ionic liquids were patented [4]. It was shown that compositions of $AlCl_3$ and 1-alkylpyridinium bromide ($[C_npy]^+Br^-$) have a small room temperature liquidus window for certain concentrations of $AlCl_3$. In the following decades, considerable research efforts were put into organic chloride-aluminum chloride ionic liquids [5, 6] which can be regarded as the first generation of ionic liquids [7].

By then, many electrochemists were fully aware of these liquids' versatile potential. Due to their hygroscopic nature, however, they are difficult to prepare, which ultimately prevented their broad usage in possible applications. Therefore, it was not before the synthesis of air and water stable ionic liquids in 1992 [8] that interest in them was virtually exploding. Based on an imidazolium cation, 1-alkyl-3-methylimidazolium ($[C_nmim]^+$), and either hexafluorophosphate ($[PF_6]^-$) or tetrafluoroborate ($[BF_4]^-$) as anion, these systems can be seen as the second generation of ionic liquids. Although they can generally be prepared and stored outside of an inert atmosphere, long time exposure can drastically change their properties, for both $[PF_6]^-$ and $[BF_4]^-$ decompose in the presence of water under formation of HF [9]. To avoid such undesired reactions with water, some both more hydrophobic and more complex anions have received considerable attention in recent years, such as trifluoromethanesulfonate ($[CF_3SO_3]^-$), bis{(trifluoromethyl)-sulfonyl}amide ($[NTf_2]^-$), and tris(pentafluoroethyl)-trifluorophosphates ($[fap]^-$) [1]. Ionic liquids comprised of these anions can be regarded as the third and most recent generation. The "next generation" ionic liquids yet to come are believed to be task-specific, i.e. optimized for dedicated applications.

1.2   Macroscopic properties and applications

1.2.1   Physiochemical properties

The most striking property of ionic liquids as a group is probably their versatility. There is an almost infinite number of possible cation/anion combinations, giving us the possibility to fine-tune an ionic liquid's properties, e.g. by variation of the size ratio, incorporation of functionalized groups, or changing the length of side chains. With a better understanding of the correlations between structure and properties the vision of ionic liquids as application-matched designer solvents could finally come true.

Despite the heterogeneity of all ionic liquids synthesized to date, most of them share common physio-chemical properties such as higher densities than water, typically between 1 and $1.6\,\mathrm{g\,cm^{-3}}$. Some of these properties are of high relevance for applications.

Broad liquidus range

The liquidus range of ionic liquids is of the same order as for most high temperature molten salts, i.e. several hundreds kelvin, and in consequence broader than for any molecular liquid –just shifted towards lower melting points. The latter mainly arise from a

---

[1] The research focus of this work is centered around the $[fap]^-$ anion.

reduction of the ionic bonding strength. The incorporation of organic material inside the ions increases the spatial distance between the charges, hence diminishing the Coulomb interaction strength.

For $[C_n mim]^+[anion]^-$ ionic liquids of different side chain lengths, up to $n = 4$, a melting point reduction was observed, whereas for higher n the melting point rose [10]. This highlights the competition between symmetry and mobility in their impact on the melting points. Increasing asymmetry lowers the melting point as long as the cost in mobility is not getting too high. Although low melting points are crucial for economic industrial processes, it still remains difficult to reliably predict them. Attempts have been made using *quantitative structure-property relationships* (QSPR) [11] and thermodynamic cycles [12] to derive an ionic liquid's melting behavior. Even for known systems, a precise determination of the melting point often proves to be difficult due to glass formation in a supercooled state.

Tunable solvent properties

The global solvation capability of a solvent is mostly defined by its polarity. For molecular liquids, polar solutes tend to dissolve in polar solvents and vice versa. Ionic liquids exhibit more complex solvation properties. Being highly polar in general, their solvation behavior with respect to different solutes can be changed drastically by ion replacement. Features like H-bond acceptance/donation and $\pi - \pi$ or $C - H \cdots \pi$ interactions may be tuned individually. In this way ionic liquids can act as very selective solvents, e.g. dissolving an organic compount completely while phase-seperating with water.

Negligible vapor pressure and high thermal stability

For all technical purposes, ionic liquids do have a negligible vapor pressure and are practically non-flammable, even at elevated temperatures. Hence, the far end of the liquidus range is defined by the liquid's decomposition temperature which is mostly influenced by the strength of incorporated heteroatom-carbon and heteroatom-hydrogen bonds [13]. Even though thermal stabilities up to $500\,°C$ have been reported [14], long time exposure to such temperatures leads to decomposition in most cases. In this work, thermal effects were observed for the ionic liquid $[bmpy]^+[fap]^-$ after several hours of exposure at $160\,°C$ despite a reported decomposition temperature above $300\,°C$ [15] (compare Sec. 6.1).

Broad electrochemical window

One key feature of ionic liquids is their broad electrochemical window, defined as the electrochemical potential range over which an electrolyte is neither reduced nor oxidized at an electrode. In most cases, this window is a multiple of the electrochemical window of water of $1.2\,V$, e.g. $4.1\,V$ for $[bmim]^+[BF_4]^-$ and $5.5\,V$ for $[bmp]^+[NTf_2]^-$ at a glassy carbon electrode [16, 17]. $[fap]^-$-based ionic liquids exhibit exceptionally broad electrochemical windows of $5.5\,V$ and more [18].

Moderate viscosity and high electrical conductivity

Viscosity and electrical conductivity are two closely related properties in purely ionic systems, for both depend on the mobility of the ions. Already in 1931, it was empirically found that the product of the molar conductivity and the viscosity for molten salts is constant [19]. Being typically two or three orders of magnitude above the viscosity of water, high viscosities are one of the major limiting factors for the large-scale use of ionic liquids. They slow down chemical reaction rates, decrease the ion mobility in these, and alter the mechanical properties of the fluids. Therefore, it has become an important objective to synthesize new ionic liquids with reasonably low viscosities without losing their other remarkable properties. To date, the lowest viscosity at room temperature reported for an ionic liquid is $21\,\mathrm{mPas^{-1}}$ (as compared to $1\,\mathrm{mPas^{-1}}$ for water and $81\,\mathrm{mPas^{-1}}$ for olive oil [20]). With increasing temperature the viscosity of ionic liquids decreases much stronger than for simple liquids. In contrast to the latter, the viscosity of ionic liquids does not obey an Arrhenius law, but is given by the Vogel-Fulcher-Tammann equation [21].

Unlike viscosity the electrical conductivity poses no significant obstacle towards application. For low viscosity ionic liquids, it is already at room temperature up to $\sigma = 10^{-2}\mathrm{Scm^{-1}}$ and thus in the range of conductivities of many widely used electrolytes in electrochemistry. In combination with their superior electrochemical windows, this makes ionic liquids a driving factor for new electrochemical processes [7]. As mentioned above, the conductivity of a molten salt is inversely proportional to its viscosity, hence it increases exponentially with increasing temperature, obeying the same Vogel-Fulcher-Tammann equation. According to the Nernst-Einstein relation [22], the molar conductance, $\Lambda = \sigma/C$, is linearly correlated to the sum of the self-diffusion coefficients of the ions (with C the molar concentration, F the Faraday constant, and R the gas constant):

$$\Lambda_{NE} = \frac{F^2}{RT}\left(D_{cation} + D_{anion}\right) \tag{1.1}$$

If all ions would contribute to the conductance, this equation would hold rigorously. For ionic liquids, this is generally not the case, i.e. $\Lambda_{IL} < \Lambda_{NE}$ – a fact assigned to the temporal presence of electrically neutral ion pairs. Often only half the ions contribute to the conductance [23]. The question of pair formation and their life time is subject of many studies and still causes controversion [10].

1.2.2   Fields of application

All these remarkable properties make ionic liquids very promising candidates for a broad range of applications, from electrolytes in high-performance fuel cells [24] and catalysts in the production of dye solar cells [25, 26] to lubricants and thermal fluids [27, 28]. In many areas, ionic liquids prove to be innovative driving factors, breaking ground for technological advances unaccessible before, e.g. in low temperature electrodeposition of many metals [29], towards low-power, fast switching organic field effect transistors [30], or in the development of safe and sustainable battery electrolytes [31].
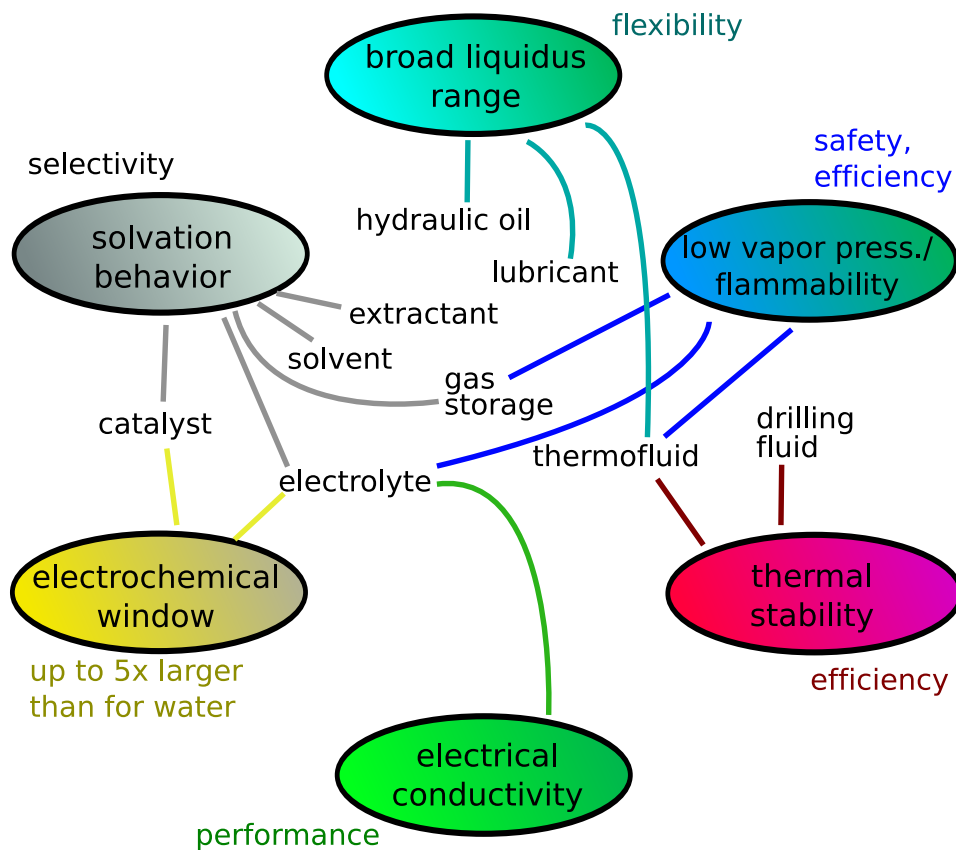
Figure 1.1: Important properties of ionic liquids and their correlation to possible fields of applications.

The use of ionic liquids is not limited to new tehnologies. For virtually every process liquid, some ionic liquid as outperforming replacement could be found given a better understanding of the interplay between structure and properties. Even if we get there, however, ionic liquids will always cost a multiple of plain molecular liquids. So particularly on an industrial scale, the technological and efficiency benefits have to exceed the additional costs for marketable applications involving ionic liquids.

Finally, it should be pointed out that, although many of the afore-mentioned applications are still to be implemented on an industrial scale, ionic liquids are already used in some processes today. Figure 1.1 correlates some fields of application with the unique properties discussed above. It is far from being exhaustive and only intended to outline the potential of ionic liquids. More comprehensive reviews and detailed descriptions of today's and future applications can be found elsewhere [32–34].

Chapter 2

Ionic liquids at interfaces

Many of the technological applications of ionic liquids presented at the end of the previous chapter involve processes at interfaces with other media. Therefore, a detailed understanding of the interfacial structure is an important factor for improving existing applications and developing new ones. In this chapter, the reader is introduced to the fundamental interactions on the molecular level, followed by a brief discussion of bulk correlations, before possible structural arrangements of ionic liquids at interfaces and their dependence on specific paramters are covered in more detail. It concludes with a summary of studies on the interfacial structure of ionic liquids.

2.1   Physical interactions on the molecular level

On the molecular level, the constituents of a liquid interact with each other in various ways. Omitting gravitational effects, these interactions are either of electrostatic (charged particles, direct and induced dipoles) or of quantum mechanical origin (dispersion, Born repulsion) or arise from a mixture of both (H-bonding). In consequence of the structural complexity of ionic liquids, the interplay of these interactions is difficult to understand and the total effective intermolecular potential not to be obtained in a straight-forward fashion.

2.1.1   Electrostatic interactions

Electrostatic interactions arise between stationary electric charges and are described by the Coulomb interaction potential. For two point charges, q_1 and q_2, at distance r in a medium of relative permittivity, ϵ_r, the interaction potential reads

$$V(r) = \frac{q_1 q_2}{4\pi\epsilon_0\epsilon_r r} \tag{2.1}$$

Coulomb interactions are responsible for the cohesion between the ions in solid salts such as NaCl and in ionic liquids. The latter, however, incorporate organic compounds in one or both of the ions that enlarge the charge separation, hence reducing the melting point

21

below room temperature. In addition, the charges are screened by an increased relative permittivity, further reducing the effective potential.

Ion-ion interactions are by far the strongest Coulomb interactions within ionic liquids but not the only ones. Wherever charge neutrality is perturbed locally, Coulomb interactions affect the overall potential. In case of permanent or induced dipoles, this yields significant contributions [1]. A molecule has a dipolar moment if it has a charge imbalance, i.e. the centers of mass positions for the positive and the negative charges do not coincide. It is defined as

$$\overrightarrow{\mu} = \delta \overrightarrow{l} \tag{2.2}$$

with $\overrightarrow{l} = \overrightarrow{\delta^+} - \overrightarrow{\delta^-}$ the distance between the effective charges within the molecule, δ^+ and δ^-, and $\delta = |\delta^+| = |\delta^-|$. In the vicinity of other charges, such effective charges experience Coulomb potentials that depend on the dipole's relative orientation. For single ion-dipole interactions, they are preferentially placed in line with the ion with the effective charge of opposite sign placed in the middle. Applying the Boltzmann weighting factor and the potential energy distribution theorem [35], one obtains for $kT > (q\mu/4\pi\epsilon_0\epsilon_r r^2)$ the angle-averaged potential energy

$$V_{i-d}(r) = -\frac{q^2\mu^2}{6(4\pi\epsilon_0\epsilon_r)^2 kT r^4} \, . \tag{2.3}$$

Similarly, the interaction potential between two dipolar molecules can be obtained:

$$V_K(r) = -\frac{\mu_1^2\mu_2^2}{3(4\pi\epsilon_0\epsilon_r)^2 kT r^6} \, , \tag{2.4}$$

for $kT > (\mu_1\mu_2/4\pi\epsilon_0\epsilon_r r^3)$. This is also known as *Keesom interaction energy* [2].

The interaction potentials described so far originate from permanently separated charges, i.e. ions or permanent dipoles in polar molecules. Apart from these, electrostatic interactions also arise from induced dipoles: When a non-polar molecule is subjected to an electric field E, its electron cloud is displaced in order to minimize the potential energy. This results in an induced dipole moment $\mu_i = \alpha E$. In general, all molecules are polarizable in such a way – to which extend depends on the molecular polarizability α. The value of α varies strongly for different liquids and is an important parameter for their solvent properties ("like dissolves like"). For ion-induced dipole interactions, the interaction potential can be calculated as

$$V_{i-id}(r) = -\frac{q^2\alpha}{2(4\pi\epsilon_0\epsilon_r)^2 r^4} \tag{2.5}$$

In the general case of dipolar and non-polar molecules interacting with each other, Debye derived the following potential:

$$V_D(r) = -\frac{\mu_1^2\alpha_2 + \mu_2^2\alpha_1}{(4\pi\epsilon_0\epsilon_r)^2 r^6} \tag{2.6}$$

---

[1] Multipoles of higher order are not considered here. Ion-quadrupole interactions are proportional to r^{-8}, thus four orders of magnitude weaker than van der Waals forces.

[2] after Willem Hendrik Keesom

with μ_1, μ_2 the permanent dipolar moments of molecules 1, 2, and α_1, α_2 the respective molecular polarizabilities. These interactions are known as *Debye induced dipole interactions*. Together with the Keesom interactions mentioned above and the London dispersion interactions introduced in the following subsection, they share the same distance dependency r^{-6} and are summarized as *van der Waals interactions*.

2.1.2 Quantum mechanical interactions

Electrostatic considerations alone fail to explain the attraction between non-polar molecules and their repulsion at very short distances. Both phenomena have their origin in quantum mechanical effects. The attractive potential arises from high-frequency perturbations of the electron cloud of atoms or molecules causing them to carry a dipolar moment at any given time. Although these dipoles average out over very short times in case of non-polar molecules, they still give rise to an attractive interaction potential between two molecules depending on their polarizabilities α_1, α_2 and their oscillation frequencies ν_{01}, ν_{02} (usually of the order of 10^{-16}s^{-1}):

$$V_L = -\frac{3}{2} \frac{\alpha_1 \alpha_2}{(4\pi\epsilon_0\epsilon_r)^2 r^6} \left(\frac{h\nu_{01} h\nu_{02}}{h\nu_{01} + h\nu_{02}} \right) \tag{2.7}$$

The according interactions are called *London dispersion interactions* [3]. For most molecular liquids, they yield the most important contribution to the van der Waals potential. Only for strongly polar liquids, the orientational Keesom term might be of the same order.

At very short distances, Repulsion follows from the Pauli principle which states that electrons as Fermions cannot share the same quantum numbers. This produces a very steep and extremely strong repulsive potential at a distance where the outer electron shells of two approaching molecules start to overlap. It is called the hard core potential and obeys no general distance dependence but is often taken as proportional to r^{-12} in semi-empirical approaches. Combined with the van der Waals potential, the well-known Lennard-Jones pair interaction potential for non-polar molecules is obtained:

$$V_{LJ} = -\frac{A}{r^6} + \frac{B}{r^{12}} \tag{2.8}$$

2.1.3 Hydrogen-bonding interactions

The hydrogen-bonding interaction is a special type of Keesom interaction (dipole-dipole, Sec. 2.1.1) between two electronegative atoms, A and B, sharing a hydrogen atom, H, covalently bonded to one of them. The resulting hydrogen bond is directional and varies in strength from approx. $1\,\text{kJmol}^{-1}$ to approx. $40\,\text{kJmol}^{-1}$ with bond lengths ranging from $0.12\,\text{nm}$ to $0.32\,\text{nm}$. It is a proton donor-acceptor interaction induced by atom A withdrawing electrons from the H atom in an A—H bond. This leaves the proton partially uncompensated and establishes an A—H$\cdots$B hydrogen bond to the proton acceptor B

---

[3] after Fritz Wolfgang London

possessing a lone electron pair upon orbital overlap. The key feature that distinguishes hydrogen-bonding from other dipole-dipole interactions is the small size of the H atoms allowing a very close approach of donor and acceptor. In consequence, the electrostatic attraction is very strong. But despite its electrostatic origin, hydrogen-bonding has also a partly covalent character with the four contributing electrons occupying the two lowest molecular orbitals of the AHB fragment.

Most hydrogen bonds comprise O, N, F, or Cl, sandwiching the H atom. When present, they often dominate other molecular interactions, in particular in aqueous systems, thus having significant impact on structural properties. Regarding the systems investigated in this work, it is important to note that the F atom in a C—F bond is, in contrast to the F⁻ anion, a very poor proton acceptor, forming no or only very weak hydrogen bonds.

2.2   Steric effects

The large organic cations (and anions in 3rd generation ILs) cannot be treated as point particles with radially symmetric force fields. With growing complexity steric effects such as the excluded volume, the general shape of the molecules, or their size ratio, become exceedingly important.

In case of pyrrolidinium- or imidazolium-based cations (rf. Sec. 3.2), for instance, the ring structure is rather hydrophilic, and the N atoms are good proton acceptors in H-bonding interactions. Since the side chains become increasingly hydrophobic with increasing length, the molecule's force field has a strong local variation with prefered sites for different interactions. So even if a certain interaction such as H-bonding is energetically favorable, it might be blocked geometrically, e.g. by a side chain (steric hindrance). On the other hand, geometry might also trigger spacial configurations between molecules if their shapes are optimized for certain interactions (steric attraction).

2.3   Bulk correlations

Depending on the constituent ions of a given ionic liquid, the interactions introduced above contribute differently to the total interaction potential and hence the bulk liquid structure of an ionic liquid. Despite the vast variety of ionic liquids, scattering data indicate that long-range charge-ordered structures are a generic feature of their liquid structure [36–39]. Correlations up to 20 Å were found corresponding to several distinct solvation shells. This is far more than observed in molecular systems [40].

As expected, these charge-ordered structures become less pronounced with increasing anion size [37]. The bigger the anion, the more delocalized its charge is, resulting in softer ionic bonding and more and more overlapping coordination shells for both ion species. At the same time, the correlation between liquid and solid structure, in some cases remarkably high [42], seems to decrease as more complex ions are incorporated. This is closely related to the appearance of different conformers in liquid and solid state, respectively, that have
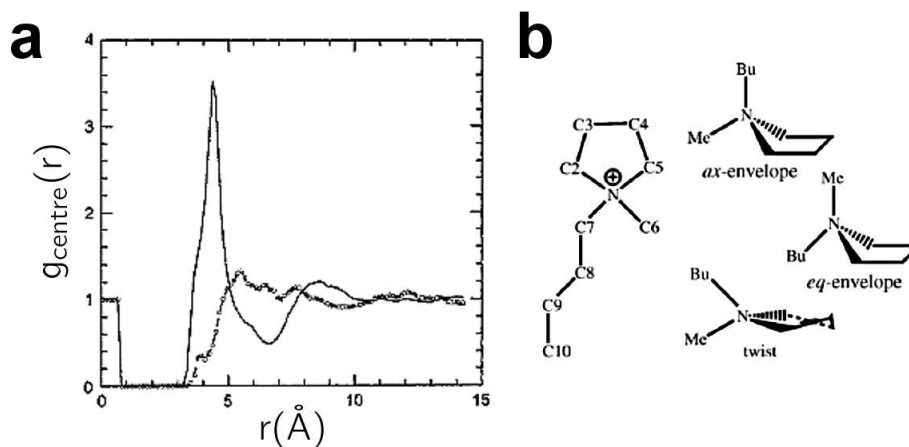
Figure 2.1: a) Partial radial distribution functions for the cation–cation distribution (circles line) and the cation–anion distribution (line) derived from neutron diffraction data. Distances are calculated from the center of the imidazolium ring (taken from Hardacre and co-workers [38]). b) Schematic representation of ring conformers of 1-butyl-1-methyl-pyrrolidinium (taken from Fujimori and co-workers [41]).

a large impact on the resulting structures [36, 41].

2.4 Ordering at interfaces

An interface, in our case a solid hard wall, disrupts the bulk coordination shells of the surrounding molecules and introduces new interactions to consider between the ions and the substrate, U_{a-s} and U_{c-s} (cf. Fig. 2.2). The interplay of interactions between ions of opposite (U_{c-a}) and same charge (U_{c-c} and U_{a-a}) governs the structural arrangement at the interface.

Differences between the specific interaction potentials of anions and cations with the substrate, U_{a-s} and U_{c-s}, may lead to favored adsorption of one ion species. For diluted, uncorrelated systems, the electrostatic potential perpendicular to the wall, $\psi(z)$, can be derived using the Poisson-Bolzmann equation for planar surfaces. It is obtained by combining the Poisson equation with Boltzmann statistics and reads

$$\frac{d^2\psi}{d^2z} = \frac{c_0 e}{\epsilon_0 \epsilon_r} \cdot \left(e^{\frac{e\psi(z)}{k_B T}} - e^{-\frac{e\psi(z)}{k_B T}} \right). \tag{2.9}$$

c_0 is the bulk concentration of the salt. The result is a diffuse electric double layer where counter ions screen the adsorbed surface ions. Increasing salt concentration increases the efficiency of this screening.

Ionic liquids, however, cannot be treated with this formalism since they are neither diluted nor uncorrelated. The formation of an electric double layer in response to a charged
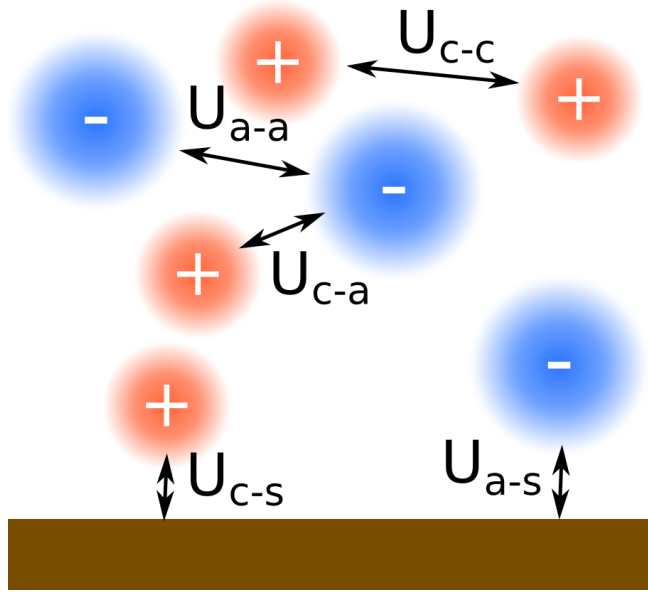
Figure 2.2: Interactions at interfaces. A solid hard wall (bottom) introduces ion-substrate interactions, U_{a-s} and U_{c_s}, competing with the bulk interactions, U_{c-a}, U_{c-c}, and U_{a-a}.

adlayer is not to be expected. One would rather expect an ionic-counterionic stacking perpendicular to the interface with decaying order towards bulk. Such a structure has already been proposed to explain capacitance measurements in conventional salt melts [43, 44]. The higher the correlations between the ions are, and the more rigid the initial adlayer is, the stronger such ionic layering would reach into bulk.

Electrostatically, the stacking of charged ionic layers is less favorable than a stacking of charge-neutral layers obtained when both species are present at the interface (checkerboard layering). In this case, the layering periodicity is half the periodicity of ionic layering assuming the densities in both cases to be constant (rf. Fig. 2.3c). The energetic penalty of ionic layering with respect to checkerboard layering can roughly be estimated by calculating Madelung's constant for both configurations which provides a scale for the electrostatic energy of a crystal lattice:

$$M = \sum_i (\pm)_i \frac{r_0}{r_i} \tag{2.10}$$

M is determined starting from an arbitrary ion within the lattice. r_0 is the shortest ion-ion distance of the lattice and r_i the distance from the center ion to the ith ion, whose contribution to the sum is negative (attractive) for opposite charge and positive (repulsive) for like charge. Since the discussed layering structures are decaying towards the bulk, M was calculated for two ionic double layers as a first estimation for the differences in electrostatic energy. For both configurations, the electrostatic energy is of the same absolute order, but of opposite sign, i.e. attractive in case of checkerboard layering and
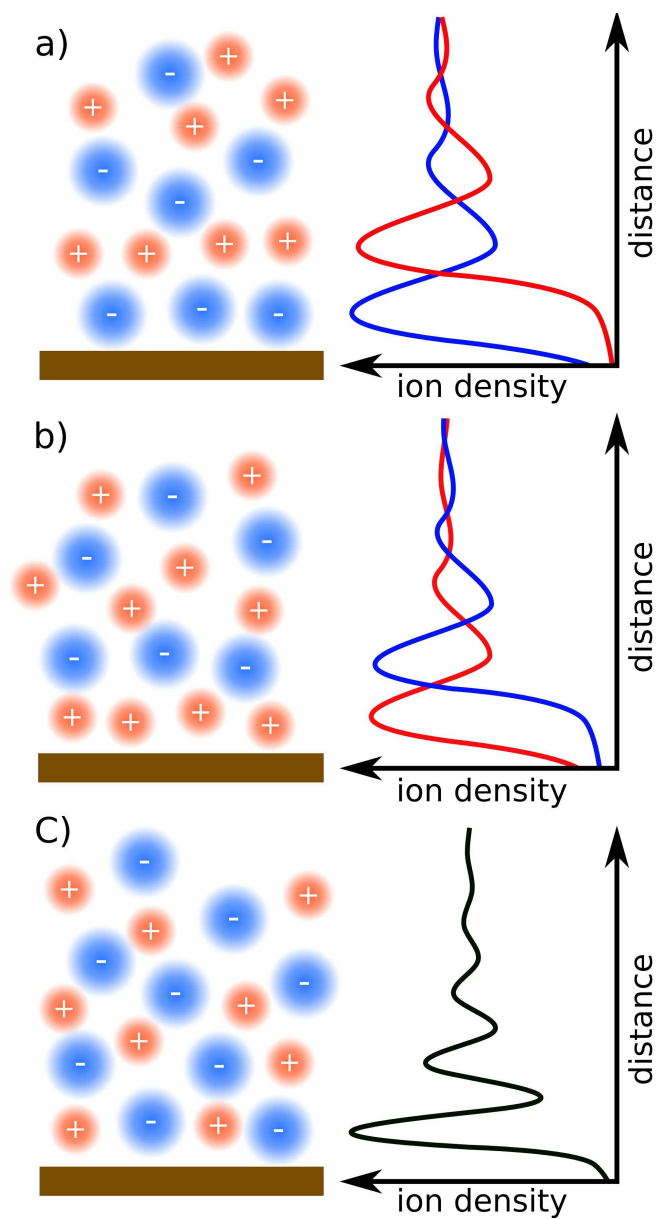
Figure 2.3: Sketch of possible configurations of an ionic liquid at a hard wall. The right panel gives a schematic representation of the resulting cation (red) and anion densities (blue). a) Ionic layering starting with a cation layer; b) ionic layering starting with an anion layer; c) checkerboard layering with both species present at the interface (total density profile in black).

repulsive in case of ionic layering. This results in an electrostatic penalty for the ionic layering of about $10\,\text{eV}$ per ion – a considerable value close to typical binding energies in primitive crystals. Although the actual penalty would be significantly lower due to the delocalized ion charges, this estimate shows that ionic layering needs a trigger to overcome electrostatics, such as a surface charge leading to a preferential adsorption of one ionic species.

As mentioned above, any interface-induced order of the ions is bound to fade off towards bulk structure with distance from the interface. The extent of this order, i.e. the decay length, is a measure for the correlation between the ions. Without correlations as in diluted systems, surface charges would be immediately screened by the formation of an electric double layer. The other limiting case is the correlation observed in molecular systems. Here, decay lengths between 1 and 2 layer distances are found [45–47]. By comparing the decay lengths for ionic liquids at interfaces to these values, insights on the role of ionic attraction in such systems might be obtained.

2.5   Experimental evidence

As has been shown in this chapter, the interfacial structure of an ionic liquid is governed by a complex interplay of different interactions, making it difficult to transfer information obtained for one specific system to others. Nevertheless, this sections supplies a brief overview over surface and interface sensitive studies on ionic liquids. For comparison, studies on molecular liquids at interfaces are covered first.

2.5.1   Structure of molecular liquids at interfaces

Theoretical predictions of density oscillations of liquids at sharp interfaces [48] could first be confirmed at the free surface of liquid metals [45, 49]. X-ray reflectivity data suggested exponentially damped oscillatory profiles[4] for both liquid gallium and mercury (Fig. 2.4a); layer spacings and decay lengths were close to the atomic dimensions and the correlation lengths in bulk, respectively. The first evidence of similar layering at a solid-liquid interface ("hard-wall effect" [50]) was found for liquid gallium at a diamond surface, again employing x-ray reflectivity [46]. The layering periodicity indicates the formation of Ga_2 dimers, which are also present in the solid α-phase, suggesting an interfacial trigger for heterogeneous nucleation (Fig. 2.4b+c).

Backed by both experimental and theoretical studies [51–53], it was long believed that non-metallic liquids do not to exhibit any interfacial structure. In 1999, this was proven wrong by a study on thin films of liquid tetrakis(2-ethylhexoxy)silane (TEHOS), a non-polar, nearly spherical molecule with a diameter of approx. 10 Å [54]. The strength of the layering found at SiO_2 had an inverse dependency on the substrate surface roughness. Hence, only a smooth "hard wall" sustains layering; a condition not fulfilled by the free

---

[4] The generalized distorted crystal model defined in the data analysis of the present work (see Sec. 6.4.3) is a derivative of the model introduced by Magnussen *et al.* [49].
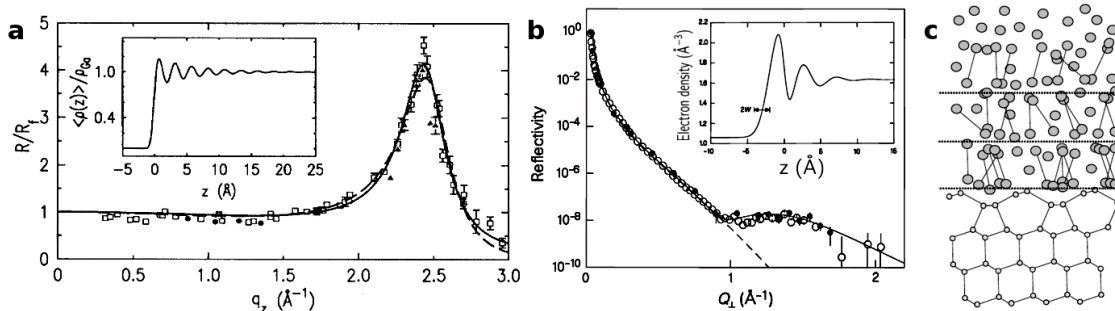
Figure 2.4: Interfacial layering of liquid gallium obtained from x-ray reflectivity data. a) The free surface of liquid gallium: The main panel shows Fresnel-normalized reflectivity data together with the best fit, the inset the resulting electron density profile (taken from Regan *et al.* [45]). b) Liquid gallium in contact with a diamond(111) surface: Reflectivity data and best fit are shown in the main panel, the inset gives the resulting electron density profile. A suggested interfacial configuration in agreement with this model is shown in c). The interface was accessed from the diamond side (taken from Huisman *et al.* [46]).

surface of most liquids due to capillary wave roughening [55]. Determining the structure of liquids comprising smaller molecules such as water remains challenging since the required resolution in real space is not readily achieved[5]. Nevertheless, it was shown by reflectivity measurements that the density of water perpendicular to a mica(001) surface exhibits oscillations. Reaching 10 Å, or about four molecular layers, into the bulk of the liquid, the layering is quite pronounced. The charged mica surface termination, however, might play an important role in the formation of this interfacial order.

2.5.2   The free surface of ionic lqiuids

The structure of the free surface of ionic liquids has been probed with a set of different techniques: Sum frequency generation (SFG), direct recoil spectroscopy (DRS), and x-ray photoelectron spectroscopy (XPS) were employed to study the in-plane surface structure, whereas neutron (NR) and x-ray reflectivity (XRR) were used to obtain structural information normal to the surface. These experimental approaches were accompanied by molecular dynamics (MD) simulations. To date, most studies focus on imidazolium-based ionic liquids, often with either BF_4 or PF_6 as anion. The general picture emerging from these studies is that a well-defined surface adlayer forms containing both anions and cations. At least for small anions such as BF_4 or PF_6, the cation appears to be the driving part for the structure formation. To which extend interfacial structures protrude into the bulk of the liquid remains ambigious.

SFG [58–60] and XPS studies [61] suggest an equal occupation of the surface with

---

[5] In order to unambigiously resolve 1 Å in real space with x-ray reflectivity, measurements to a maximim momentum transfers up to $\pi/1\text{Å} \approx 3\,\text{Å}^{-1}$ are necessary.
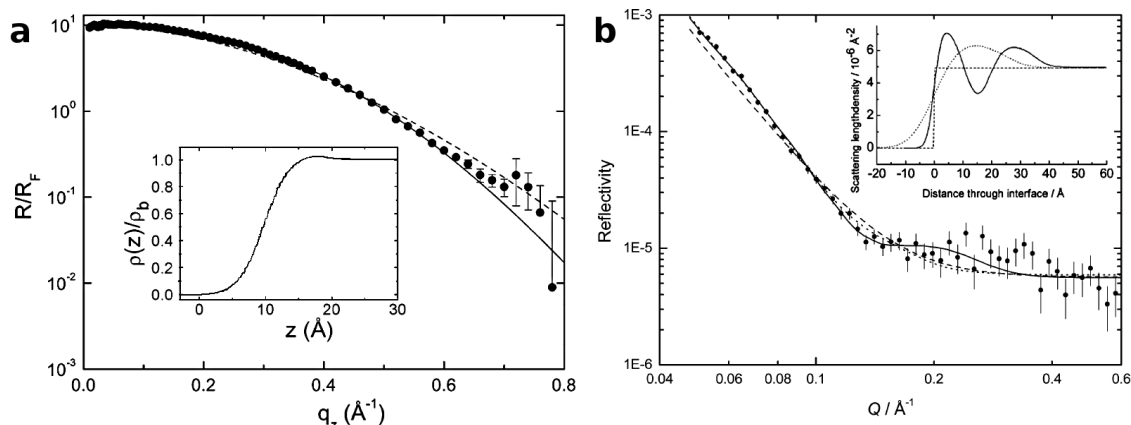
Figure 2.5: Neutron and x-ray reflectivity studies of the free surface of two $[\mathrm{C_n mim}]^+[\mathrm{PF_6}]^-$ - ionic liquids together with the corresponding density profiles obtained from best fits. a) X-ray reflectivity data from the free surface of $[\mathrm{bmim}]^+[\mathrm{PF_6}]^-$ (reproduced from Sloutskin *et al.* [56]). b) Neutron reflectivity data from the free surface of $[\mathrm{C_8 mim}]^+[\mathrm{PF_6}]^-$. The lines represent different fitting models: sharp interface (dashes), one-layer (dots), and three-layer (solid) (taken from Bowers *et al.* [57]).

both species. The alkyl chains protrude into the vapor phase and no effect upon anion variation was found. The imidazolium ring is either oriented parallel to the surface or slightly tilted. This model is in general supported by DRS although a strong influence of the anion size on the orientation of the cations was observed [62–64]. X-ray reflectivity revealed an anion density enhanced by 10% in a $6\,\mathrm{nm}$ thick adlayer at the surface [56] (rf. Fig. 2.5a). This enhancement is consistent with predictions from MD simulations [65, 66]. The also predicted density oscillations perpendicular to the surface, however, are not in agreement with the data, which was ascribed to shortcomings in the simulations' force fields [67]. No indication of density contributions from protruding alkyl chains on the vapor side, as suggested in the above-mentioned SFG and XPS studies, was found.

On the other hand, the limited resolution in the x-ray data – reliable data points were recorded up to $0.7\,\mathrm{\AA}^{-1}$ – in relation to the small dimensions of the anions does not allow to draw unambigious conclusions on the molecular scale details of the density profile. The same holds for the only neutron reflectivity study of the free surface published to date [57] (rf. Fig. 2.5b): While a plain error function density profile could be excluded by the data analysis, the suggested density oscillations protruding approx. $40\,\mathrm{\mathring{A}}$ into the bulk from a three-layer fit were not identified unambigiously. Nonetheless, the agreement with the afore-mentioned MD simulations is reasonably good.

2.5.3 Ionic liquids in contact with other media

The interface of ionic liquids in contact with other liquids has mainly been studied with focus on electrochemical properties such as mass transfer, electron transfer, or solubility between two immiscible electrolytes. On the interfacial structure, however, there is hardly any information available. Efforts have been undertaken to determine ion distributions across the interface between such electrolytes by fitting extended Poisson-Boltzmann equations to XRR data [68], but this approach has not been expanded to purely ionic systems yet. Therefore, only the ionic liquid-solid interface will be covered in the following. The interested reader can find an account of the research on the ionic liquid-liquid interface in the review from Aliaga *et al.* [69].

From the technical point of view, accessing the buried ionic liquid-solid interface is more challenging than the free surface. In consequence, only few experimental studies have been reported to date, again mostly involving imidazolium-based ionic liquids. SFG was employed to elucidate the orientation of imidazolium cations in the first adlayer of ionic liquids in contact with SiO_2 [70–73]. The results are inconsistent regarding both the orientations of imidazolium ring and alkyl chain with respect to the surface normal as well as the impact of anion size. Romero and Baldelli [70] reported alkyl chains lying flat on the SiO_2 surface and a strong decrease of the imidazolium ring tilt angle with anion size. Conboy and co-workers [72], however, found no significant anion size impact and deduced almost upright standing alkyl chains from their data. These discrepancies might stem from differing substrate preparation procedures and residual water contents [71, 72]. One common feature is, however, a significant tilt of the imidazolium ring away from the interface, which contrasts studies of the free surface employing the same technique (see Sec. 2.5.2) – except for a study on a very rough TiO_2 electrode [74]. SFG and FT-IR spectroscopy studies from RTIL-metal electrode interfaces back this view [75, 76], so such a configuration might be a generic feature of substrate-ion interactions at smooth interfaces. The tilt angle, though, was observed to decrease again with increasing negative surface potential [72] (see also Sec. 3.4).

The structure of confined ionic liquids interfacing with different smooth substrates has been investigated by Atkin and Warr using atomic force microscopy (AFM) [77]. Recording the required tip force upon approach as a function of the tip-substrate distance, the authors observed up to eight distinct solvation layers extending into the liquid (see Fig. 2.6a). The extent of this interfacial ordering depends highly on surface charge, surface roughness, and the orientation of the cations. The actual layer distance, on the other hand, is governed by the intrinsic dimensions of the ionic liquid. Pronounced layering was also found in $[C_n mim]^+$-based ionic liquid thin films employing x-ray reflectivity [78]. Depending on the thickness of the spin-coated films, the reflectivity data were fitted to up to five distinct layers (see Fig. 2.6b). Ordering was, however, only observed after thermal annealing at liquid-crystalline temperatures for long alkyl chain lengths, $n = 12$ and $n = 18$. A similar behavior was also found for an ionic liquid confined inside a carbon nanotube [79].

With the availability of more accurate force fields for different ions [82, 83], an increas-
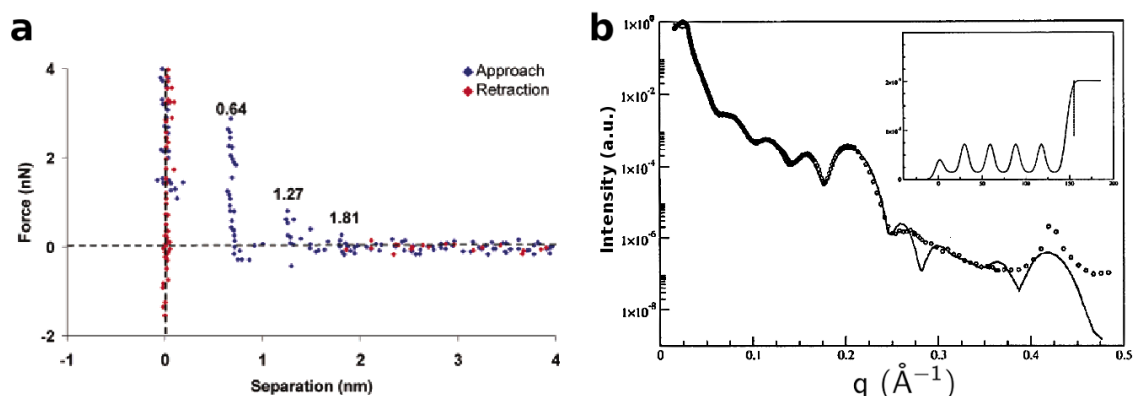
Figure 2.6: Interfacial structure of imidazolium-based ionic liquids in confinement. a) Force versus distance profile for an AFM tip approaching and retracting from a mica surface in $[C_2 mim]^+ [Acetate]^-$. The separation distances for each layer prior to push-through are given on the plot (taken from Atkin and Warr [77]). b) X-ray reflectivity from a $156\,\text{Å}$ $[C_{18} mim]^+ [PF_6]^-$ thin film on Si(111) together with the best fit obtained from a five-bilayer model. The inset shows the corresponding electron density profile (reproduced from Carmichael and co-workers [78]).
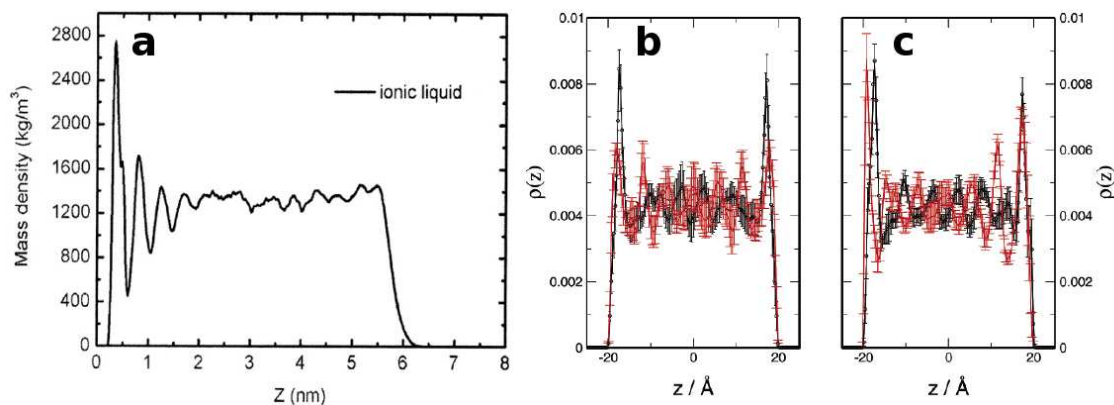
Figure 2.7: Density profiles perpendicular to ionic liquid-solid interfaces from molecular dynamics simulations. a) $[bmim]^+ [PF_6]^-$ at a hydrophobic graphite surface: Mass density of the ionic liquid versus distance from the interface (taken from Maolin and co-workers [80]). b+c) Dimethylimidazolium chloride ($[dmim]^+ [Cl]^-$) confined between two parallel charged walls: Cation (black) and anion (red) number densities in the interspace without (b) and with external electric field (c) generated by a uniform surface charge density of $\sigma = 2.0\,\mu C/cm^2$. The left wall is positively charged (taken from Pinilla and co-workers [81].

ing number of MD simulations of ionic liquids at interfaces has been reported [80, 81, 84–87]. Despite significantly different model systems, they all agree in the appearance of well-ordered structures at an interface that decay with increasing distance from the inter-face (see Fig. 2.7). Preferential adsorption, e.g. triggered by a polar surface, can lead to discrete ionic layers [86] – an effect that can also be induced by the application of an external potential [81, 85]. With increasing ion size[6], it is believed that steric packing effects will become increasingly important for the formation of charge-separated layers at interfaces [88].

---

[6] i.e. with increasing anion size: Due to computational limitations, mostly large imidazolium cations in conjunctions with simple anions, such as Cl^- or $[BF_4]^-$, have been modeled so far.

Chapter 3

Systems and research focus

The objective of this work was to elucidate the interfacial structures of ionic liquids at hard walls with molecular resolution and to gain insight into the dependence of these structures on external parameters such as temperature or size ratio between anion and cation. The large number of commercially available ionic liquids[1] poses the question which ones to choose as model systems. Such a model system should at best have high technological relevance, reference character, and should fit into the boundary conditions given by the experimental probe, in our case x-ray reflectivity. The latter point favours liquids comprising large molecules with a high degree of spacial correlation. To identify suitable candidates for further investigations, a series of ionic liquids was probed in preparatory bulk liquid scattering studies: The ionic liquids were sealed in quartz capillaries[2], and the liquid scattering measurements were carried out at beamline ID15B (ESRF, Grenoble) at an x-ray energy of $E = 89\,\mathrm{keV}$. Diffraction images were recorded with a two-dimensional image plate detector[3] with typical exposure times of 100 seconds. The radially averaged images yielded the diffracted intensity versus q. Figure 3.1 shows the resulting data for a selection of liquids.

It is evident that the two $[\mathrm{fap}]^-$-based ionic liquids (bold red and blue lines) exhibit very strong first correlation peaks below a momentum transfer range of $1\,\mathrm{\mathring{A}}^{-1}$, with $[\mathrm{bmpy}]^+[\mathrm{fap}]^-$ exhibiting the strongest correlations. Assuming a certain degree of correlation between bulk and interfacial structure, these data suggest a strong effect on the x-ray reflectivity from this particular system in a momentum transfer range readily accessible with our reflectivity setup (rf. Sec. 5.1). For that reason, the $[\mathrm{fap}]^-$ anion was considered to be the ideal starting point for parameter variation – in particular, since these ions are also technologically interesting with model character for hydrophobic, 3rd generation ionic liquids (rf. Sec. 3.1).

$[\mathrm{bmpy}]^+[\mathrm{fap}]^-$ was chosen as the reference system to study the effects of temperature variation, doping with molecular solvents, partial replacement of anions, and electric fields most carefully. In addition, several different cations were studied to probe the universality

---

[1] Merck KgaA, Darmstadt, Germany, alone offers more than 300 high-purity grade ionic liquids to date.
[2] Markröhrchen, 2.5 ± 0.2 mm diameter, 0.1 mm wall thickness; Hilgenberg GmbH, Malsfeld, Germany
[3] mar345, Marresearch GmbH, Norderstedt, Germany
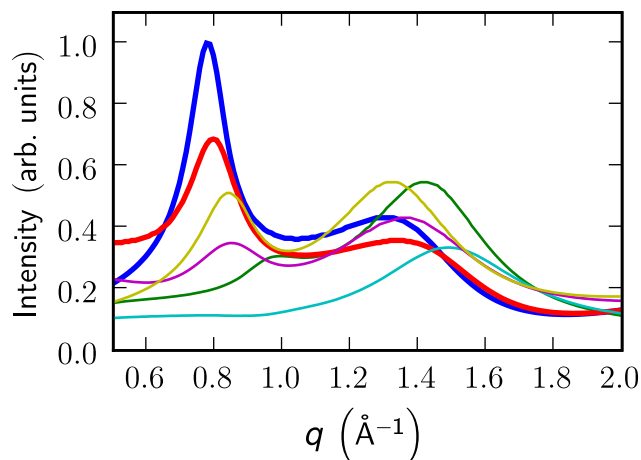
Figure 3.1: Bulk liquid scattering data from a variety of ionic liquids: [bmpy]$^+$[fap]$^-$ (bold blue), [hmim]$^+$[fap]$^-$ (bold red), [bmpy]$^+$[Tf$_2$N]$^-$ (yellow), [hmim]$^+$[Tf$_2$N]$^-$ (magenta), [bmim]$^+$[PF$_6$]$^-$ (green), [bmim]$^+$[BF$_4$]$^-$ (cyan). All curves are normalized to the first peak in the [bmpy]$^+$[fap]$^-$ data.

of the observed phenomena[4]. In the following subchapters, first the [fap]$^-$ anion and the different cations are introduced to acquaint the reader with the probed ionic liquids. Then, the applied manipulation strategies, doping and external electric fields, are motivated and outlined.

3.1 The [fap]$^-$ anion

The [fap]$^-$ anion was designed as a replacement of hexafluorophosphate ([PF$_6$]$^-$), which is one of the most widely used and investigated anions to date but suffers from a major drawback: its hydrolytic unstability caused by facial protonation of the fluorine atoms [18, 90]. This results in elimination of HF, a highly undesireable side product [9]. By replacing three fluorine atoms with pentafluoroethyl groups, facial protonation can be sterically surpressed and tris(pentafluoroethyl)trifluorophospate ([fap]$^-$) is obtained. It has a superior hydrolytic stability. The maximum water uptake of ionic liquids based on this anion is one order of magnitude smaller than for comparable [PF$_6$]$^-$-based ionic liquids and allows for water contents of less than 10 ppm in dried liquid. In Tab. 3.1, some physiochemical properties of [PF$_6$]$^-$- and [fap]$^-$-based ionic liquids sharing the same imidazolium cation are compared.

Besides the afore-mentioned much lower water uptake the difference in viscosity and electrochemical windows stand out, highlighting some major advantages of 3$^{\text{rd}}$ generation ionic liquids. The combination of low viscosity, exceptionally broad electrochemical

---

[4] Other systems were also investigated beyond the studies presented in this work [89].
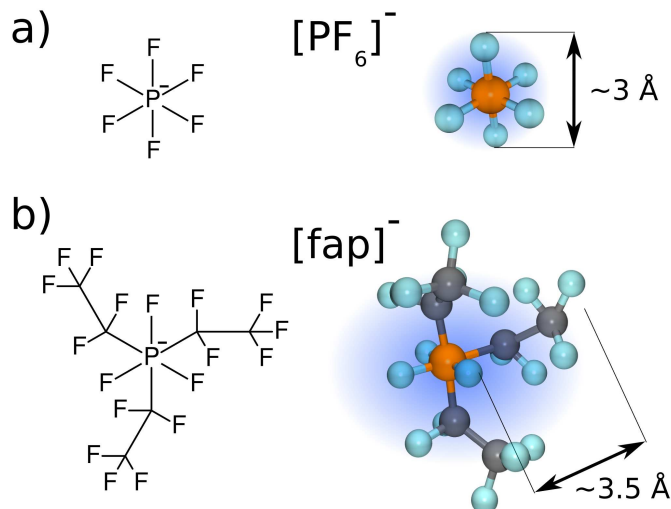
Figure 3.2: Hexafluorophosphate ($[PF_6]^-$) and tris(pentafluoroethyl)trifluorophospate ($[fap]^-$) anions in 2D and 3D representations. a) $[PF_6]^-$; b) $[fap]^-$. In the molecular sketches, negative charge clouds (blue) and typical dimensions are indicated.

window, and non-hygroscopicity provides an intriguing opportunity for electrochemical applications.

The $[fap]^-$ anion features about three times the molecular weight of $[PF_6]^-$. It is significantly bulkier, extending the spacial correlations between the ions and hence increasing the sensitivity of our probe. The shift of the size ratio between cation and anion towards the anion and the reduced charge density within the anion are expected to have a large impact on the structural arrangement in the bulk liquid [36].

3.2   Cation variation

A total of four $[fap]^-$-based ionic liquids were probed. The corresponding cations were 1-butyl-1-methylpyrrolidinium ($[bmpy]^+$), 1-hexyl-3-methylimidazolium ($[hmim]^+$), tetra-butylammonium ($[tba]^+$, and 1-octadecyl-3-methylimidazoilium. These cations all share N^+ as center of positive charge, but differ widely in structure and geometry (see Fig. 3.3). This gives the opportunity to study the influence of steric effects on the interfacial structure systematically.

While the temperature-dependent structure was investigated for all systems, the "fruit fly" for this work was the ionic liquid $[bmpy]^+[fap]^-$; the different manipulation strategies described in the coming subchapters were all applied to this system. The backbone of $[bmpy]^+$ is the five-membered C_4N ring of the pyrrolidine. Since the atoms of it are not arranged in the same plane, different conformational structures are possible (compare Fig. 2.1b) of which, according to ab initio calculations [92], only *envelope* conformers
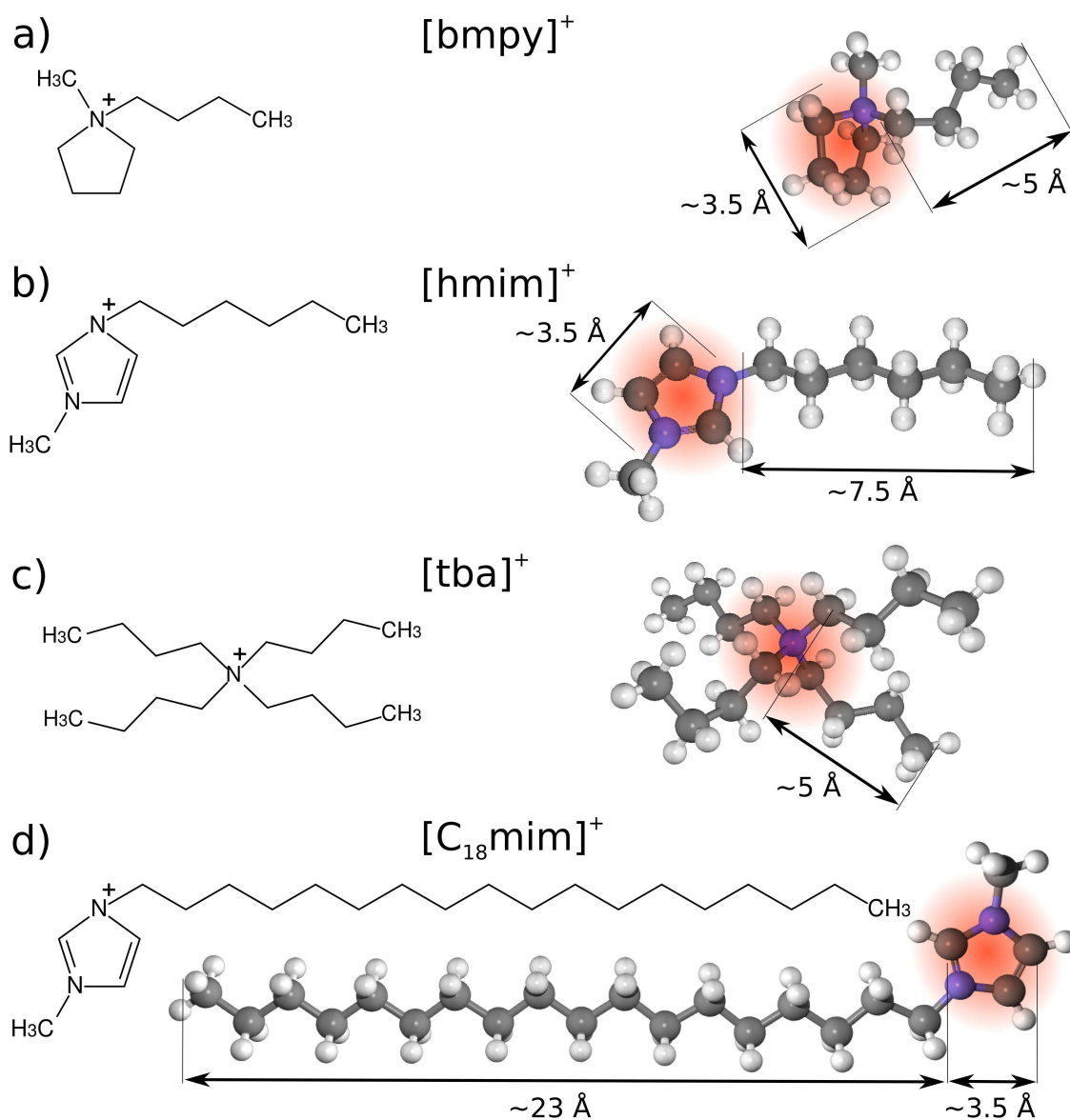
Figure 3.3: The four different cations investigated in this work in 2D and 3D representations. a) 1-butyl-1-methylpyrrolidinium ([bmpy]$^+$); b) 1-hexyl-3-methylimidazolium ([hmim]$^+$); c) tetrabutylammonium ([tba]$^+$; d) 1-octadecyl-3-methylimidazoilium ([c$_{18}$mim]$^+$). In the molecular sketches, positive charge clouds (red) and typical dimensions are indicated.

Table 3.1: Summary of physiochemical properties of $[PF_6]^-$- and $[fap]^-$-based ionic liquids.

	$[hmim]^+[PF_6]^-$	$[hmim]^+[fap]^-$
anion formula	PF_6	$C_6F_{18}P$
mol. weight $(g\,mol^{-1})$	312.24	612.28
weight ratio a:c	0.87	2.66
melting point $(°C)$	-61[91]	-14[15]
RT density $(g\,cm^{-3})$	1.3[15]	1.56[15]
viscosity (mm^2s^{-1})	548[18]	74[18]
conductivity $(mS\,cm^{-1})$	1.46[*,18]	1.32[18]
electrochemical window (V)	4.15[*] (vs. Pt)	6.5[†, 18] (vs. ferrocene)
max. water uptake (ppm)	22600[*,18]	2030[18]

*: $[bmim]^+[PF_6]^-$ *data.*

†: $[C_5mim]^+[fap]^-$ *data.*
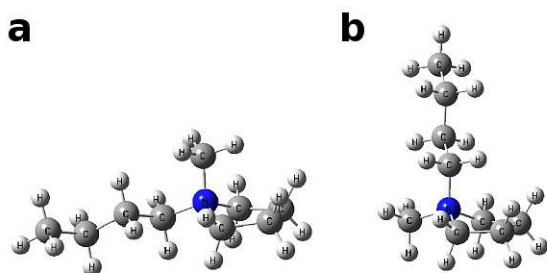
Figure 3.4: Optimized geometries of the *eq* and *ax* conformers of $[bmpy]^+$ obtained from Raman spectra (taken from Fujimori and co-workers [41]).

with the N sticking out of a plane spanned by the C atoms are stable. Of importance for the structure both in bulk and at interfaces is whether the hydrophobic butyl side chain lies within the ring plane (*eq* conformer) or out of this plane (*ax* conformer). Figure 3.4 shows both configurations. Two findings are deduced from the analysis of Raman spectra [41]: 1. Conformational changes occur mainly in the pyrrolidinium ring (i.e. the alkyl chain configuration remains unchanged). 2. For large anions both conformers are present in bulk liquid whereas for small anorganic anions mainly the out-of-plane conformer is involved. DFT calculations yield a typical energy difference of $3 - 5\,kJ\,mol^{-1}$ between these conformers, which is in the same order of magnitude as the differences in thermal energy covered by temperature variation in this work. Therefore, the conformal equilibrium, and with it the steric influence on the structure, can be expected to change significantly upon temperature change.

Two of the investigated cations are imidazolium-based, $[hmim]^+$ and $[c_{18}mim]^+$ (Fig. 3.3b, d). Imidazolium cations, in particular 1-butyl-3-methylimidazolium, are the most widely used and investigated cations in ionic liquids. Their common basis, imida-
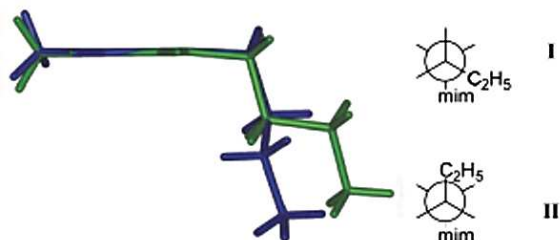
Figure 3.5: Overlay of gauche (I, blue) and anti (II, green) conformers of 1-butyl-1-methylimidazolium ([bmim]$^+$) obtained from x-ray diffraction of [bmim]$^+$Cl$^-$ crystals (taken from Berg and co-workers [97]). The conformation of the C(7)–C(8) bond of the butyl chain is shown in Fischer projection.

zole, is, similar to pyrrolidine, a five-membered ring, C_3N_2, with one C replaced by an additional N. In contrast to the former, it is an aromatic system with all ring atoms lying within the same plane[5]. For a series of involved anions, two main conformers have been identified for imidazolium cations in liquid state, reflecting *gauche* and *anti* configurations in the alkyl chain [95, 96] (Fig. 3.5). Here, the alkyl chain does not flip in- and out-of-plane with respect to the ring as is the case for pyrrolidine, but rather rotates around its first C–C axis. Hence, the imposed steric difference between these conformers is smaller (compare Figs. 3.4,3.5). Raman spectra indicate that both conformers are inherent features of 1-alkyl-1-methylimidazolium cations independent of the alkyl chain length and present with a 1:1 ratio in the liquid state [97].

[hmim]$^+$ has a similar shape and size as [bmpy]$^+$, so comparing their temperature-dependent interfacial structures in conjunction with [fap]$^-$ could give clues on generic properties of pyrrolidinium and imidazolium ionic liqiuds and on the role of their different conformation. [c$_{18}$mim]$^+$, on the other hand, differs vastly from the other cations for its three to four times longer side chain. To what extend this length difference is reflected by the ordering length scales, depends on the rigidity of these chains. The fourth cation, [tba]$^+$, has no ring structure as backbone but consists of four butyl chains around the central N$^+$. Steric interactions between the hydrophobic side chains of both ion species can be expected to drive the structural arrangement.

Table 3.2 gives an overview over the properties of all neat ionic liquids investigated in this work.

3.3   Doping

In order to study the impact of Coulomb screening on the interfacial ordering mechanisms of ionic liquids, two distinct doping strategies were followed to bias the screening behavior of [bmpy]$^+$[fap]$^-$: Molecular organic solvents were added in different concentrations introducing an dielectric medium to the system that shields the charges electrostatically.

---

[5] The presence of 6 π electrons within the ring structure renders imidazole aromatic. All ring atoms aligning in one plane is a typical feature of such systems [93, 94].

Table 3.2: Properties of the neat ionic liquids employed in this study. All data taken from the supplier's spec sheets if not stated otherwise.

	$[\text{bmpy}]^+$	$[\text{hmim}]^+$	$[\text{tba}]^+$	$[\text{c}_{18}\text{mim}]^+$
cation formula	$C_9H_{20}N$	$C_{10}H_{19}N_2$	$C_{16}H_{36}N$	$C_{22}H_{43}N_2$
cat. mol. weight (g mol^{-1})	142.26	167.27	242.26	335.59
weight ratio c:a	$1:2$	$2:3$	$1:1$	$3:4$
melting point (°C)	4	-14	58	43
RT viscosity $(\text{mm}^2\text{s}^{-1})$	184	$74^{[18]}$	n/a	n/a
RT density (g cm^{-3})	$1.59^{[15]}$	$1.561.56^{[15]}$	1.34^* (72°C)	1.32
$\delta\rho/\delta T^*$ $(10^{-3}\,\text{g cm}^{-3}\,\text{K}^{-1})$	1.0	1.0	0.8	0.9
electrochem. window[†] [V]	6.6	n/a	7.0	n/a
max. water uptake [ppm]	$3500^{[18]}$	$2030^{[18]}$	n/a	n/a
meas. water content[‡] [ppm]	< 100	< 100	n/a	n/a

[*]: *from bulk liquid pycnometry (see Sec. 5.3.1)*

[†]: *vs. ferrocene*

[‡]: *estimated with Karl Fischer titration (see Sec. 5.3.1)*

Secondly, some of the $[\text{fap}]^-$ anions were replaced by chloride ions, Cl^-, by addition of the corresponding salt, $[\text{bmpy}]^+\text{Cl}^-$, in different concentrations. The enhanced mobility of the atomic ions could allow them to impinge charged cation layers at the interface, thus screening them and counteract long-range layering.

Four requirements were to be met for molecular solvents as model dopants: full miscibility in $[\text{bmpy}]^+[\text{fap}]^-$, melting points below room temperature, chemical stability, and a resonably low vapor pressure to minimize evaporation during data acquisition and thus keeping the solvent concentration stable. Both solvents chosen for this study, propylene carbonate (PC) and triethylene glycol (TEG), are polar, aprotic solvents and fulfill these needs sufficiantly. The former, PC, constitutes in addition a technologically relevant system: It is frequently used as high-permittivity component in electrolytes today [98, 99]. Its electrochemical properties in conjunction with various ionic liquids has been studied to date though neither in conjunction with $[\text{bmpy}]^+[\text{fap}]^-$ nor sensitive to interfacial structures [100–102]. The cyclic PC differs strongly in molecular structure from TEG, so the screening effects of two different generic molecular structures are compared (see Fig. 3.6. An overview over the properties of both the dopants and the ions is given in Tab. 3.3.

3.4 Electric field effects

External electric fields present another handle to alter the electrostatics at the ionic liquid-sapphire interface. Since ionic liquids are conducting, voltage application below the substrate with a counter electrode immersed in the liquids gives rise to a corresponding poten-
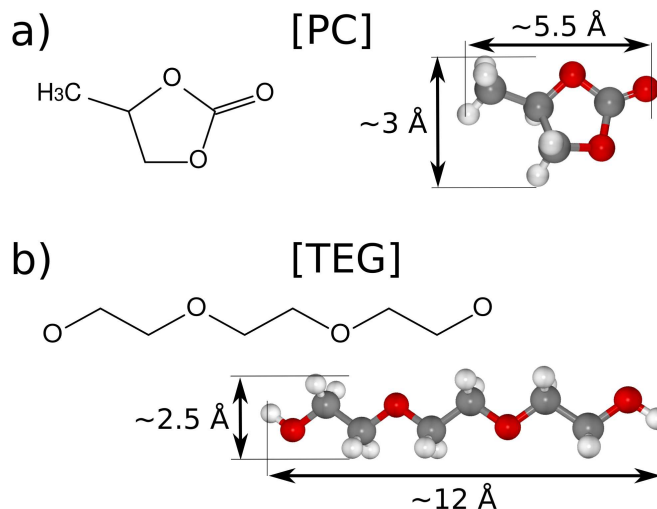
Figure 3.6: The molecular organic solvents used as dopands for $[\mathrm{bmpy}]^+[\mathrm{fap}]^-$ in 2D and 3D representation. a) Propylene carbonate (PC); b) Triethylene glycole (TEG). Typical dimensions are indicated.

tial drop across the substrate. In response to this external field, a conducting liquid reduces its contact angle according to the Young-Lippmann equation (electro-wetting, [103]):

$$cos\left(\theta\right) = cos\left(\theta_0\right) + \frac{\epsilon_r \epsilon_0}{2\gamma d} V^2 \tag{3.1}$$

θ is the contact angle, θ_0 the contact angle with external voltage $V = 0$, ϵ_r the dielectric constant of the substrate, γ the surface tension of the liquid, and d the thickness of the substrate. Contact angle studies on several ionic liquids confirm this equation qualitatively but show, however, a jump at zero voltage (compare Fig. 3.7a). This points towards a strong steric influence on the structural configuration. In contact with metal, electrochemical capacitance studies give evidence for reorientation of interfacial cations [69] (Fig. 3.7b).

Table 3.3: Properties of the molecular organic solvents employed in this study.

	propylene carbonate	triethylene glycole
formula	$C_4H_6O_3$	$C_6H_{14}O_4$
mol. weight $[\mathrm{g\,mol}^{-1}]$	102.09	150.17
melting point $[^\circ\mathrm{C}]$	< -50	< -4
diel. const.	~ 65	~ 20
RT density $[\mathrm{g\,cm}^{-3}]$	1.20	1.13
RT vapor pressure $[\mathrm{mbar}]$	0.04	0.003
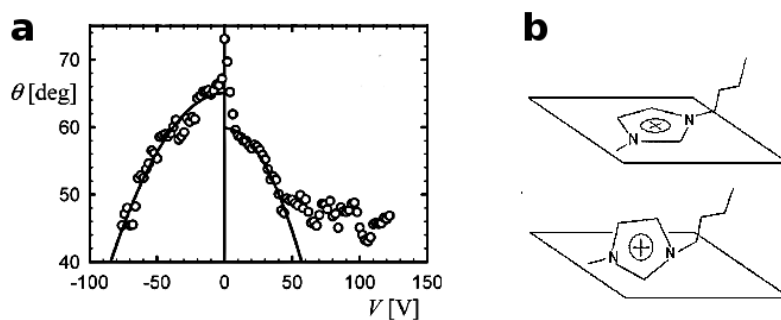
Figure 3.7: Electric field effects at ionic liquid-solid interfaces. a) Contact angle versus applied potential across a thin fluoropolymer film covered with $[\mathrm{hmim}]^+[\mathrm{fap}]^-$ (taken from Millefiorini and co-workers[103]). b) Cation orientation relative to a metal surface derived from capacitance measurements for negative (top) and for positive potential (bottom) with respect to the potential of zero charge (taken from Aliaga and co-workers [69]).

High energy x-ray reflectivity provides a direct probe to study these effects on a molecular level.

Part II

Technical and experimental details

Chapter 4

X-ray scattering

X-ray scattering provides versatile tools to study interfacial structures with sub-nm resolution, such as grazing incidence evanescent wave diffraction, crystal truncation diffraction, or x-ray reflectivity. The main experimental technique employed in this work is high energy x-ray reflectivity. Complementary information on the liquid structure (bulk spacial correlations) of the ionic liquids was acquired from bulk liquid x-ray scattering. This chapter outlines the principles of these experimental techniques. More comprehensive treatments can be found elsewhere [104–106].

4.1 X-ray reflectivity

If monochromatic x-rays impinge an interface, the specularly reflected intensity is a function of the incident angle and the electron density gradient across the interface. Measuring this intensity versus the specular angle, i.e. the x-ray reflectivity, is a very sensitive probe of the laterally averaged structural arrangement, which might be resolved in the subsequent analysis of the recorded data. Mathematically, such reflection patterns can be described using the optical principles of refraction.
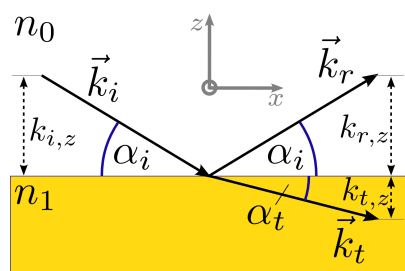
Figure 4.1: Reflection and transmission at a single interface between two media with different refractive indices, n_0 and n_1 (see text for details).

4.1.1   Basic concepts

The incident beam, a plane electromagnetic wave, can be represented by its electric field vector $\mathbf{E}(\mathbf{r}) = \mathbf{E}_0 exp(i\mathbf{k}_i\mathbf{r})$ with wave vector $|\mathbf{k}_i| = \frac{2\pi}{\lambda}$ and wave length λ. In a linear medium, the latter is related to the real (dispersive) part of the complex refractive index, n, via $\lambda = \lambda_{vac}/Re(n)$. The imaginary part of n, $Im(n)$, reflects the energy dissipation within the medium. For x-rays the refractive index is smaller than unity[1] and can be expressed as

$$n = 1 - \delta + i\beta \qquad (4.1)$$

with δ and β expressing the dispersion and absorption term, respectively:

$$\delta = \frac{\lambda^2}{2\pi}r_e\rho_e\frac{f^{(0)} + f^{(1)}(E)}{Z} \approx \frac{\lambda^2}{2\pi}r_e\rho_e \qquad (4.2a)$$

$$\beta = \frac{\lambda^2}{2\pi}r_e\rho_e\frac{f^{(2)}(E)}{Z} = \frac{\lambda}{4\pi}\mu\,. \qquad (4.2b)$$

r_e and ρ_e denote the medium's electron density, μ its absorption coefficient; $f(E) = f^{(0)}(q) + f^{(1)}(E) + if^{(2)}(E)$ is the x-ray form factor with the energy-dependent dispersion and absorption corrections [107]. Tabulated values from ab-initio calculations for vanishing momentum transfer, $q = 0$, are available online [108, 109]. For the q range covered in the x-ray reflectivity experiments, $q_{max} = 1.5\,\text{Å}^{-1}$, the q dependence of $f^{(0)}(q)$ is negligible.

At the ideal interface between two media with refractive indices, n_1 and n_2, the impinging beam is reflected and transmitted according to Snell's law[2]:

$$\frac{cos(\alpha_i)}{cos(\alpha_t)} = \frac{Re(n_2)}{Re(n_1)} \qquad (4.3)$$

For a beam passing from an optically denser medium into an optically lighter medium, $\delta_2 > \delta_1$, $cos(\alpha_t)$ reaches unity at the critical angle $\alpha_c = arccos\left(\frac{1-\delta_2}{1-\delta_1}\right)$. Total reflection occurs for $\alpha_i \leq \alpha_c$, i.e. no intensity propagates into medium 2. [3]

The relations between incident, reflected, and transmitted electric field strength, E_0, E_r and E_t, can be deduced employing the fact that the tangential components of the electric field must be continuous across an interface [111]. For incident beams polarized perpendicular to the scattering plane (s-polarized), the resulting Fresnel formulae for reflection

---

[1] The electrons involved in the scattering process can be approximated as harmonic oscillators with resonance frequencies ω_j[105]. The frequency of the incoming wave then needs to be bigger, $\omega > \omega_j$. A condition easily fulfilled by high energy x-rays.

[2] Following the conventions in x-ray optics, the angles are defined with respect to the interface plane, in contrast to visible-light optics, where the angles are defined with respect to the interface normal (Fig. 4.1).

[3] apart from an evanescent wave field parallel to the interface [110].

and transmission read

$$r = \frac{E_r}{E_0} = \frac{k_{i,z} - k_{t,z}}{k_{i,z} + k_{t,z}} = \frac{sin\left(\alpha_i\right) - \sqrt{\left(\frac{n_2}{n_1}\right)^2 - cos^2\left(\alpha_i\right)}}{sin\left(\alpha_i\right) + \sqrt{\left(\frac{n_2}{n_1}\right)^2 - cos^2\left(\alpha_i\right)}} \tag{4.4a}$$

$$t = \frac{E_t}{E_0} = \frac{2k_{i,z}}{k_{i,z} + k_{t,z}} = \frac{2sin\left(\alpha_i\right)}{sin\left(\alpha_i\right) + \sqrt{\left(\frac{n_2}{n_1}\right)^2 - cos^2\left(\alpha_i\right)}} \tag{4.4b}$$

For p-polarized light, similar equations are derived. Since n is almost unity for x-rays[4], there is practically no difference between both expressions and polarization effects are negligible. In a scattering experiment, the intensity $R_F = |r^2|$, the so-called Fresnel reflectivity, is the measureable quantity, not the electric field itself. R_F decreases rapidly with increasing incident angle. For $\alpha_i > 3\alpha_c$, R_F is approximated by

$$R_F \approx \left(\frac{\alpha_c}{2\alpha_i}\right)^4 . \tag{4.5}$$

In the specular geometry of reflectivity experiments, $|\boldsymbol{k}_i| = |\boldsymbol{k}_f| = k$ and $\alpha_i = \alpha_f = \alpha$, the momentum transfer vector, $\boldsymbol{q} = \boldsymbol{k}_f - \boldsymbol{k}_i$, only has a component parallel to the interface normal, $\hat{e}_z$ (see also Sec. 5.1.2):

$$q_z = 2ksin\left(\alpha\right) = \frac{4\pi}{\lambda}sin\left(\alpha\right) . \tag{4.6}$$

4.1.2   Interfacial roughness

The Fresnel coefficient in Eq. 4.4a describes the reflection from an *ideal*, infinitely sharp interface between two homogeneous media. In contrast to such an idealized interface, real interfaces always exhibit roughness, at least on an atomic length scale. Thus, the refractive index does not follow a step function across the interface as assumed in the derivation of the Fresnel reflectivity. Implying a Gaussian height probability distribution with standard deviation σ, the laterally averaging x-ray beam "sees" an error function profile for the refractive index (Fig. 4.3):

$$n\left(z\right) = \frac{n_0 + n_1}{2} - \frac{n_0 - n_1}{2}erf\left(\frac{z}{\sqrt{2}\sigma}\right) \tag{4.7}$$

In the limiting case of vanishing root mean square (rms) roughness, $\sigma = 0$, the step function profile of the ideal interface is recovered.

The effect of such vertical electron density variations on the reflected signal is an exponential damping factor to the ideal Fresnel reflectivity coefficient. It has analytically

---

[4] Deviations are of the order of 10^{-6} for most materials.
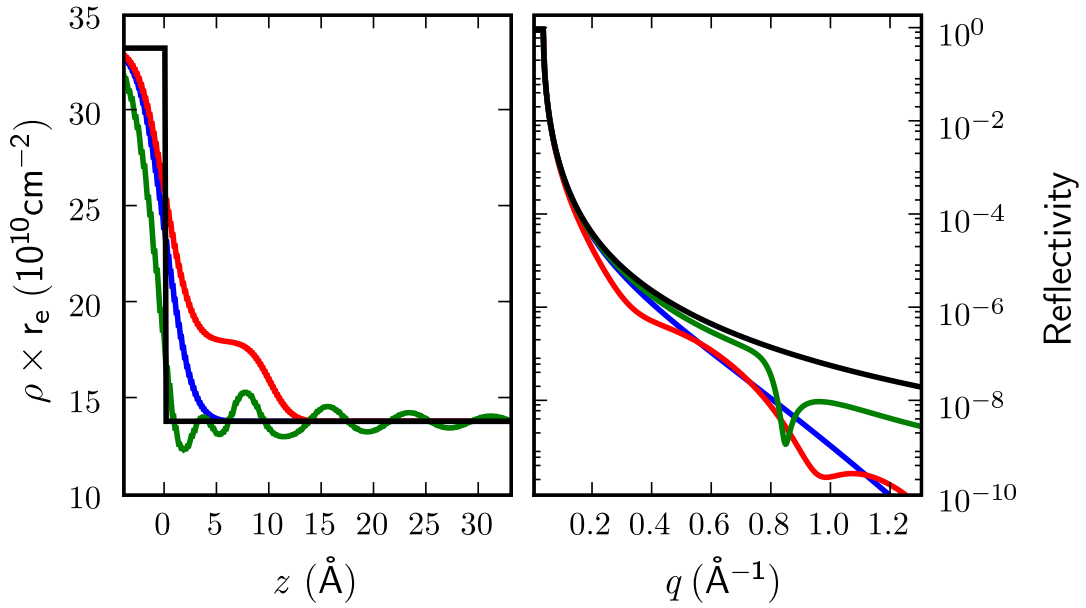
Figure 4.2: Different density parametrizations of the $[\mathrm{bmpy}]^+[\mathrm{fap}]^-$-sapphire interface (left) and the corresponding reflectivity curves (right). Black: ideal step interface without roughness, yielding the Fresnel reflectivity, R_F; blue: flat interface with interfacial roughness, $\sigma = 2\,\text{Å}^{-1}$ (rf. Sec. 4.1.2); red: additional interfacial adlayer of 30% higher density, $16\,\text{Å}$ thick (rf. Sec. 4.1.3); green: binary distorted crystal model parametrization using the best fit parameter set at $T = -15\,^\circ\text{C}$ (rf. Sec. 6.4.3 and Sec. 7.1.1).
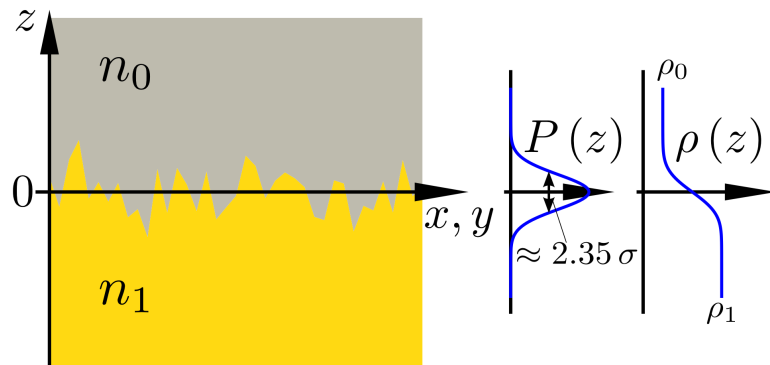
Figure 4.3: Height profile $z(x, y)$ (left) of a rough interface between two media, n_0 and n_1, with a Gaussian distribution (middle) around the mean value, $z = 0$. The standard deviation of this distribution is equal to the rms roughness, σ, of the interface. The electron density profile along the z coordinate resembles an error function profile in this case (right).
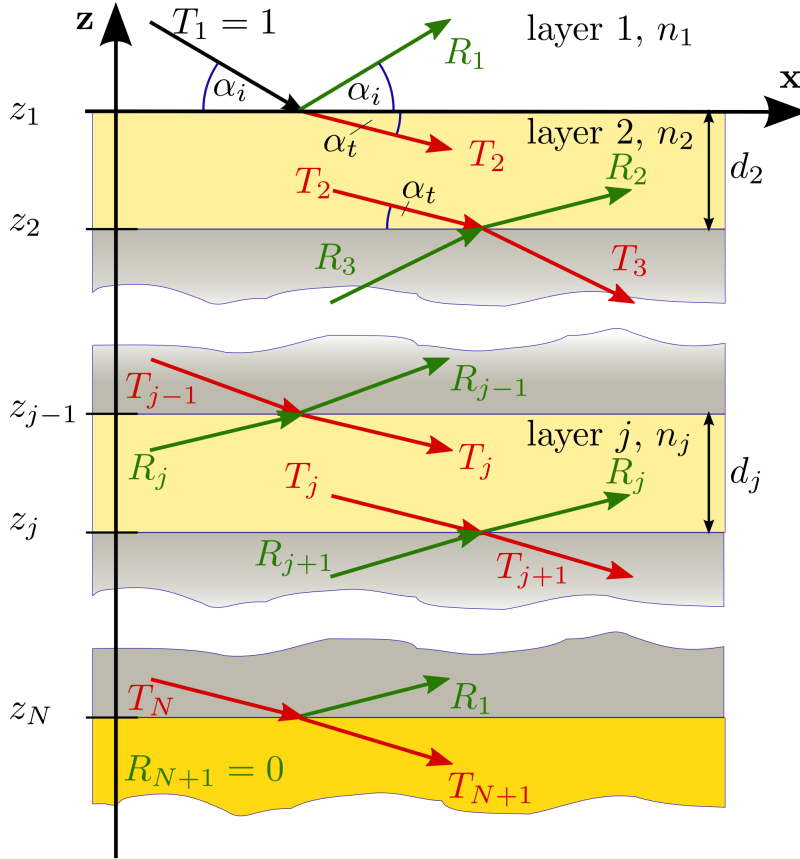
Figure 4.4: Scattering from a multilayer stack of $N + 1$ parallel layers. A description is given in Sec. 4.1.3.

been derived based on different assumptions for the lateral correlations of the roughness [112]. Employing the distorted-wave Born approximation (DWBA), it has been shown that for interfaces with uncorrelated roughness the *Névot-Croce* factor (NC, [113]) has to be applied, whereas for highly correlated interfaces the *Beckmann-Spizzichino* factor (BS, [114]) is valid:

$$r' = re^{-2k_{i,z}k_{t,z}\sigma^2} \quad \text{NC} \tag{4.8a}$$
$$r' = re^{-2k_{i,z}^2\sigma^2} \quad \text{BS} \; . \tag{4.8b}$$

Both factors differ mainly in the region of the critical angle. For hard x-rays at large angles, $\alpha_i \gg \alpha_c$, the difference becomes negligible.

4.1.3 Multiple interfaces

In section 4.1.1, a formalism to treat the reflection of x-rays from a single ideal interface between two media of homogeneous electron density was introduced. Most systems

probed with x-ray reflectivity comprise more complicated density profiles, e.g. a stack of different layers all contributing to the recorded reflectivity signal. The reflectivity signal from such a multilayer system is discussed in the following.

Consider the situation depicted in Fig. 4.4: A total of $N + 1$ layers define N ideal interfaces. Layer j, $j = 1 \ldots N + 1$, has the refractive index n_j and thickness d_j, the bordering layers 1 and $N + 1$ are semi-infinite ($d_1 = d_{N+1} = \infty$). Starting with the incident x-ray beam hitting interface 1 with $T_1 = 1$, at the angle α_i, a reflected (R_j) and a transmitted wave (T_{j+1}) are created at each interface j from T_j and R_{j+1}, $j = 1 \ldots N$. The corresponding amplitudes can be calculated using the Fresnel formulae 4.4 keeping in mind the interference with the wave reflected from the layer below. By definition, there is no reflected wave from the bottom; hence interface N can be taken as a starting point to calculate the resulting amplitude R_1 in a recursive way as shown by Parratt in 1954 [115]:

$$X_j = \varphi_{j,j} \frac{(r_{j,j+1} + X_{j+1}\varphi_{j+1,j})}{(1 + r_{j,j+1}X_{j+1}\varphi_{j+1,j})} \qquad (4.9\text{a})$$

$$r_{j,j+1} = \frac{(k_{j,\text{z}} - k_{j+1,\text{z}})}{(k_{j,\text{z}} + k_{j+1,\text{z}})} \qquad (4.9\text{b})$$

$$\varphi_{l,m} = \exp\left(-2ie^{i(l+m)\pi}k_{l,\text{z}}z_m\right) . \qquad (4.9\text{c})$$

X_j denotes the ratio between R_j and T_j, $r_{j,j+1}$ is the Fresnel formula for the reflection from interface j. The reflectivity of the entire multilayer system, $R = |X_1|^2 = |R_1|^2$ follows after N iterations. This recursion is called *Parratt formalism* and provides the backbone of the data analysis in this work.

The *Parratt formalism* yields exact results for the reflectivity of a multilayer system with ideal interfaces. Interfacial roughness can be taken into account by applying the appropriate correction factors (Eq. 4.8) to the corresponding Fresnel coefficients with rms roughness σ_j for interface j – as long as the approximation $\sigma_j \ll d_j$ holds for *all* layers. Systems with $\sigma_j \sim d_j$ for any interface have to be treated differently (see next section).

4.1.4 Arbitrary density profiles

Thanks to the steadily increasing computational capacity in modern computer systems, the processing of a large number of slabs within the Parratt formalism can readily be done. This allows to calculate the reflectivity from an arbitrary density profile by approximating it with a series of perfectly sharp interfaces (see Fig. 4.5)[5].

Kinematical approximation and Master formula

The Parratt formalism yields fully dynamical, exact solutions for the reflectivity from a given electron density profile. Nonetheless, it does not offer a direct analytical relation

---

[5] The thickness of the slices has to be chosen such that it is well below the density steps across these slices. Considering the corrugation always present at the atomic scale, the step size was set to 0.2 Å in the data analysis of this work.
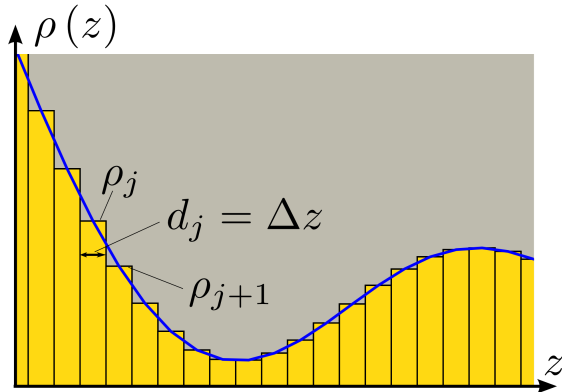
Figure 4.5: Approximation of an arbitrary density profile (blue curve) by a series of perfectly sharp interfaces between homogenious layers of thickness Δz (yellow columns).

between the measured reflected intensity and the real structure of a system. In the framework of the kinematical approximation, i.e. neglecting multiple scattering events, the reflectivity, $R(q)$, from a continuous density profile, $\rho(z)$, can be calculated via the so-called *Master formula* [104, 105]:

$$R(q) \;=\; R_{\mathrm{F}}(q)\,|F(q)|^2 \tag{4.10a}$$

$$F(q) \;=\; \frac{1}{\rho_{-\infty} - \rho_{+\infty}} \int_{-\infty}^{+\infty} \mathrm{d}z \frac{\mathrm{d}\rho(z)}{\mathrm{d}z} e^{iqz} \;. \tag{4.10b}$$

It provides a direct relation with the resulting signal separated into a contribution from a sharp interfacial, R_{F}, and a contribution from the interfacial structure, $|F(q)|^2$. While this expression is not valid in the region of the critical angle, α_c, where multiple scattering events dominate, it is very accurate for angles $\alpha > 3\alpha_c$ and often allows for a qualitative interpretation of reflectivity data.

4.2   Bulk liquid scattering

In the absence of any long-range order, the bulk structure of a liquid is dominated by short-range intermolecular correlations. The coordination around one single molecule can be characterized by its *radial distribution function* (RDF), $g(r)$, expressing the probability of finding another molecule at distance r from the first one[6]. For an ionic liquid as a binary system, three distinct partial RDFs are to be considered, ascribing the distribution of ions of the same, $g_{cc}(r)$, $g_{aa}(r)$, and different species, $g_{ca}(r)$. Generally, bulk liquid scattering allows to compute these partial RDFs as will be outlined in the following. But in practice, the complex nature of the ionic liquids treated in this work would require additional information on their structure in order to extract detailed real-space information. Some important structual features, such as the predominant correlation distance and its relative strength, however, can directly be derived from the scattered intensities and compared to the corresponding features found in the interfacial structure.

---

[6] more precisely, the center of another molecule

Consider an incident beam of monochromatic x-rays penetrating a bulk liquid sample. The intensity with respect to the momentum transfer, $I(\boldsymbol{q})$, scattered into a solid angle, $d\Omega$, is proportional to the differential scattering cross-section, $d\sigma/d\Omega = |f(\boldsymbol{q})|^2$, with $f(\boldsymbol{q})$ the sample's scattering amplitude. If we neglect multiple scattering, i.e. apply the first Born approximation to the scatterer, the scattering amplitude is, apart from a constant factor, the Fourier transform with respect to $\boldsymbol{q}$ of the scattering potential, $V(\boldsymbol{r})$. For x-rays, $V(\boldsymbol{r})$ is directly correlated to the electron density, and it follows:

$$I(\boldsymbol{q}) \propto \frac{d\sigma}{d\Omega} = |f(\boldsymbol{q})| = |\sum_k r_0 e^{i\boldsymbol{q}\cdot\boldsymbol{r}_k}|^2 \qquad (4.11)$$

The sum is over all electrons in the sample with r_0 the Thompson scattering length and $\boldsymbol{r}_k$ the position vector of electron k. In a liquid, all comprising particles are constantly moving around, and no direction of space is preferred; hence $I(\boldsymbol{q})$ becomes $I(q)$. Averaging over all orientational configurations, the exponential function within the sum becomes $sin(qr_k)$. In order to faciliate the further analysis, the scattered intensity, Eq. 4.11, can be split into intra-molecular (self-scattering) and inter-molecular contributions if the scattering is assumed to arise from independent neutral atoms with spherical electron density distributions (Debye approximation):

$$I(q) = \sum_{i,j} x_i x_j f_i(q) f_j(q) \frac{sinqr_{ij}}{qr_{ij}} + \sum_{i<j} x_i x_j f_i(q) f_j(q) S_{ij}(q) . \qquad (4.12)$$

x_i and $f_j(q)$ are the atomic fraction and form factor of atom type i, respectively, and r_{ij} the intramolecular distances between the atomic centers. The partial structure factors, S_{ij}, specify the intermolecular correlations and are related to partial RDFs between atoms , g_{ij}, via a Fourier transform relation,

$$S_{ij}(q) = 1 + 4\pi\rho \int_0^\infty r^2 dr \, (g_{ij}(r) - 1) \frac{sinqr_{ij}}{qr_{ij}} , \qquad (4.13)$$

with ρ the atomic number density of the liquid. For weak scatterers within the first Born approximation, only pair correlations contribute coherently to the overall intensity, so g_{ij} constitute the most fundamental structural information that may directly be derived from bulk liquid scattering. Prerequisite for their determination is detailed knowledge on the structural arrangement within the comprising molecules.

Prior to data analysis, several corrections have to be applied to the data to account for absorption, background, incoherent scattering, geometric and polarization effects, etc. These are covered in Sec. 6.5.

Chapter 5

Sample environment

The high energy x-ray reflectivity studies presented in this thesis crucially depended on access to 3rd generation synchrotron radiation sources in order to achieve the required molecular resolution. Hence, all experiments were carried out at a dedicated high energy beamline at the European Synchrotron Radiation Facility (ESRF) in Grenoble, France. This chapter gives an overview over the "sample environment" in a wider sense: Starting with a description of the beamline at the ESRF, the sample chamber and the sample preparation will subsequently be discussed. It concludes with a brief notion of the high voltage setup and the Kelvin probe sample chamber.

5.1 X-ray setup

The experimental setup employs a permanent setup dedicated for **H**igh **E**nergy **M**icro **D**iffraction (HEMD, [116]) located at the high energy beamline ID15A at the ESRF. After successful tests with a prototype, it was constructed and commissioned by our group in collaboration with the ESRF in 2005. This thesis reports the fourth PhD project on either the prototype or its permanent successor [117–119]. Since the experimental and technical aspects of the instrumentation have been discussed in detail in the preceeding works, only a brief summary of the parts which are important for the context of this work are outlined. The interested reader is referred to [118] where the same setup is described.

5.1.1 The high energy scattering beamline ID15A

The high energy scattering beamline ID15A is optimized for the use of x-ray radiation between $40\,\text{keV}$ and $300\,\text{keV}$. The x-ray beam is generated by a seven pole asymmetric multi-pole wiggler (AMPW)[1]. In order to reduce the heat load on the optical devices, the low energy part of the spectrum, $E < 40\,\text{keV}$, of the beam is absorbed by filters placed in front of the double-crystal Laue monochromator consisting of two asymmetrically cut and bent Si(111) crystals in fixed-exit geometry [120]. The first crystal is directly exposed to

---

[1] critical energy: $44.1\,\text{keV}$, minimum gap size: $20.6\,\text{mm}$, magnetic field: $1.84\,\text{T}$.
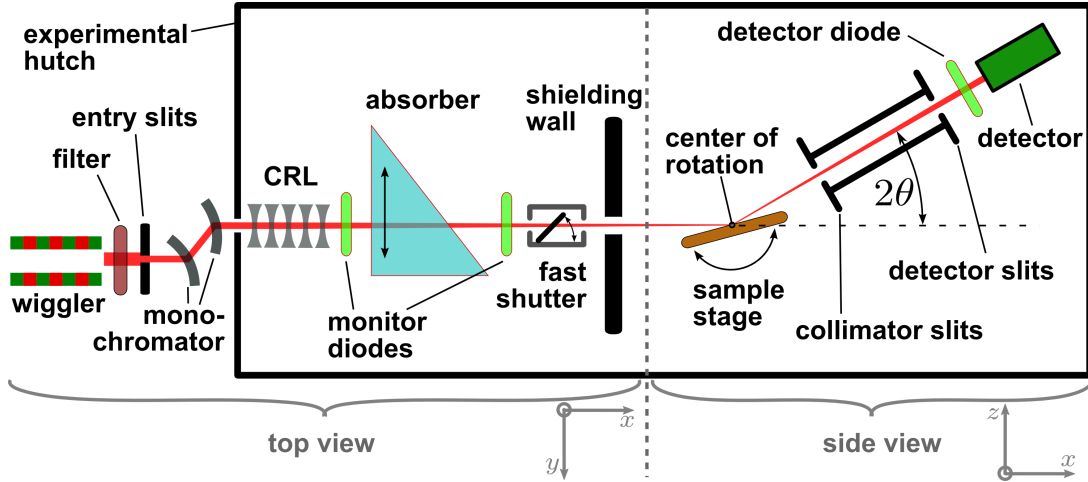
Figure 5.1: Sketch of the setup for high energy x-ray reflectivity experiments at beamline ID15A. The left part including the shielding wall is shown from the top, the right part as a side view.

the white beam and creates a virtual light source for the second crystal whose asymmetric cut determines the energy resolution[2] of $\Delta E/E \approx 2.3 \cdot 10^{-3}$. The fine-tuned bending radii of the two crystals result in an almost parallel beam profile in horizontal direction.

The source reaches its maximum brightness of approx. $3.3 \times 10^{14} \frac{\text{photons}}{\text{mrad}^2\,0.1\%\text{bw}}$ per $100\,\text{mA}$ ring current at a photon energy of $E = 50\,\text{keV}$. At $E = 72.5\,\text{keV}$, the energy used in all experiments, this value decreases by approx. 15% .

5.1.2 The HEMD setup

Figure 5.1 gives a schematic representation of the setup in the experimental hutch configured for high energy x-ray reflectivity. In the next paragraphs, the individual sections are described in more detail.

Beam focusing

The shape of the beam entering the experimental hutch of ID15A is defined by the slits in front of the monochromator. In order to optimize the signal-to-noise ratio and to reduce the footprint on the sample, the primary beam was focused to the sample position in the center of rotation of the sample stage by means of a compound refractive lens (CRL) comprising 150 to 200 single Al lenses [122]. The beam size at the sample position was determined by vertical and horizontal knife edge scans. The vertical beam size ranged

---

[2] Its value is a compromise between primary beam and bandwidth [121].

from $5\,\mu$m to $8\,\mu$m during the experimental runs[3], the horizontal beam size was approx. $26\,\mu$m.

Absorber

Typical reflectivity experiments at ID15A span a dynamic range of up to ten orders of magnitude [123, 124]. Current scintillation detectors cover only five orders of magnitude (compare Sec. 5.1.2) and require an absorber system for the detection of the entire reflectivity curve with one detector. A wedge-shaped PMMA[4] absorber allowed for continuous adjustment of the absorption factor between 1 and 10^{-5}, thus assuring a sufficiently high dynamic range. Despite its unhandy dimensions as a consequence of the small attenuation coefficient of PMMA, such a light-weight material was chosen for its less pronounced beam hardening properties in contrast to heavier materials: the x-ray attenuation decreases only slightly with increasing energy. So the ratio of higher harmonics present in the primary beam[5] does not change significantly for different absorber settings as would be the case for high Z absorber material such as lead glass. The wedge design allowed us to very acurately match the absorption factor to the specific requirements of a given measurement protocol (see Sec. 6.2).

Fast shutter

In order to minimize and control beam exposure of the sample, a fast shutter with switching times $< 50\,$ms was installed in the beam path. Its operation via an electro-magnetic gate was integrated in the beamline control software, allowing to open the gate $0.2\,$s before the detector exposure was initiated.

Sample stage and detector table

The key component of the HEMD setup, the six-circle diffractometer[6], is realized in two independent towers, the sample stage and the detector table (Fig. 5.2). For highest mechanical precision, both θ and 2θ (see Sec. 5.1.2) are set by a combination of linear motions rather than via a rotation stage. The resulting angular accuracies for θ and 2θ are $< 20\,\mu$rad and $< 10\,\mu$rad, respectively.

The sample stage itself consists of a massive swing mounted on four granite pillars whose rotation defines the incident angle. A motor tower mounted on top of the swing allows for alignment adjustments of the angles and lateral and vertical sample positions. From the top of the tower, there is $245\,$mm left to the center of the beam. Together with

---

[3] The vertical beam width is highly dependent on the stability of the electron beam in the storage ring, which was responsible for the large variation between the different experimental runs.

[4] poly(methyl methacrylate)

[5] For the wiggler settings used during the experimental runs, the ratio between $\lambda/3$ and λ radiation was about 10^{-3} [118].

[6] custom-made by HUBER Diffraktionstechnik GmbH & Co KG, Rimsting, Germany
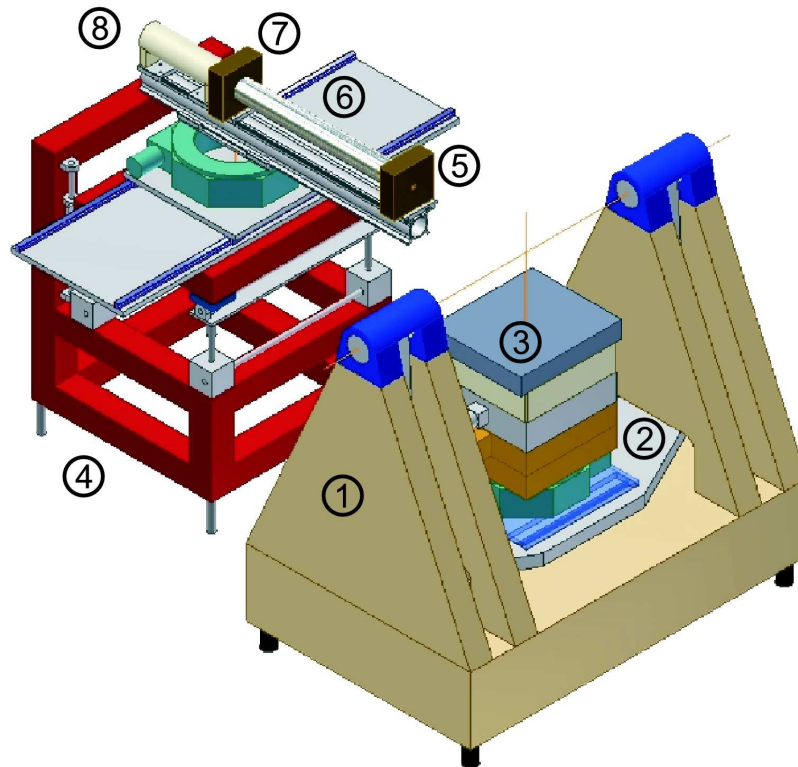
Figure 5.2: Design drawing of the HEMD instrument. 1: granite base; 2: swing; 3: sample tower; 4: detector stage; 5: collimator slits; 6: flight tube; 7: detector slits; 8: scintillation counter. (courtesy of F. Adams)

the heavy duty design (up to $500\,\mathrm{kg}$ can be mounted on top), this ensures a high flexibility for experimental setups.

A point detector mounted on the detector table records the reflected x-ray intensity. The scattering angle with respect to the incident beam defines the momentum transfer q; the resolution depends on the solid angle defined by the vertical opening of the detector slits. For background reduction, the scattered beam is guided through a shielding tube covering most of the distance between sample stage and detector of $1196\,\mathrm{mm}$. The entrance area into the tube is defined by collimator slits.

Detector

A single photon-counting scintillation detector[7] serves as point detector. It converts incoming x-rays to visible-light photons that can be post-processed after photo multiplication. The energy window can be adjusted such that higher harmonics radiation is rejected. Due to the large crystal thickness of $5\,\mathrm{mm}$, the conversion efficiency at $\mathrm{E} = 72.5\,\mathrm{keV}$ is still

---

[7] CyberStar CBYY48NA05B, FMB Oxford Ltd, Oxford, UK; scintillator: $5\,\mathrm{mm}$ thick, Tl activated NaI single crystal.
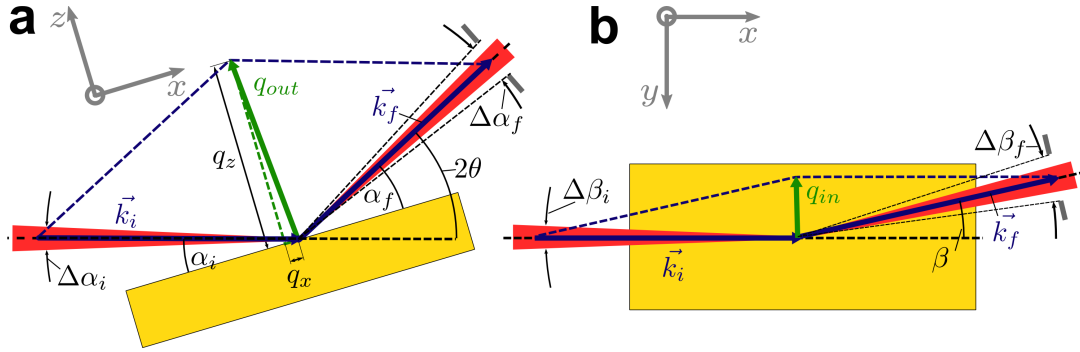
Figure 5.3: Sketch of the scattering geometry with the substrate surface serving as reference plane. a) Top view: The incident angle α_i is defined by the tilt of the interface with respect to the beam, the detector tilt 2θ defines the overall out-of-plane momentum transfer. In case of specular reflectivity, $\alpha_i = \alpha_f = \theta$ holds, and $q_{out} = q_z$, $q_x = 0$. The vertical detector slit gap defines the solid angle $\Delta\alpha_f$. b) Side view: If the detector laterally spans an angle β with respect to the incident beam, the momentum transfer has an in-plane component q_{in}. For $\beta = 0$, $q_{in} = 0$ and $q = q_{out}$ follow.

$> 99\%$. Since it is a single photon counter, the varying detector deadtime at different photon count rates needs to be corrected for. Based on a simple detector deadtime model [125], the corrected count rate, N_{corr}, as a function of the measured count rate, N_{meas}, and the detector's deadtime, τ, is given by

$$N_{\mathrm{corr}} = \frac{N_{meas}}{1 - N_{meas} \cdot \tau} \ . \tag{5.1}$$

By way of comparing the incident flux with the recorded intensity, τ was determined to $0.68\,\mu\mathrm{s}$ [118]. Up to $300\,000\,\mathrm{cps}$, this correction is accurate. Nevertheless, the count rates during data acquisition were always limited to a maximum of $150\,000\,\mathrm{cps}$.

In addition, three PIN semi-conductor diodes[8] were installed in the beam path (see Fig. 5.1). Two were used to monitor and normalize the incident beam, the third was mounted on a linear translation stage directly in front of the scintillation counter for the alignment of the sample in the focused primary beam without absorber. When not in use, it was moved out of the beam path.

Scattering geometry and resolution

Figure 5.3 shows a sketch of the scattering geometry. Defining the substrate surface as reference plane, the incident beam of fixed wave vector $\boldsymbol{k}_i$ hits the tilted interface and is scattered at the vertical and horizontal exit angles with respect to the beam, 2θ and β, respectively. Defining a coordinate system with $\boldsymbol{e}_z$ parallel to the interface normal and $\boldsymbol{e}_x$

---

[8] Eurisys Si PIN diodes, Canberra Inc, Meriden CT, USA

parallel to the beam direction, the momentum transfer, $\boldsymbol{q} = \boldsymbol{k}_f - \boldsymbol{k}_i$ reads

$$
\begin{aligned}
q_x &= k\left(\cos\alpha_f \cos\beta - \cos\alpha_i\right) & \text{(5.2a)}\\
q_y &= k\cos\alpha_i \sin\beta & \text{(5.2b)}\\
q_z &= k\left(\sin\alpha_f + \sin\alpha_i\right) . & \text{(5.2c)}
\end{aligned}
$$

In reflectivity experiments, incident and exit angles are equal ($\alpha_i = \alpha_f = \theta$) with the angle $\beta = 0$. In consequence, there is no in-plane momentum transfer and $|\boldsymbol{q}| = q_z = q$, i.e. the overall momentum transfer has only a vertical component,

$$
q = q_z = 2k sin\theta , \qquad\qquad\qquad (5.3)
$$

with $k = 2\pi/\lambda$.

The experimental resolution in q space depends on the bandwidth of the incoming beam, $\Delta E/E$, its angular divergence, $\Delta\alpha_i$ and $\Delta\beta_i$, and the aperture of the detector defining the solid angles $\Delta\alpha_f$ and $\Delta\beta_f$. It can be expressed as the total differential of the momentum transfer components with respect to the afore-mentioned variables. With $\Delta\lambda/\lambda = \Delta E/E$, one obtains

$$
\begin{aligned}
\delta q_x &= q_z\left(\Delta\alpha_i + \Delta\alpha_f\right) & \text{(5.4a)}\\
\delta q_y &= k\left(\Delta\beta_i + \Delta\beta_f\right) & \text{(5.4b)}\\
\delta q_z &= \frac{\Delta\lambda}{\lambda}q_z + k\left(\Delta\alpha_i + \Delta\alpha_f\right) . & \text{(5.4c)}
\end{aligned}
$$

Only the vertical resolution, δq_z, is of interest in reflectivity experiments; integration of the signal in x and y direction relaxes the lateral contributions. Practically, this is done by adjusting the horizontal and vertical detector admittances, Δa_h and Δa_v, such that all reflected intensity from a certain momentum transfer q is recorded. The detector apertures, $\Delta\alpha_f$ and $\Delta\beta_f$, can be related to the admittances via

$$
\begin{aligned}
\Delta\alpha_f &\approx \frac{\Delta a_v}{l} & \text{(5.5a)}\\
\Delta\beta_f &\approx \frac{\Delta a_h}{l} & \text{(5.5b)}
\end{aligned}
$$

with l the distance between sample and detector.

For the beamline setup described above, the admittance and divergence contributions to δq_z are smaller than $10^{-6}\,\mathring{A}^{-1}$ and can be neglected already at small incident angles in comparison to the contribution from the energy resolution, $\Delta\lambda/\lambda = 2.3 \times 10^{-3}$ (rf. Sec. 5.4c).

5.2 Sample chamber

Several requirements were to be met by the custom-built sample chamber for high energy x-ray reflectivity experiments of the ionic liquid-solid interface:
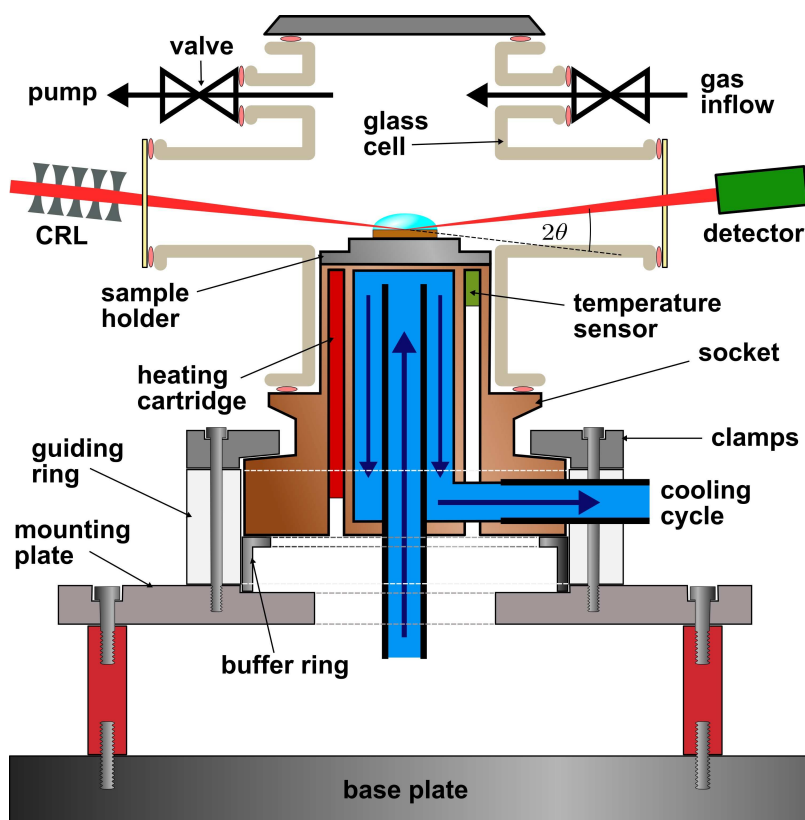
Figure 5.4: Sketch of the sample chamber as used at the high energy scattering beamline ID15A. See the text for details.
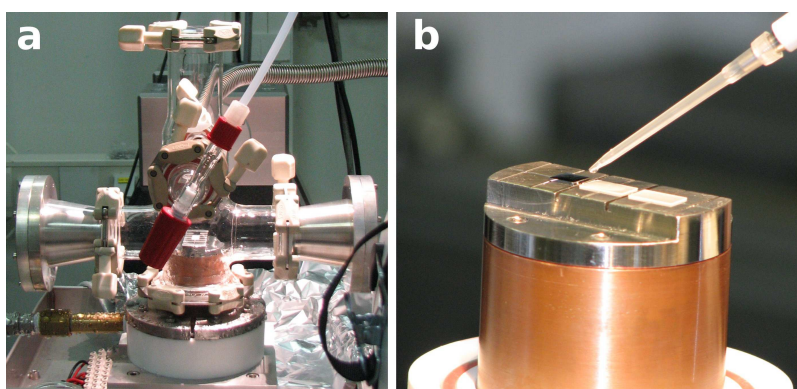

Figure 5.5: a) Side view of the mounted and fully connected sample chamber. b) Close-up of the sample holder with three different substrates during the application of the ionic liquid with an Eppendorf pipette.

- high thermal and mechanical stability;

- fast temperature cycling over a wide temperature range;

- controllable, inert environment;

- quick and easy sample exchange;

- optional high voltage connectivity.

The answer to these requirements presented below is the result of an evolution of solid-liquid sample chamber designs [118, 119].

5.2.1 Design and materials

The sample chamber comprises four basic parts: the mount connecting it to the instrument, the chamber socket for temperature control and readout, the sample holder, and the glass cell with the x-ray windows and connectivity to manipulate the sample environment. Design and working principle are illustrated in Fig. 5.4.

Chamber mount

The chamber mount must provide a mechanically very stable and resilient fixation of the chamber to the HEMD sample stage. Of particular importance is a plane seating to avoid even ever so slight tilts of the sample during experimental runs. Already tilts of some 10^{-3} degree around the specular rotation axis can cause severe misalignment. A plane seating under all thermal conditions is guaranteed by only applying mechanical stress in one direction to fix the chamber to the mount. The chamber rests on a stainless steel buffer ring and is enclosed by a broad PTFE guide ring fixed to an adapter plate. Four quarter-circular stainless steel clamps, the socket, and a buffer ring are bolted down to the adapter plate. An extrusion from one side of the latter to the center leaves enough space for wiring and tubing of the chamber from below. The thin, $2\,\mathrm{mm}$ thick buffer ring reduces the undesired heat transfer from the socket to the mount and speads up thermal equillibration.

Chamber socket

The chamber socket is a rotationally symmetric copper heat exchanger suited for both liquid and gaseous cooling media. In the presented experiments, liquid nitrogen-cooled N_2 gas was used. Heating capability is provided by four heating cartridges[9] with a total heating power of $800\,\mathrm{W}$. Two calibrated platinum resistive temperature sensors (Pt100)[10] were used to control the temperature in a PID control circuit[11].

---

[9] Watlow Electric Manufactoring Company, St. Louis, USA

[10] Jumo GmbH & Co KG, Fulda, Germany

[11] A LakeShore 310 temperature controller was used to control the heating output of a power supply. The nitrogen flow was adjusted to the target temperature. Even above ambient temperature, a moderate flow was sustained to reduce the thermal inertia of the socket. The PID settings were optimized manually.

The accessible temperature ranges from $-60\,°C$ to $300\,°C$. While temperature stability in a typical cooling step of $\Delta T = 150\,K$ is reached within minutes, it takes nevertheless approx. $2\,h$ for the whole setup to thermally relax. In equillibrium, a temperature stability of $\pm 5\,mK$ is acchieved. One of the major advantages of this socket design is that the sample environment is completely sealed off from the socket's control functions.

Sample holder

On top of the chamber socket, a circular area of $50\,mm$ diameter, the stainless steel sample holder is mounted. It has a round base and ends in a rectangular platform on which the substrates are placed (Fig. 5.5). Up to three substrates can be mounted at once allowing for independent measurements at an equilibrated temperature. The sample holder can easily be exchanged for cleaning purposes.

Glass cell

Imposed on the sample holder, a cylindrical glass cell is connected to the base of the socket via a KF50 vacuum flange. It consists of borate glass and has several further KF flanges fused into it: along the beam path to connect x-ray windows to it[12], two in the upper part for the vacuum pump and the gas inflow, and at the top to connect a end cap or provide additional connectivity, e.g. for pressure control, when needed. Vacuum pressures down to $10^{-6}\,mbar$ were reached.

5.3 Sample preparation

5.3.1 Ionic liquids

All ionic liquids were procured from Merck[13] in high purity grade with both water and chloride content specified below $100\,ppm$. While especially water contamination is a major problem for many conventional ionic liquids, it is not an issue with the highly hydrophobic 3rd generation ionic liquids employed here (see Sec. 3.1). Nonetheless, each liquid has been degassed in a vacuum oven at $1\,mbar$ and $80\,°C$ for at least $24\,h$ prior to application in order to remove residual water. For the experiments, an ionic liquid droplet was applied to the readily mounted substrate with an Eppendorf pipette[14] at $110\,°C$, the high temperature preventing condense contamination from the ambient environment. During experiments, the sample environment was evacuated and any water uptake suppressed. As a cross-check, the water contents have been determined *ex situ* using Karl Fischer titration [126, 127]. Although the measurements were carried out at ambient conditions,

---

[12] In this work, both kapton and mylar windows were employed of which the background was neglectible in the q range probed in the reflectivity and bulk scattering experiments.

[13] Merck KGaA, Darmstadt, Germany

[14] Eppendorf AG, Hamburg, Germany
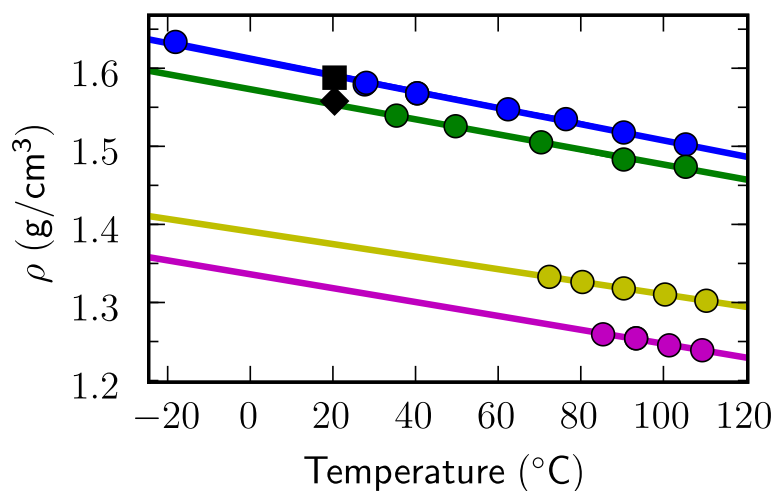
Figure 5.6: Temperature-depended bulk liquid mass density of the $[\text{fap}]^-$-based ionic liquids as determined by bulk liquid pycnometry (circles). The solid lines represent linear fits to the data for the cations $[\text{bmpy}]^+$(blue), $[\text{hmim}]^+$(red), and $[\text{tba}]^+$(yellow); the supplier's room temperature specifications are included as black square ($[\text{bmpy}]^+$) and diamond ($[\text{hmim}]^+$).

i.e. no particular care had been taken to minimize the water content, they confirm the manufacturer's specifications.

The bulk density of an ionic liquid needs either to be known or included as a free parameter in the parametrization of the interfacial electron density profile (rf. Sec. 6.4.3). So the temperature-dependent bulk densities of the ionic liquids were determined externally using bulk liquid pycnometry[15] to reduce the number of free paramters. As shown in Fig. 5.6, the measured densities exhibit a linear response to temperature changes in the temperature range of interest and agree well with the manufacturer's specifications if available.

The density and water content data described above are included in Tab. 3.2 in Sec. 3.2.

5.3.2 Solvent mixtures

Both solvents, PC and TEG, were procured from Sigma Aldrich[16] and properly degassed (see above) prior to subsequent treatment. Using Eppendorf pipettes and a high precision balance, different solvent:$[\text{bmpy}]^+[\text{fap}]^-$ ratios were prepared in test tubes (Tab. 5.1). Although the molecular solvents were also chosen for their very low vapor pressures (see Sec. 3.3), these are not neglectible and make it unfeasible to apply vacuum during the experiments as for the neat ionic liquids. Instead, the sample cell was shortly evacuated

---

[15] See [89] for details.
[16] Sigma-Aldrich Chemie GmbH, Munich, Germany

Table 5.1: Ratios of the solvent-ionic liquid mixtures.

	PC:$[\text{bmpy}]^+[\text{fap}]^-$	TEG:$[\text{bmpy}]^+[\text{fap}]^-$
molecular ratios	1:5, 1:2, 2:1, 5:1	1:5, 1:2
solvent mass concentrations [%]	3, 8, 25, 46	5, 11

immediately upon sealing and then saturated with a protective Ar gas atmosphere. The solvent-RTIL droplet was applied at $45°\text{C}$[17], the measurements were carried out at $8°\text{C}$.

5.3.3   Salt mixtures

The salts $[\text{bmpy}]^+$chloride and $[\text{bmpy}]^+$bromide were procured from Merck as were the neat ionic liquids. At room temperature both salts are solid. For further treatment, they were disolved in acetonitrile, a fully miscible solvent for both the salts and the RTIL, to 1:50 concentrations (mass ratio salt:C_2H_3N). With these dilutions, salt-ionic liquid mixtures of different molecular concentrations were prepared in test tubes and thoroughly degassed in a vacuum oven at $80\,°\text{C}$ to remove the dispencable acetonitrile. The weight of the resulting mixtures was determined to ensure the complete removal of residue acetonitrile. Thanks to the high volatility of the latter, this did not prove to be an issue.

Salts and ionic liquid, $[\text{bmpy}]^+[\text{fap}]^-$, share the same cation. Hence, the molecular concentration of the mixtures is equal to the ratio Cl^-:$[\text{fap}]^-$ or Br^-:$[\text{fap}]^-$, respectively. The different concentrations investigated during the experiments are listed in Tab. 5.2. They were applied identically to the neat RTILs (see Sec. 5.3.1) and measured at $8°\text{C}$.

Table 5.2: Ratios of the salt-ionic liquid mixtures.

	$[\text{bmpy}]^+\text{Cl}^-$:$[\text{bmpy}]^+[\text{fap}]^-$	$[\text{bmpy}]^+\text{Br}^-$:$[\text{bmpy}]^+[\text{fap}]^-$
molecular ratios	1:5, 1:2, 2:1, 5:1	1:5, 1:2

5.3.4   Substrates

The basal plane of single crystalline sapphire, α-Al$_2$O$_3$ (0001), was chosen as model hard-wall interface. It complies with two main requirements given by the experimental probe and system: chemical inertness against the ionic liquids and availability of superbly smooth wafers. Being the hardest of the oxide crystals and second only to diamond along

---

[17] This lower temperature, still well above ambient conditions, was chosen to minimize evaporation of the solvent from the mixture during application. The vapor pressures of PC and TEG, exponentially dependent on T, reach here $0.49\,\text{mbar}$ and $0.13\,\text{mbar}$, respectively.

the minerals, it is chemically inert against practically all acids and bases at ambient conditions [128], in particular also against hydrofluoric acid which migth be present in trace amounts even in $[fap]^-$-based ionic liquids[18]. Sapphire (0001) wafers are commercially available with near-atomic smoothness; the rms roughness of the specimens used in this work[19] was estimated to approx. 2Å from the slope of XRR data recorded at the dry interface (compare Sec. 4.1.2, see [89] for details). For the experiments, several $10 \times 6\,\mathrm{mm}^2$ substrates were cut from one of these wafers.

Cleaning protocol

In order to ensure clean, well-defined, and reproducable interfaces, a rigorous substrate treatment protocol was kept during all experimental runs:

1. iterative immersion in different solvents (acetonitrile, isopropanole, acetone, chloroform) in an ultrasonic bath for $15\,\mathrm{min}$ each;

2. Piranha etch (3 parts H_2SO_4, 1 part H_2O_2; $1\,\mathrm{min}$);

3. water rinsing: first under flowing water[20], then for several minutes in an ultrasonic bath;

4. drying under a jet of Ar gas;

5. UV/ozone surface cleaning[21] for at least $30\,\mathrm{min}$.

The wet chemical cleaning of the first three steps free the substrates very efficiently from practically all contaminations, leaving a clean and very hydrophilic surface. Submonolayer contaminations of organic material, e.g. stemming from the Piranha etch, however, might still be present at the surface. Such contaminations are readily removed in the final UV/ozone cleaning step: The molecules of any organic contaminants are excited and/or dissociated through photon absorption. Simultaneously, ozone and activated oxygen are produced, combining with the excited and dissociated molecules to volatile gases such as CO_2, H_2O, or N_2. After this treatment, the surface is not only even more hydrophilic than after the wet cleaning cycle, but also preserves this state significantly longer [129] (see Fig. 5.7a).
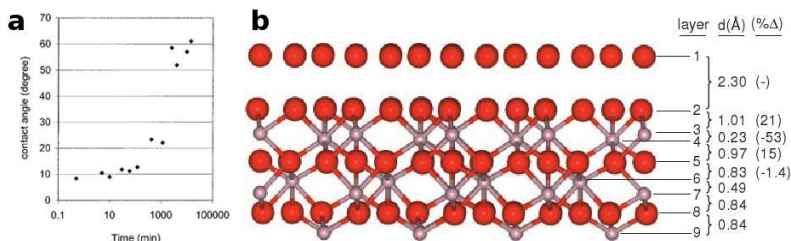
Figure 5.7: a) Contact angle of water on UV/ozone treated alumina versus time after treatment (taken from Luo and Wong [129]). b) Relaxed α-Al_2O_3 surface after wet chemical cleaning at ambient conditions derived from XCRD data: atomic layer spacings for oxygen (red) and aluminum atoms (silver) along the [0001] direction. The topmost oxygen layer stems from adsorbed water hydrogen-bonded to the partly hydroxyl-, partly oxygen-terminated surface layer of the sapphire. The corresponding hydrogen atoms are not included in the fitting model for lacking contrast (taken from Eng and co-workers [130]).

Substrate termination

Unlike the Al-terminated clean α- $-Al_2O_3$-vacuum interface observed under UHV conditions [131], the above-described cleaning procedure under ambient conditions renders the surface hydroxylated. X-ray crystal truncation rod data [130] yield a surface configuration after wet chemical cleaning intermediate between evacuated α-Al_2O_3 and fully hydroxylated γ-$Al(OH)_3$ – the former being highly reactive with water, the latter fully passivated – with a half-ordered water adlayer on top (see Fig. 5.7b)).

Based on the Pauling electrostatic bond valence principle [132], the adlayer stabilizes the surface by preventing oversaturation or undersaturation of the surface oxygen atoms. In the absence of adsorbed water, the same effect can be acchieved by in-plane O– H$\cdots$O hydrogen-bonding [130]. It is suggestive to assume this to be the case after UV/ozone treatment, thus giving a reasonable explanation for the higher and better-preserved hydrophilicity thereafter. Since the substrates were kept under UV light right until mounting upon which the sample environment was immediately evacuated, such surface configuration should still be maintained when in contact with the ionic liquid.

---

[18] Electrical resistivity measurements across the SiO_2-$[bmpy]^+[fap]^-$ interface were performed to test the suitability of Si wafers for the XRR experiments. The oxide was insulating at first, but a rapidly increasing leakage current was observed after approx. $1\,h$, suggesting an HF residue emerging as the ionic liquids saturate with H_2O.

[19] $\varnothing = 2''$, $d = 0.4\,mm$, procured from Saint-Gobain Crystals, Newbury OH, USA

[20] ultra-pure water processed in a Millipore purification system; Millipore GmbH, Schwalbach, Germany

[21] UV light irradiation in a $400\,mbar$ oxygen atmosphere, $\lambda = 172\,nm$; BlueLight Excimer Compact Source, $20\,W$ el. power, $50\,mW\,cm^{-2}$ irradiance; Heraeus Noble Light, Hanau, Germany
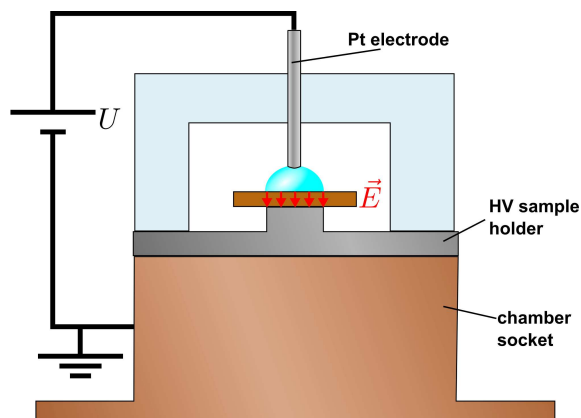
Figure 5.8: Sketch of the modified high-voltage setup. See text for details.

5.4 High voltage setup

In order to carry out reflectivity measurements in the vicinity of external electric fields across the interface, some minor modifications were necessary in the sample environment as is illustrated in Fig. 5.8: The sample holder was replaced by another one with a much smaller, $4 \times 6 \, \text{mm}^2$ platform with rounded edges to hinder voltage break-throughs by the increased electrode-ground vacuum distance. A high-voltage electrical feed-through was connected to the upper flange of the chamber to supply the desired voltage to the immersed platinum electrode. The latter was held in position by a PTFE bridge across the sample holder. Two different high-voltage power supplies of opposite polarities[22] provided a voltage of up to $\pm 40 \, \text{kV}$. The counter electrode (the chamber socket) was always kept grounded.

5.5 Kelvin probe chamber

In collaboration with the Max Planck Institute for Iron Research in Düsseldorf, Germany, a combined x-ray / Kelvin probe chamber was constructed and commissioned at the high energy beamline ID15A. It allows to monitor the change in substrate surface potential upon x-ray irradiation. Below, only a brief outline of the working principle is given and the chamber design is introduced. More exhaustive treatments can be found in literature [133, 134].

5.5.1 Working principle

The Kelvin probe method (KPM) is a very sensitive probe of relative changes of work functions between the Kelvin probe tip and the sample surface below it. Figure 5.9 illustrates the working principle: The metal tip is electrically connected to the metal sample

---

[22] 40A12P4 and 40A12M4, Ultravolt Inc, Ronkonkoma NY, USA
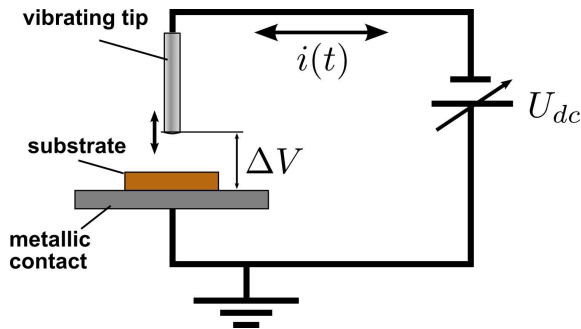
Figure 5.9: Circuit diagram of the Kelvin probe method to determine the Volta potential of a surface. See text for details.

holder and brought in close contact to the sample surface. Differences in the work functions of tip, sample holder, and substrate give rise to an electrostatic potential difference, ΔV, between tip and sample holder (*Volta potential*). Comparing ΔV with and without irradiation of the substrate surface yields the radiation-induced surface potential difference.

The vibrating tip induces periodic modulations of the capacitance between tip and sample holder and induces a current $i(t) = \hat{i}cos(wt)$ within the readout circuit that is amplified. In order to measure ΔV, an external DC voltage, U_{DC}, is applied until $\hat{i}$ is nullified. It follows that $\Delta V = -U_{DC}$.

5.5.2 Chamber design

The core part of the combined x-ray / Kelvin probe setup is a custom-built Scanning Kelvin Probe (SKP) chamber. It allows for adjusting the Kelvin probe tip in all three dimensions of space with a resolution of $10\,\mu$m. The experimental lateral resolution, however, is limited by the diameter of the tip, which was approx. $400\,\mu$m. The chamber socket is connected to the chamber through a hole in the bottom and fastened to its base plate. It carries heating cartridges and is connected to a cooling cycle, allowing for temperature variation in a range between $-40°$C and $200°$C. Figure 5.10 shows a picture of the mounted x-ray / Kelvin probe chamber, taken from the direction of the incident beam.
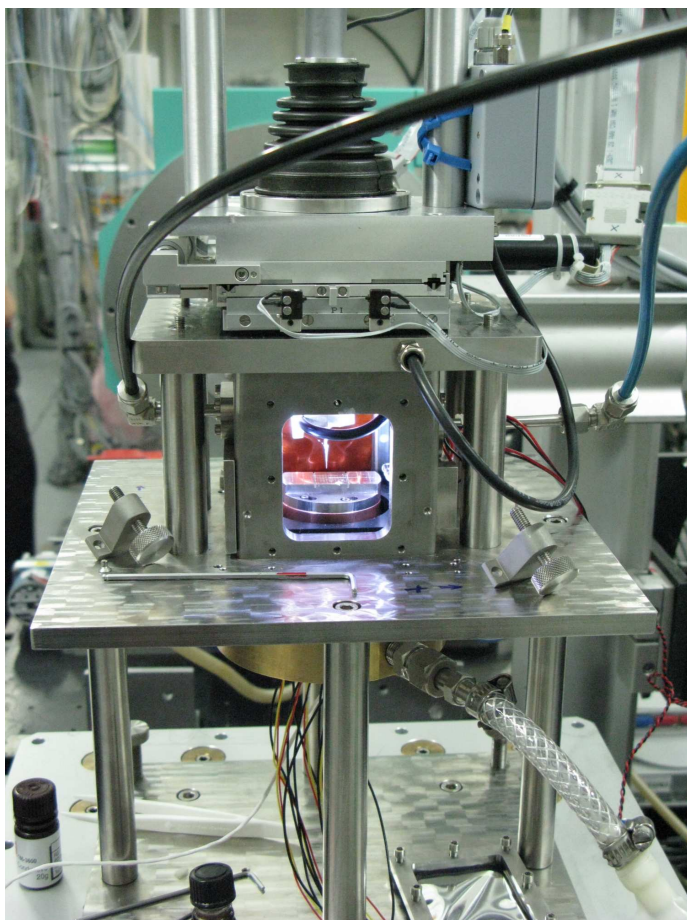
Figure 5.10: Picture of the mounted x-ray / Kelvin probe setup, taken from the direction of the incident beam. Through the open x-ray window, the Kelvin Probe tip can be seen above the bare sample holder.

Chapter 6

Data acquisition and analysis

6.1 Radiation damage

X-rays as a probe interact with the matter under investigation, and the incoming energy is partly dissipated. In particular in organic systems, this can evoke severe structural changes, i.e. radiation damage. This section briefly summarizes the radiation effects observed during reflectivity experiments and thereby motivates the measurement protocol presented in the forthcoming section. Possible causes and an interpretation of the temperature dependence will also be given.

Figure 6.1a compares two iterative reflectivity curves recorded over the same area of the $[\text{bmpy}]^+[\text{fap}]^-$-$\text{Al}_2\text{O}_3$ interface at $T = 120°\text{C}$: Upon irradiation, the layering feature broadened by $\approx 20\%$ (estimated by fitting Lorentzian peak shapes to these features), accompanied by a slight shift rightwards. Such smearing out of interference patterns is typical for radiation-induced structural changes when previously well-ordered structures get randomly disturbed. For an incident flux of $10^{14}\,\text{ph}\,\text{mm}^{-2}\,\text{s}^{-1}$, approx. $1\,\text{meV}$ are dissipated in one ion pair per second[1] – at least three orders of magnitude below the bond energies within the molecules. Hence, secondary effects, at this energy mostly stemming from ionizing Compton electrons, are likely to cause the radiation damage [136] (see Fig. 6.1b).

Monitoring the reflected signal at a defined momentum transfer in time (via so-called *timescans*) gives insights into the time scales of structural changes. Subsequent horizontal-translation scans perpendicular to the beam (*y* scans) reflect the spatial evolution of the damage. In Fig. 6.2, such scans are shown for the ionic liquid $[\text{hmim}]^+[\text{fap}]^-$ and two different temperatures, $T = 110°\text{C}$ and $T = -33°\text{C}$, at a momentum transfer of $q \approx 0.8\,\text{Å}$. The timescans in the left panel, both in agreement with an exponential saturation function (blue und green lines), disclose an immediate response of the signal to irradiation, saturating at about twice the initial value. The dynamics of this process, however, differ by almost an order of magnitude with time constants of $\tau = 76\,\text{s}$ at $T = -33°\text{C}$ and $\tau = 730\,\text{s}$ at $T = 110°\text{C}$. This gives evidence of drastically reduced radiation damage

---

[1] calculated for $72.5\,\text{keV}$ from mass energy-coefficients taken from Hubbell and Seltzer [135]
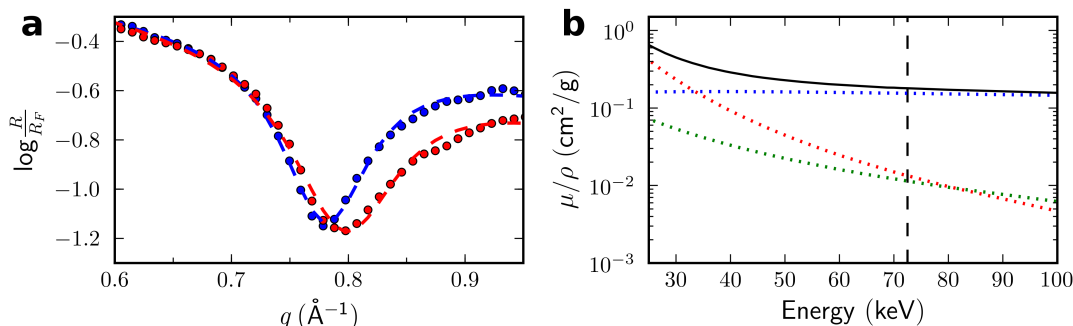
Figure 6.1: a) Reflectivity of $[\text{bmpy}]^+[\text{fap}]^-$ recorded at $T = 110°\text{C}$ for the first (blue) and third time (red) over the same substrate area. The dashed lines indicate Lorentzian line shapes fitted to the layering feature. Upon irradiation, the latter broadens by approx. 20% indicating a loss in interfacial order. b) Contributions of incoherent (blue dots) and coherent (green) scattering and of absorption (red) to the total mass attenuation coefficient of $[\text{bmpy}]^+[\text{fap}]^-$ (black solid line) versus photon energy.

at low temperatures, an effect well-known from electron microscopy studies of organic species [137–139]. Electron spin resonance has shown that not the ionizing radiation itself causes the damage, but the subsequent chemical redox processes which lead to bond rupture, cross-linking, etc. [140]. High temperatures speed up these reactions, hence promoting structural changes.

The right panel of Fig. 6.2 shows translation scans across the point of irradiation after $500\,\text{s}$ (circles, upper curve) and $900\,\text{s}$ (diamonds) of irradiation for the high temperature and after $1500\,\text{s}$ (circles, lower curve) for the low temperature. All curves exhibit a Lorentzian shape; the two datasets after different irradiation duration have almost the same FWHM, $\Gamma = \approx 90\,\mu\text{m}$, pointing towards a localized damage profile after saturation. A comparision with the low temperature profile yields an approx. 20% lower FWHM despite the longer irradiation time.

Similar radiation effects were observed for all ionic liquids even though their extent might vary individually. The immediate onset of imposed signal changes renders it impossible to exclude any impact on the recorded reflectivity data. Nevertheless, these changes are slow-evolving and, at least at first, even in the most sensitive regions of the reflectivity small in comparision to the layering features. In combination with the high diligence taken to minimize radiation damage, this should assure that the acquired data reflect the undisturbed structural arrangement to a high degree[2].
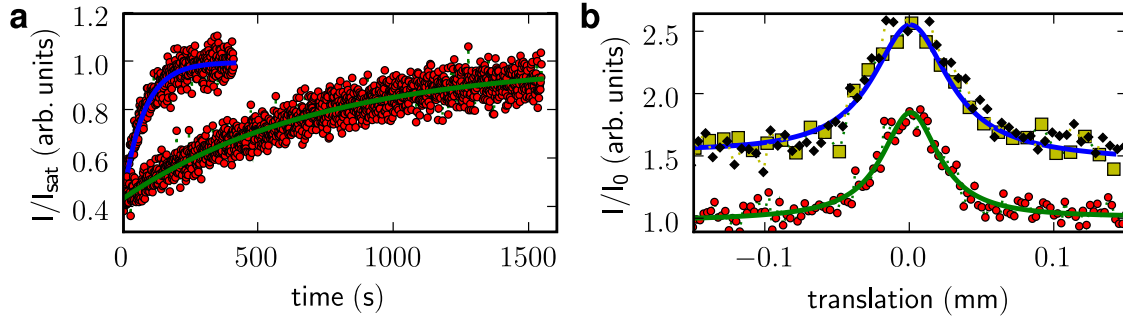
Figure 6.2: a) Time evolution of the reflected signal at $q = 0.82\,\text{Å}$ for $[\text{hmim}]^+[\text{fap}]^-$ together with fitted exponential saturation functions at $T = 110°\text{C}$ (blue) and $T = -33°\text{C}$ (green). b) Translation scans across the previously irradiated spots at the same temperatures with Lorentzian line shape fits. The curves for the high temperature, after $500\,\text{s}$ (green squares) and $900\,\text{s}$ (black diamonds), are shifted for clarity, the low temperature curve was recorded after $1500\,\text{s}$ of irradiation (see text for details).

#	2θ min	max	Δ	f_{abs}	sec.
3	0.0	0.2	0.005	5×10^4	2
4	0.08	0.48	0.01	4×10^3	2
5	0.24	0.6	0.005	12.5	2
7	0.4	1.1	0.05	1	2
6	0.9	1.8	0.05	1	5
1	1.02	1.62	0.05	1	5
2	1.03	1.63	0.05	1	5
8	1.6	2.2	0.05	1	10
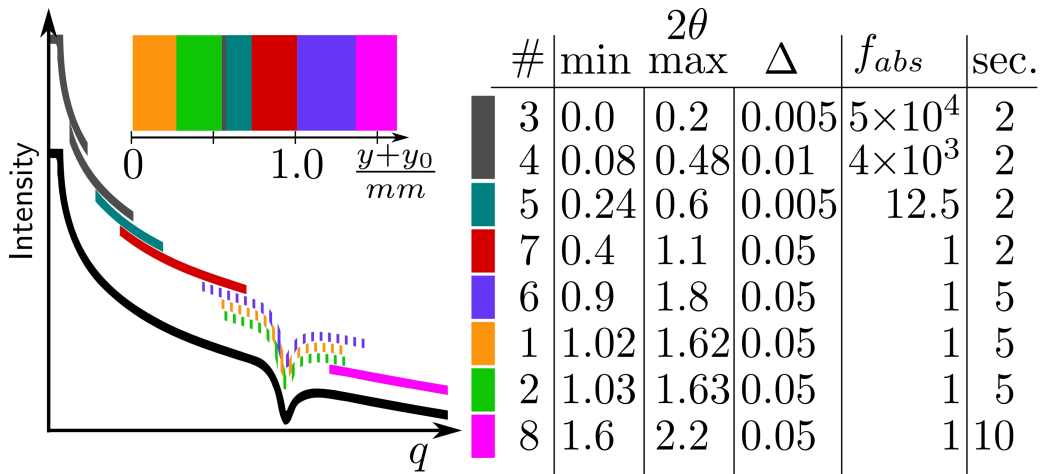
Figure 6.3: Illustration of the measurement protocol employed for the reflectivity measurements. The individual scans are represented by color-coded stripes of the reflectivity curve and shifted against each other for clarity. Overlaps in q space between adjacent scans simplify reassembling the overall curve (shown in black at the bottom) in the subsequent data treatment. The inset shows the segment each scan covers in the in the y direction via translation during recording in the corresponding color. Start, end, and step values for 2θ, the absorption factor, and the counting time per data point are listed in the adjacent table.

6.2   Measurement protocol

For reproducible data acquisition and in order to eliminate external effects caused by e.g. radiation damage or substrate inhomogeneities, an elaborated measurement protocol was set-up and followed at, at least, two different substrate positions for every IL. Several measures were taken to minimize the radiation load on the interface: In the low-q region, the absorber was in use as long as the count rates allowed for it. Irradiation time was limited to actual counting time by the fast shutter, and the samples were translated horizontally (in y direction, compare Fig. 5.3) between the acquisition of two adjacent points by at least one beam profile width. As an additional benchmark for homogeneity, the most sensitive region around the layering features was covered with three nested scans over different substrate regions (see Fig. 6.3). Table 6.1 sums up the technical key parameters of the x-ray reflectivity scheme.

Table 6.1: Technical parameters of the x-ray reflectivity scheme.

parameter	value
x-ray wavelength λ	0.171 Å
wavelength spread $\Delta\lambda/\lambda$	$2.3 \cdot 10^{-3}$
primary beam intensity	$5 \cdot 10^{10}\,\mathrm{photons\,s^{-1}}$
vertical detector slit opening	$350\,\mu\mathrm{m}$
horizontal detector slit opening	$350\,\mu\mathrm{m}$
vertical beam size b_v	$6\,\mu\mathrm{m}$ - $8\,\mu\mathrm{m}$
horizontal beam size b_h	$26\,\mu\mathrm{m}$
distance sample-detector	$1196\,\mathrm{mm}$
maximum vertical momentum transfer q_{max}	$1.5\,\mathrm{Å}^{-1}$
sample length d	$6\,\mathrm{mm}$

6.3   Raw data treatment

6.3.1   Correction factors

In a first data processing step, the recorded data need to be normalized to the primary beam intensity and corrected for detector deadtime (rf. to Eq. 5.1), beam footprint on the sample, and the absorption factor.

   The ring current delivered by the synchrotron constantly declines after injection, from a peak value of $200\,\mathrm{mA}$ typically to about $150\,\mathrm{mA}$ before the next injection. In addition, the primary intensity at the beamline is subject to variations due to small temperature changes inside the optics hutch, for instance. These external influences are readily compensated

---

[2] For an account of radiation-induced charging effects at the interface, the reader is refered to Sec. 9.2.

by normalizing the detector count rate to the current of the first monitor diode (compare Fig. 5.1).

At shallow incident angles, the incident beam profile exceeds the projection of the interface perpendicular to it. Hence, the reflected intensity is smaller than to be expected from the primary beam intensity. This can geometrically be corrected for by normalizing the reflected signal to the share of the intensity that actually hits the interface. For a Gaussian beam profile, which is a sound approximation of the focussed beam profile [89], the corresponding correction factor reads [105, 117]

$$f_{\mathrm{fp}} = \mathrm{erf}\left(\frac{d\sin\vartheta}{8\sqrt{\ln 2}\,b_{\mathrm{v}}}\right) \; . \tag{6.1}$$

In the low-q range, the PMMA absorber (rf. to Sec. 5.1.2) was in use to cover the required dynamic range, so the corresponding detector counts need to be multiplied by the absorption factor. These were estimated from absorber scans with the detector diode and fine-tuned by matching together overlapping reflectivity scans. The overview in Fig. 6.3 lists the absorber settings used in the measurement protocol.

6.3.2 Background

Two sources contribute to the background level of the recorded signal: external background arising mostly from scattering events within the beam path (air, optical elements, x-ray windows, etc.) and intrinsic scattering from the sample itself. The former can be suppressed to a few counts per second and is thus rendered insignificant except for very low count rates at high-q values. The intrinsic background, however, gives a significant contribution to the overall signal and stems mainly from bulk liquid scattering which is discussed in more detail in Sec. 4.2. Since the spatial correlations in the bulk and the interfacial structure of ionic liquids are closely linked (see Sec. 7.4), the dominant features of liquid-structure and reflectivity data coincide in q space, making a careful background acquisition and subtraction mandatory.

In order to accurately record the background as a function of the momentum transfer, the measurement protocol was repeated with the incident angle detuned by $\Delta = 0.03°$. Δ was chosen such that any influence from the specular reflectivity signal was avoided.

6.3.3 Regridding onto universal q space grid

Figure 6.4 shows the corrected reflectivity and background data for the $[\mathrm{bmpy}]^+\,[\mathrm{fap}]^-$ interface at $T = -15°\mathrm{C}$ (open circles). Background and signal are of the same order of magnitude in this peak region, resulting in drastic effects of the former on the corrected data. In order to minimize statistical noise and to extract all information obtainable, all data were carefully regridded onto an equidistant q-space grid using a weighted nearest-neighbors interpolation (full circles). This significantly reduces background noise whereas all features of both signal and background are preserved. The equidistant coverage of q space
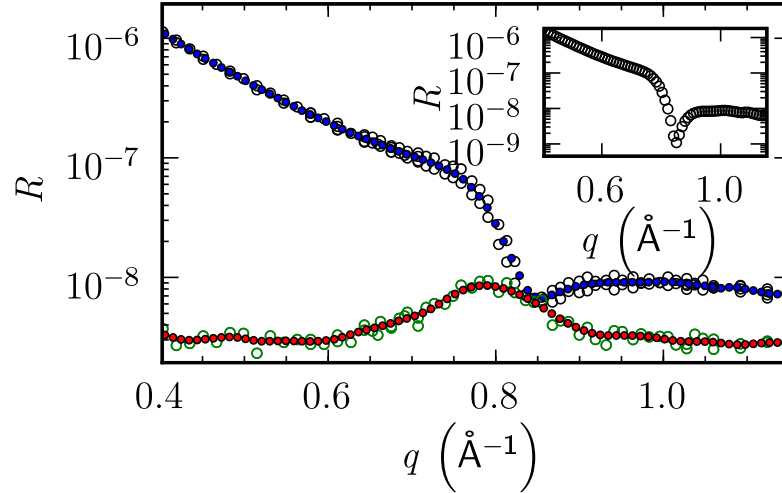
Figure 6.4: q-space regridding exemplified for $[\text{bmpy}]^+[\text{fap}]^-$ at $-15°C$: The open black and green circles represent the corrected reflectivity and background data, respectively. The full blue and red circles show the same data after averaging and regridding onto an equally spaced q grid. The statistical background noise is significantly reduced while all structural features are preserved.

eliminates artificial weighting factors arising from different sampling densities. Furthermore, it is not necessary to have a point-wise match between reflectivity and background data, hence simplifying and speeding up experimental runs.

Appropriate regridding parameters were adjusted manually: Δq was set to the minimum of the sampling rate in the layering region (scans no. 1, 2, and 6; see Fig. 6.3) to avoid over-sampling on the one, and over-weighting of the low-q region on the other hand. A second order polynomial was chosen for the interpolation algorithm. The standard deviation defining the Gaussian weighting distribution around the grid point to be interpolated was empirically optimized to $1.2\,\Delta q$ for reflectivity and $2.0\,\Delta q$ for background data.

6.4 Extracting real space profiles from reflectivity data

Knowing the real-space electron density profile perpendicular to an interface, $\rho(z)$, the x-ray reflectivity emerging from it could be readily calculated using the sliced Parratt formalism described in Sec. 4.1.4. Vice versa, however, a unique and straight-forward determination of the real-space structure from reflectivity data is not possible due to the loss of phase information in the recorded intensity, $I \propto |Ee^{i\Phi}|^2$. Instead, the profile needs to be parametrized with a set of fitting parameters that are subsequently fed into a fitting algorithm to find the best match to the experimental data. A physically meaningful parametrization requires additional knowledge on the system, such as bulk electron densities, feasible model assumptions on the generic structure, and a restrictive use of free

fitting parameters reflecting the feature richness of the data to avoid ambiguities. It follows directly from the recursive Parratt formalism that either the density of the topmost or the bottom layer needs to be known in any case.

In the following sections, first the definition of an appropriate cost function and the implemented fitting approach are introduced, before a density model to describe the interfacial layering of ionic liquids is discussed.

6.4.1 Cost function

Typically, the cost function to be minimized by the fitting algorithm is set to the sum of the quadratic deviations between experimental and calculated data points (method of least squares):

$$\chi^2 = \sum_{i=1}^{N} \left(I_{i,exp} - I_{i,calc} \right)^2 \tag{6.2}$$

The large dynamic range covered in x-ray reflectivity experiments (up to nine orders of magnitude in this work), however, makes scaling necessary if sensitivity of the fit over the whole curve is desired. One possibility is to divide every summand in Eq. 6.2 by the Fresnel reflectivity at the corresponding momentum transfer, $R_F(q_i)$. Even though this drastically reduces the dynamic range of the data to be fitted, the observed layering features might still extend over two or three orders of magnitude. For this reason, the cost function used in this work was defined via logarithmic deviations:

$$\chi^2 = \min_{\alpha} N^{-1} \sum_{i=1}^{N} \left(\ln \left(\alpha I_{i,exp} \right) - \ln I_{i,exp} \right)^2 \tag{6.3}$$

α is a normalization factor for the experimental data allowing the fit to adjust the total reflection level and making the parameter refinement more robust against misalignmet and normalization errors due to beam hardening. It is chosen such to minimize the cost function after each iteration of the fitting procedure, hence not a free fitting parameter. With $\delta_i = \ln I_{i,exp} - \ln I_{i,exp}$, Eq. 6.3 can be simplified to

$$\chi^2 = \min_{\alpha} N^{-1} \sum_{i=1}^{N} \delta_i + \ln \alpha \tag{6.4a}$$

$$= \langle \delta^2 \rangle - \min_{\alpha} \left[(\ln \alpha)^2 + 2 \ln \alpha \langle \delta \rangle \right] \tag{6.4b}$$

$$= \langle \delta^2 \rangle - \langle \delta \rangle^2 . \tag{6.4c}$$

In order to prevent numerical errors, the initial value for the constant $\ln \alpha = -\langle \delta \rangle$ in each iteration step is set to the final value of the preceeding step, so $\langle \delta \rangle^2$ is always small in comparision to $\langle \delta^2 \rangle$ in the end phase of the refinement algorithm.

6.4.2   Optimization procedure

Setting out from an initial guess, the cost function defined above needs to be globally minimized in the multi-dimensional parameter space. Deterministic approaches such as the popular *Levenberg-Marquardt algorithm* (LMA) [141] get easily stuck in local minima if the initial guess is too far away from the global minimum. Here, global optimization strategies prove to be superior although requiring much more computational capacity[3]. Among others, the Monte Carlo approach of *Simulated Annealing* (SA) is well-suited to find a global minimum[4]. As the name suggests, it adopts the manner in which metal crystals reconfigure towards equilibria in the process of annealing to the search for the lowest point in the landscape spanned by the const function. The thermal energy, allowing to leave energy valleys in the physical process, is replaced by a $\Delta\chi^2$ that is systematically reduced during the refinement. Given an appropriate annealing strategy, SA asymptotically converges to the global minimum [143].

In this work, the *Adapted Simulated Annealing* algorithm [144] was used. Based on the flexible framework by Mezger in our group [124, 145], the binary distorted crystal model was implemented into the code together with the afore-described regridding routine (Sec. 6.3.3).

6.4.3   Binary distorted crystal model

As has already been elaborated on in Sec. 2.4, two fundamentally different types of interface-induced order are thinkable for ionic liquids at a hard wall: ionic-counterionic layering and checkerboard layering – both decaying towards the bulk liquid. The model for the electron density profile discussed here, the *binary distorted crystal model*, accounts for the molecular nature of the system in its most generic form and facilitates representations of these two layering archetypes. Foundation of the model is the distorted crystal model successfully employed in the description of the surface of single-component liquid metals which describes the density across the interface as the sum of equally spaced Gaussian density distributions of increasing widths [45, 49, 146, 147] (see Sec. 2.5.1). This model was adopted to ionic liquids by combining two alternating Gaussian-sum density distributions corresponding to the cation (c) and anion (a) distributions, respectively. The area densities of each Gaussian,

$$\rho_{c,a} = d\,Z_{c,a}\rho_m N_A/M_{c,a}\,, \tag{6.5}$$

reflect the molecular share of each ion species and preserve charge neutrality. Scaling it with the layering periodicity[5], d , preserves the volume density of the ionic liquid. $Z_{c,a}$ is the number of electrons of the respective ion, $M_{c,a}$ its molar mass, ρ_m the bulk mass

---

[3] Parameter refinement took up to several hours with the implemented approach as compared to seconds with LMA.

[4] An instructive overview over common global optimization strategies can be found in [142].

[5] the spacing between subsequent Gaussians of the same species
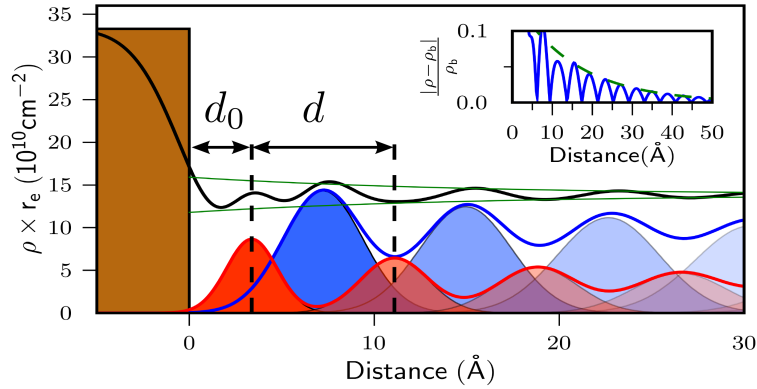
Figure 6.5: Cation (red), anion (blue) and total (black) electron densities obtained from the best fit to the $[\text{bmpy}]^+[\text{fap}]^-$ data at $T = -15°\text{C}$. Red/blue: cation/anion Gaussian distributions contributing to the respective partial electron density profiles (solid lines). Brown bar: electron density of the sapphire substrate without roughness. The exponentially damped envelope function of the resulting total profile is shown in green. In the inset, the modulus of the reduced deviation from bulk density is given.

density, and N_A is Avogadro's constant. The intrinsic ion structures and the initial degree of order is included in the starting values, $\sigma_0^{c,a}$ of the Gaussian standard deviations,

$$\sigma_n^{c,a} = \sqrt{(\sigma_0^{c,a})^2 + n\sigma_b^2}, \; n = 0 \dots \infty. \tag{6.6}$$

σ_b controls the broadening of the Gaussians with increasing distance from the interface. Together with an error function profile modelling the IL-sapphire interface, the overall parametrization of the electron density profile perpendicular to the interface reads

$$\rho(z) = (2\pi)^{-1} \sum_{n=0}^{\infty} \left[\frac{\rho_c}{\sigma_n^c} e^{-\frac{1}{2}\left(\frac{d_0 + nd - z}{\sigma_n^c}\right)^2} \right. $$
$$\left. + \frac{\rho_a}{\sigma_n^a} e^{-\frac{1}{2}\left(\frac{d_0 + (n+\epsilon)d - z}{\sigma_n^a}\right)^2} \right] + \rho_s \text{erf}\left(\frac{-z}{\sqrt{2}\sigma_s}\right). \tag{6.7}$$

ρ_s represents the substrate density and σ_s the interfacial roughness. The offset of the first Gaussian layer from the interface is given by d_0. The introduction of the symmetry parameter ϵ allows to move continuously from checkerboard layering, $\epsilon = 0$, to ionic-counterionic layering with either the cation, $\epsilon = 0.5$, or the anion next to the interface, $\epsilon = -0.5$.[6] Values between -0.5 and 0.5 represent intermediate states with a certain degree of polarization.

Figure 6.5 illustrates the composition of the total electron density of the partial ion densities across the interface.

---

[6] The latter case results in a shift of the actual first layer offset: $d_{0,\text{new}} = d_0 - 0.5d$
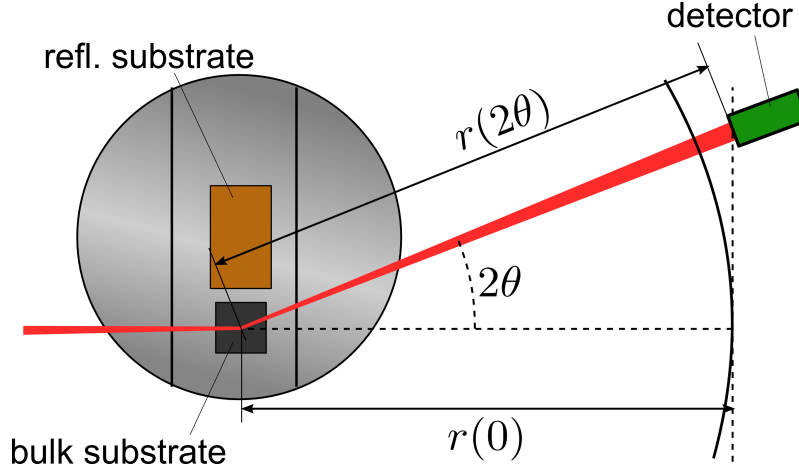
Figure 6.6: Top-view sketch of the bulk liquid scattering setup. See text for details.

6.5 Bulk liquid scattering scheme

The bulk liquid scattering measurements were carried out using the same experimental setup and sample environment as for the reflectivity experiments: Next to the sapphire substrate, a Si wafer piece ($5\,\mathrm{mm} \times 5\,\mathrm{mm}$) was placed and completely covered with ionic liquid. The beam was positioned horizontally in the center of the Si substrate and penetrated the liquid $50\,\mu\mathrm{m}$ above the interface. The detector was translated horizontally during acquisition, recording momentum transfers up to $q = 2\,\text{Å}^{-1}$ with a resolution of $0.016\,\text{Å}^{-1}$.[7] Figure 6.6 shows a sketch of the bulk liquid scattering scheme.

The acquired raw data was normalized to the primary beam intensity and corrected for absorption in the ionic liquid, for the solid angle, and for polarization. Multiple scattering events and Compton scattering were not considered. The correction factor for the absorption in the liquid, $A(2\theta)$, depends on where along the beam path the scattering event occurs. Integration over all possible pathes yields [148]

$$A(2\theta) = \frac{\int_0^d \exp\left[-\mu\left(d - x(1 - \frac{1}{\cos 2\theta})\right)\right]dx}{\int_0^d dx} \tag{6.8}$$

$$= \frac{\exp(-\mu d)}{\mu d\left(\frac{1}{\cos 2\theta} - 1\right)}\left\{1 - \exp\left[-\mu d\left(\frac{1}{\cos 2\theta} - 1\right)\right]\right\}. \tag{6.9}$$

μ is the linear attenuation coefficient calculated from the NIST database [108], d the sample thickness ($5\,\mathrm{mm}$), and x the position of the scattering event within the sample, $x = 0 \ldots d$.

Since the detector is moved perpendicular to the incident beam during acquisition, the sample-detector distance, $r(2\theta)$, is a function of the scattering angle, 2θ. The correspond-

---

[7] The vertical and horizontal detector slit openings were set to $4\,\mathrm{mm}$ and $1\,\mathrm{mm}$, respectively; the counting time was $5\,\mathrm{s}$ per data point. Refer to Tab. 6.1 for technical parameters not specified here.

ing solid angle spanned by the horizontal and vertical slit openings, a and b is given by [149]

$$\Omega = 4 \arcsin \frac{ab}{\sqrt{\left(4 \left(r(2\theta)\right)^2 + a^2\right) \left(4 \left(r(2\theta)\right)^2 + b^2\right)}} \,. \tag{6.10}$$

The measured intensity was divided by the fractional area, $\Delta A = \Omega/4\pi$.

For the used scattering geometry, the polarization factor, P, reads

$$P = P_\mathrm{o} + P_\mathrm{i} \cos(2\theta) \,, \tag{6.11}$$

with $P_\mathrm{i} = 0.05$ and $P_\mathrm{o} = 0.95$ the estimated fractional polarizations within the horizontal plane and perpendicular to it.

Part III

Results and discussion

Chapter 7

Temperature dependence and cation variation

7.1 $[\text{bmpy}]^+[\text{fap}]^-$

During three different experimental beamtimes using three separately purchased charges of ionic liquid, reflectivity data from the $[\text{bmpy}]^+[\text{fap}]^-$- sapphire interface were acquired at four different temperatures[1] : $-15°$C (supercooled), $8°$C (around the melting point), $66°$C, and $110°$C. Figure 7.1 shows the resulting corrected reflectivity curves. All four curves feature a pronounced dip at a momentum transfer of $q_0 \approx 0.8\,\text{Å}^{-1}$, which implies a distinctive layering perpendicular to the interface with a periodicity $d \approx 2\pi/q_0 \approx 8\,\text{Å}$. By trend the dip position shifts slightly leftwards with increasing temperature, from $q_0 = 0.85\,\text{Å}^{-1}$ at $-15°$C to $q_0 = 0.78\,\text{Å}^{-1}$ at $110°$C while its width broadens simultaneously. This behavior can qualitatively be attributed to an increase in layer spacing driven by thermal expansion and to a decrease in layering strength reflected in the smearing of the layering feature. At first glance, this trend is broken at $66°$C with a shift rightwards from the dip at $8°$C. But upon closer inspection it becomes obvious that rather the reflectivity at $8°$C does not fit into the scheme with its large dip shift in comparison with the small temperature change. Here, the layering feature also appears to be as sharp as or even sharper than at the lowest temperature.

7.1.1 Real space profiles from parameter refinement

The reflectivity data were used to fit the model parameters introduced in Sec. 6.4.3 and thereby extract real space profiles of the ionic liquid-sapphire interface. Six free parameters were optimized in a q range from $0.25\,\text{Å}^{-1}$ to $1.05\,\text{Å}^{-1}$:[2] the layer spacing, d, the first layer offset, d_0, the starting widths of the Gaussians, σ_0^c and σ_0^a, the decay parameter,

---

[1] The highest and the lowest temperature points were probed during the first beamtime, the intermediate ones during two subsequent sessions.

[2] This range was chosen empirically to maximize the fit's sensitivity to the characteristic dip feature while still taking account of the slope of the reflectivity's smooth part.
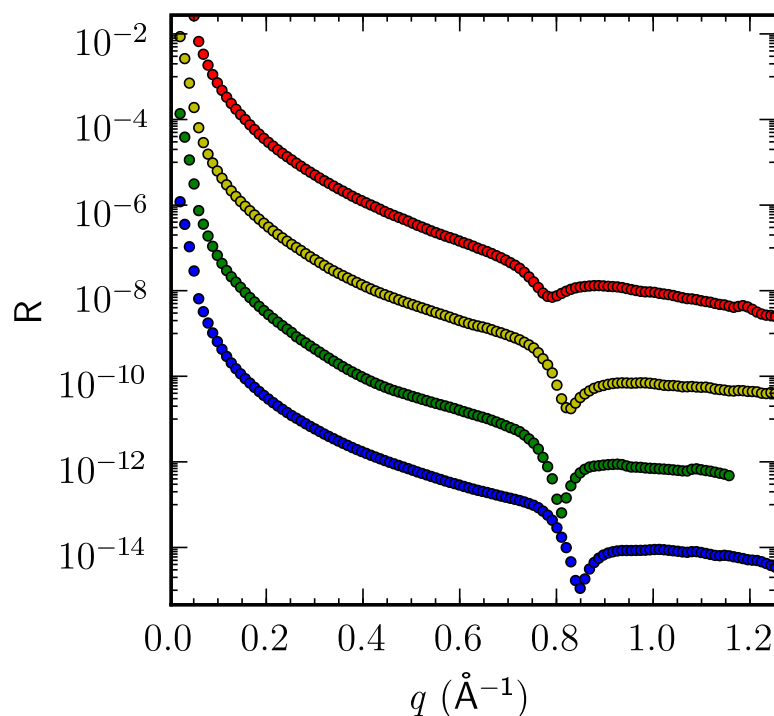
Figure 7.1: Corrected reflectivity curves of the [bmpy]$^+$[fap]$^-$-sapphire interface recorded at $110°$C (red), $66°$C (yellow), $8°$C (green), and $-15°$C (blue) versus vertical momentum transfer q. The curves are shifted by two orders of magnitude against each other for clarity.

σ_b, and the interfacial roughness, σ_r. With the ionic liquid's bulk density determined from pycnometry measurements (Sec. 5.3.1), one important degree of freedom remains, the positional arrangement of the ionic layers with respect to the interface. Both cation and anion starting layers were tested, as well as checkerboard layering and intermediate (asymmetric) states. The systematic response of the recorded signals to an increase in temperature provides an ideal test for the consistency of this fitting approach and adds significantly to the robustness of the outcome.

The best fit results for all data were obtained for a symmetric ionic layering starting with a cation layer. These fits are discussed in detail in the next section, followed by a careful treatment of the sensitivity of the fitting routine to individual parameters and the error bars derived from it. Finally, the fit quality will be compared to other positional arrangements, underlining the unambiguousness of the overall picture emerging from the parameter refinement.

Best fits to the data

The fit quality of cation-triggered ionic layering was not only at every temperature point superior to all other arrangements, but in addition solely yielded a parameter set that
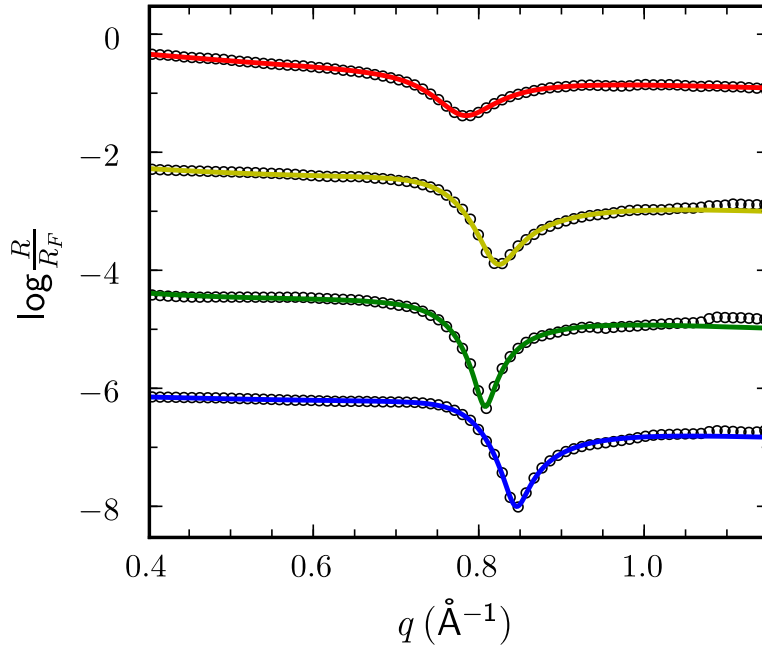
Figure 7.2: Best fits to the reflectivity data from the $[\mathrm{bmpy}]^+[\mathrm{fap}]^-$-interface, obtained for cation-triggered ionic layering at $110°\mathrm{C}$ (red), $66°\mathrm{C}$ (yellow), $8°\mathrm{C}$ (green), and $-15°\mathrm{C}$ (blue). In order to put emphasis on the layering feature, the curves are shown normalized by the Fresnel reflectivity, R_F. For clarity, they are shifted against each other.

evolves consistently with temperature. Figure 7.2 shows the excellent agreement of the resulting reflectivities to the data. The extracted electron density profiles for the partial ionic profiles have already been shown in Fig. 6.5 for the lowest temperature. In Fig. 7.3, the moduli of the deviations from bulk density for all four temperatures are shown on a logarithmic scale together with fitted exponential envelope functions to the profiles. The latter are proportional to $e^{-z/\xi}$. ξ is the decay length of the interfacial layering, which is related to the broadening parameter σ_b of the layering model. It decreases linearly from about $16\,\mathring{\mathrm{A}}$, or approx. two double layer spacings, d, at the lowest temperature, to about $13\,\mathring{\mathrm{A}}$, or approx. $1.6\,d$, at $T = 110°\mathrm{C}$. At the same time, d increases in accordance with thermal expansion. A free symmetry parameter ϵ (compare Sec. 6.4.3) only resulted in insignificant deviations from the fully symmetric configuration, $\epsilon = 0.5$, without improving the fit quality; so this parameter was kept fixed in order to improve the fit stability.

A graphic representation of the parameter evolution with temperature is given in Fig. 7.4 for all six free parameters. The linear fits to the data, depicted as solid blue lines, indicate a consistent response of d, ξ, σ_0^a, and d_0 to temperature changes and give no evidence for any transition when crossing the ionic liquid's melting point, $T_M = 4\,°\mathrm{C}$. While the temperature effect on the former three parameters can readily be attributed to thermal expansion and an increase in entropy, respectively, the declining or, within error margins, at
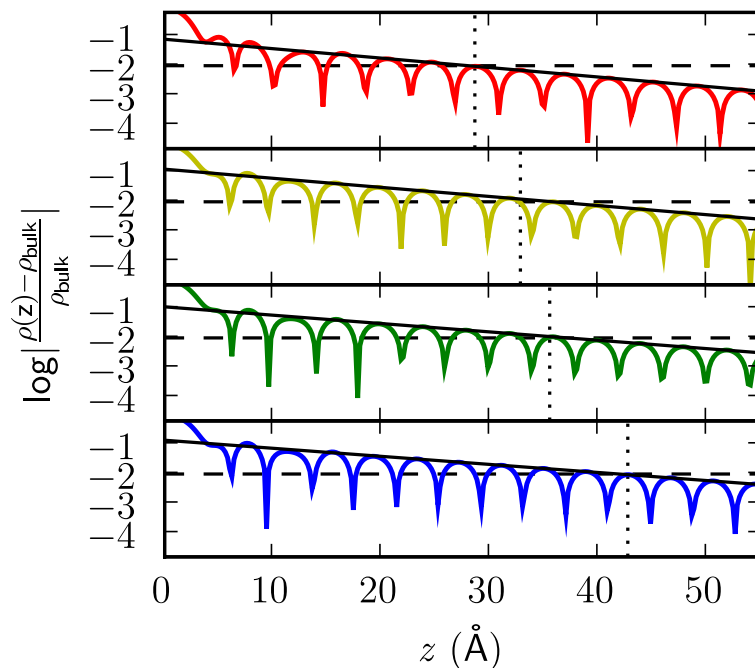
Figure 7.3: Extracted electron density profiles perpendicular to the $[\mathrm{bmpy}]^{+}[\mathrm{fap}]^{-}$-sapphire interface at $110°$C (red), $66°$C (yellow), $8°$C (green), and $-15°$C (blue). For the purpose of comparison, the absolute deviations from bulk density are shown on a logarithmic scale, and a significance threshold, set to 1% deviation from bulk density, is given (dashed lines). The decay in layering strength is clearly visible in the decreasing slope of the fitted exponential envelope functions to the profiles (solid black lines).

best constant first layer offset, d_0, discloses a rather unanticipated behavior. It implies that the first molecule's potential well has a more shallow slope on its sapphire side, causing the average position to shift towards the interface with increasing thermal energy.

The parameters σ_c and σ_a model the initial laterally averaged disorder of $[\mathrm{bmpy}]^{+}$ and $[\mathrm{fap}]^{-}$, respectively, convoluted with the molecules' intrinsic structure perpendicular to the interface. The FWHMs of the Gaussian density distributions in the first double layer, approx. $2.35\,\sigma_0^{a,c}$, can be compared to the structural dimensions of the two ions to test the plausibility of the obtained interfacial configuration. Figure 7.5a juxtaposes the molecular structures with the fit results, displaying the feasibility of the latter. The well-matching dimensions suggest a high degree of initial order since the predominant part of the Gaussian widths can be assigned to the structure.

A closer analysis of the graphs of d, d_0, and σ_0^a versus temperature reveals systematic deviations of the $8°$C data points from linearity. This confirms the irregularities already observed in the reflectivity data (compare Fig. 7.1). In particular, the deviation in the double layer spacing, d, is striking. It is directly correlated to the layering feature's unsystematically strong shift towards lower q values. At the same time, the ratio between
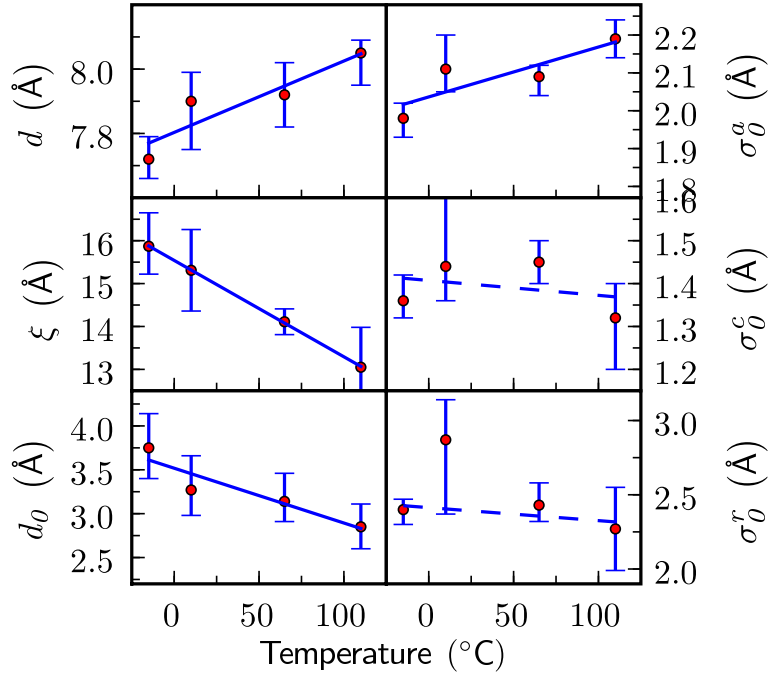
Figure 7.4: Evolution of all model parameters from the $[\mathrm{bmpy}]^+[\mathrm{fap}]^-$-sapphire interface versus temperature together with linear regressions (blue lines). The error bars represent a confidence interval of 30% around the cost function's minimum, obtained from parameter space maps with respect to the individual parameters (see Sec. 7.1.1).

d_0, essentially being a phase shifter acting on the reflectivity, and d is the key quantity determining the shape of the feature. In Fig. 7.5b, d_0 and d from the best fit (red curve) are gradually changed towards the values obtained from the linear fits to the other temperature data while keeping all other parameters constant (blue curve). The resulting curve now fits almost perfectly into the scheme, supporting the connection drawn between reflectivity data and fit outcome.

   With the obious explanation, a melting point transition, ruled out owing to the linearity of the remaining three data points, two other causes for this anomaly are conceivable: The samples stem from different charges of ionic liquids; minor differences, e.g. caused by differing ages of the liquid[3], might have given rise to slightly different interfacial arrangements. Another source for contamination arises from the transfer of the substrates to the sample stage during which they inevitably are exposed to environmental atmosphere for several minutes. Slight changes in its composition might have resulted in a different substrate termination in this particular case. Despite this noticably unsystematic behavior

---

[3] Although the ionic liquids used in this work can be considered as very stable, slow chemical degradation cannot be excluded. The high consistency of the data from three separate experimental campaigns, however, proves the reproducible quality of the samples.
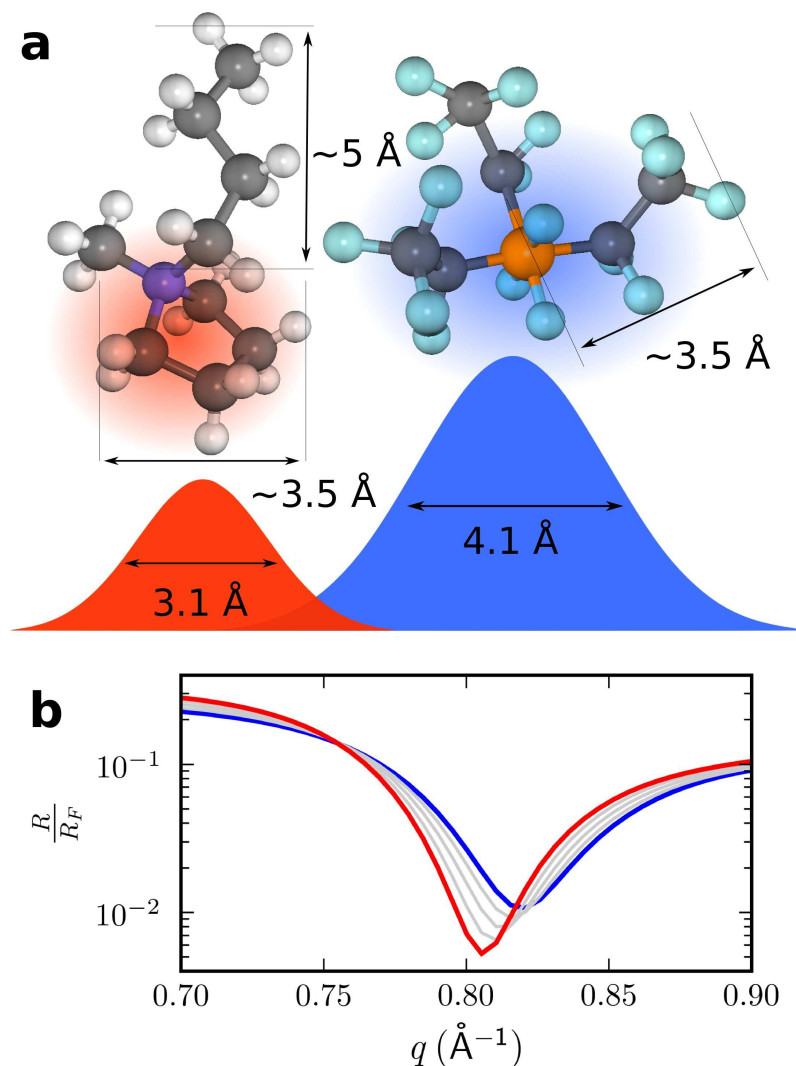
Figure 7.5: a) Comparision of the molecular dimensions of the $[\text{bmpy}]^+$ and $[\text{fap}]^-$ molecules to the Gaussian density profiles in the first interfacial adlayers, derived from the best fit at $-15°$C. Typical distances in the molecular structures as well as the Gaussian FWHMs are indicated. b) Simulated evolution of the reflectivity at $8°$C from the best fit (red curve) to the curve derived from the parameter evolution of d_0 and d of the remaining three temperatures (blue curve; compare Fig. 7.4); all other parameters were kept constant. The thin gray lines represent intermediate steps between the two endpoints.

and the uncertainty it induces, however, it is worth pointing out again the remarkable consistency of the fit results given the complexity of the multi-dimensional parameter space optimization.

Fit sensitivity and error analysis

Error bars for fit parameters in an optimization problem and cross-correlations between the individual parameters are typically defined via the covariance matrix, where the diagonal elements represent the absolute square of the standard deviations and the non-diagonal elements (i, j) the covariances between paramters i and j. For the popular Levenberg-Marquardt algorithm, an estimate of the covariance matrix can be derived from the final approximation of the Jacobian matrix [150]. The Monte Carlo approach of Adaptive Simulated Annealing employed in this work, however, does not provide such means of error analysis. Error bars were therefore defined from the cost function's response to variation of individual parameters around their minima instead. In this region, the slope of the ascent of the cost function reflects the sensitivity of the fitting model to this particular parameter. Though it is not possible to derive error bars in terms of probability from these slopes, the introduction of confidence intervals within which the cost function stays below a defined relative threshold allows for comparing the parameter sensitivities both within one set of parameters as well as across different sets, e.g. at different temperatures. For the present data analysis, the confidence threshold was set to $1.3 \times \chi_{min}$; hence the error bars given represent the fit parameter values in a cost function range of $30\,\%$ around the best fit. At this cut-off, a significant decrease in fit quality was observable for all data.

The parameter space sampling for the error analysis was performed by successive fitting runs with the parameter in question pinned to a series of values around the best fit while the other parameters were kept free. In doing so not only the parameter's sensitivity but also its cross-correlations with the other parameters were mapped as is exemplified for the broadening parameter, σ_b, at $T = -15\,^\circ\mathrm{C}$ in Fig. 7.6. The lower panel shows that all fit parameters are practically constant versus σ_b in the confidence interval, giving evidence for the robustness of this model parameter in this particular case.

Generally speaking, the parameters d and σ_b exhibit similar robustness for all four temperatures, whereas the Gaussian starting widths, $\sigma_0^{c,a}$, are closely correlated as well as σ_0^c, d_0, and σ_r. In particular the latter is intuitively understood since these three parameters can manipulate a prominent feature in the electron density profile, the depletion width and depth at the interface, and each can partly compensate for changes induced by the other two. σ_r and d_0, for instance, are positively correlated as can be seen in Fig. 7.7: An increasing roughness smears out the depletion zone which in turn can be compensated for by increasing d_0 as well. Such correlations need to be taken into account when discussing the robustness of the concerned fitting parameters. In contrast to d and σ_b, definite statements on the accuracy of d_0 cannot be made.

As mentioned above, the ionic liquid's bulk density was determined independently and thus not included as a free parameter in the model. Nevertheless, its value is of great importance for the reflectivity curves generated from the density profiles since it defines the contrast at the step between the sapphire and the liquid. The experimental uncertainties of the density as well as of the interfacial temperature add up to an overall uncertainty of the density fed into the parametrization well below 1% around its nominal value. In order to exclude any influence on the results stemming from this uncertainty, the parameter space
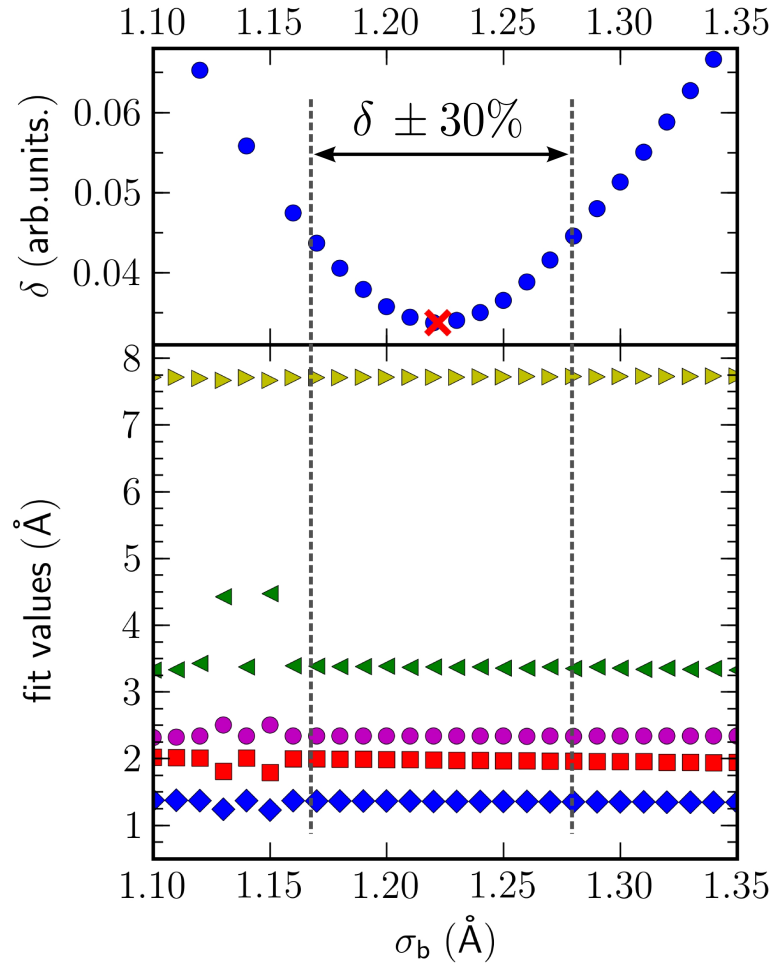
Figure 7.6: Error analysis for the broadening parameter, σ_b, at $T = -15\,^\circ\text{C}$ on the basis of a one dimensional parameter space map along the σ_b direction ($[\text{bmpy}]^+[\text{fap}]^-$-sapphire interface). Upper panel: cost function, χ, versus σ_b; the confidence interval of $30\,\%$ around the best fit, χ_{min}, is depicted by the vertical bars. Lower panel: evolution of the other model parameters versus σ_b.

was also mapped around the nominal density, ρ_0, as shown in Fig. 7.8 for the lowest temperature. The upper panel depicts the cost function, χ, versus the normalized bulk electron density, ρ/ρ_0, (blue circles) together with $\chi(\rho_0)$ (red cross). The cost function describes a very shallow negative slope, displaying that the fit drives the density towards unphysical values when kept free. At the same time, all other parameters remain constant. This indeed negates any influence of wrong bulk density values on the fit parameters, which not only holds for this example but for all temperatures, and underlines the importance of the fixed density on the fit stability.
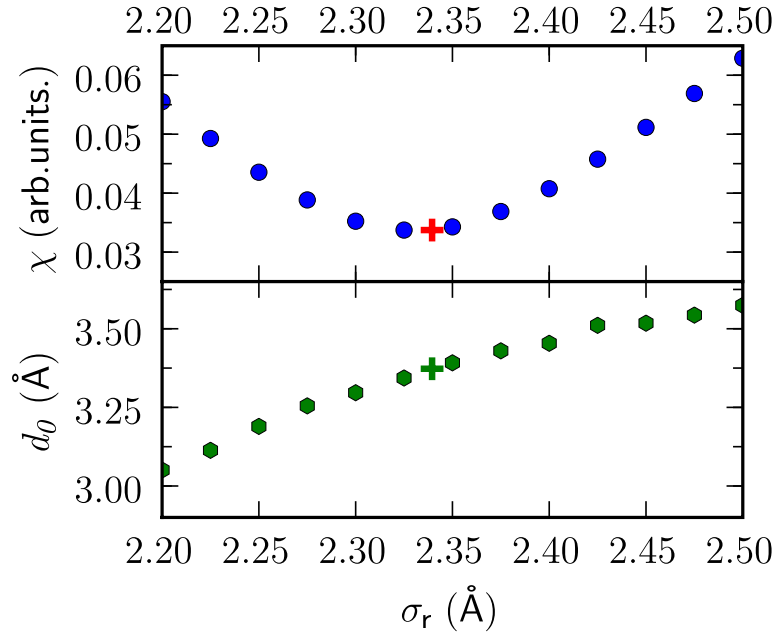
Figure 7.7: Correlation of the interfacial roughness, σ_r, and the first layer offset, d_0, on the basis of a one dimensional parameter space map along the σ_r direction at $T = -15\,°C$ ([bmpy]$^+$[fap]$^-$-sapphire interface). Upper panel: cost function, χ, versus σ_r. Lower panel: evolution of d_0 versus σ_b.

Comparison to other positional arrangements

The best-fit result of a cationic starting layer at the interface is supported by independent SKP measurements of the irradiated sapphire-vapor and sapphire-IL interfaces (Sec. 9.2). Nonetheless, different positional arrangements were thoroughly evaluated and compared to the outcome presented above (Fig. 7.9).

Despite the difference in the partial densities of [bmpy]$^+$ and [fap]$^-$ – ρ_c is about one third of ρ_a – the differences in the resulting electron density profiles extracted from "cation first" or "anion first" parametrization, respectively, remain small in comparison to the large step induced by the sapphire surface. Given the six degrees of freedom of the density model, very much the same profiles can be constructed with either configuration. Hence, it is quite unlikely that robust conclusions can be drawn from the analysis of one independent data set. The left and middle panels of Fig. 7.9 illustrate this issue for the lowest temperature (lower panels and blue curves in the upper panels): Both fits to the data are decent and practically not distinguishable by eye, both fit parameter sets appear reasonable, and also the resulting electron density profiles look very similar despite the different starting ion. However, the "anion first" configuration could be ruled out solely from the reflectivity data analysis with high confidence thanks to the availability of a consistent temperature series. Aside from the fact that the reflectivity features at the highest temper-
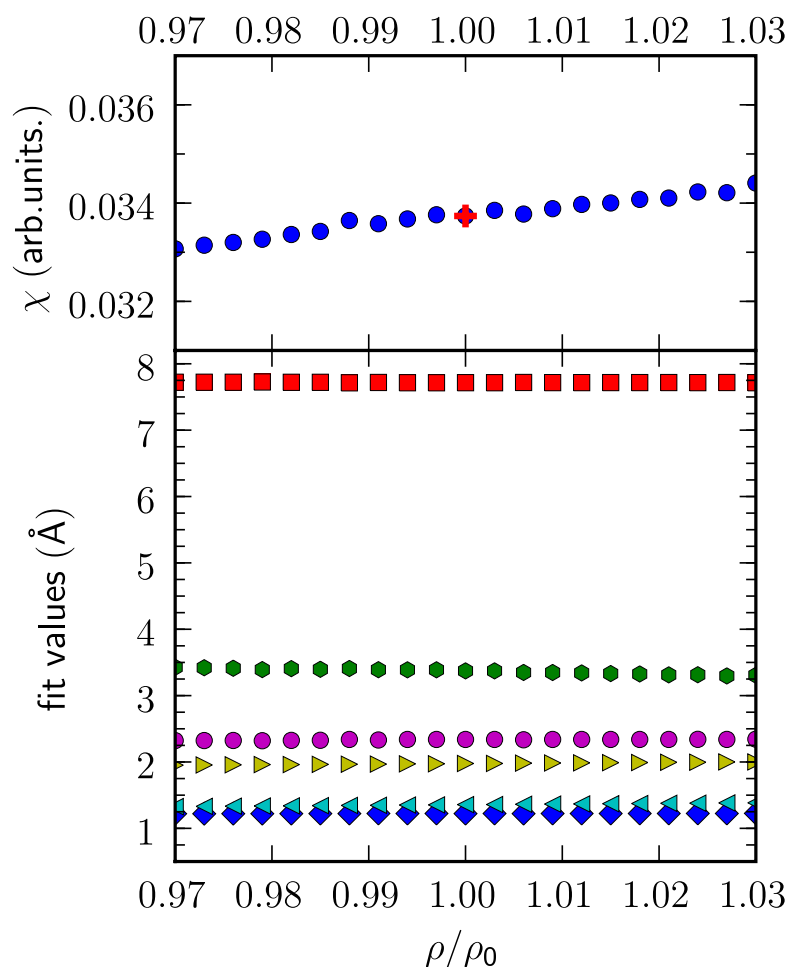
Figure 7.8: Correlation of the ILs bulk density, ρ_0, and the other fit parameters, d_0, on the basis of a one dimensional parameter space map along the σ_r direction at $T = -15\,°\mathrm{C}$ ($[bmpy]^+[fap]^-$-sapphire interface). Upper panel: cost function, χ, versus ρ_0. Lower panel: evolution of the other parameters versus ρ_0.

ature could not satisfactorily be reproduced (red curve in the upper right panel of Fig. 7.9), the parameter evolution with temperature is by far not as self-consistent as in the "cation first" case.

Compared to the nuances distinguishing the two double-layer configurations from each other, the differences between checkerboard and "cation first" configuration are rather big due to the inherently distinct spatial arrangement of the ions. Two implementations of checkerboard layering were tested against the experimental data: a) with the Gaussian distributions aligned on top of each other while preserving their distinct starting values,
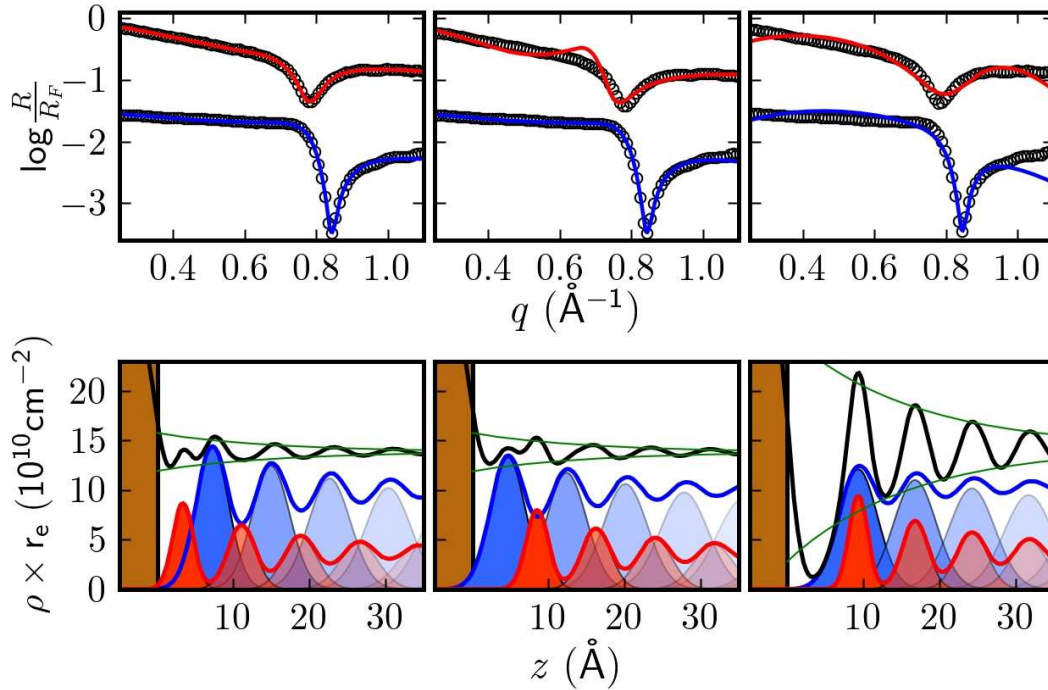
Figure 7.9: Comparison of low and high temperature fits (top panels; blue and red lines) and the resulting low temperature density profiles for different model parametrizations (bottom panels) at the $[\text{bmpy}]^+[\text{fap}]^-$-sapphire interface. Left: cation starting layer; middle: anion starting layer; right: checkerboard layering. See text for details on the different models and Fig. 6.5 for an assignment of the objects in the density profiles.

and b) a simplified model with just one Gaussian distribution for both ions[4]. While model b generally failed to reproduce the data, model a could decently fit some of the data sets even though the fit quality was still considerably lower than for the "cation first" case; the upper right panel of Fig. 7.9 shows the fits for lowest and highest temperature. The resulting profiles, however, exhibited either a very large depletion layer of at least $d_0 = 10$ Å (compare right lower panel of Fig. 7.9), or a significant density excess on the substrate side. Both of these features are physically unfeasible, clearly ruling out a checkerboard configuration at the ionic liquid-sapphire interface.

7.2 Cation variation 1: $[\text{hmim}]^+$ and $[\text{tba}]^+$

Both $[\text{hmim}]^+$ and $[\text{tba}]^+$ are comparable in size with $[\text{bmpy}]^+$, so in conjuction with $[\text{fap}]^-$ a similar ordering behavior as observed for $[\text{bmpy}]^+[\text{fap}]^-$ is to be expected from the geometric point of view. The reflectivities from their interface to sapphire, recorded for

---

[4] effectively achieved by fixing one ion's starting width to the value of the other
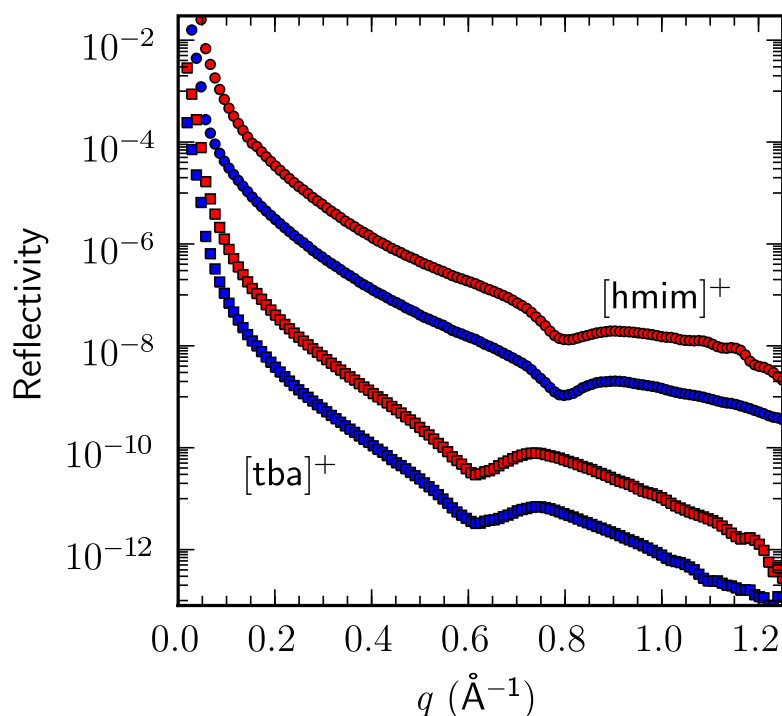
Figure 7.10: Corrected reflectivity curves of the $[\mathrm{hmim}]^+[\mathrm{fap}]^-$-sapphire (circles) and the $[\mathrm{tba}]^+[\mathrm{fap}]^-$-sapphire interface (squares) versus vertical momentum transfer q. The $[\mathrm{hmim}]^+$data was recorded at 110°C (red) and -30°C (blue), the $[\mathrm{tba}]^+$data at 120°C (red) and 56°C (blue). The curves are shifted by one order of magnitude against each other for clarity with an additional order of magnitude between the $[\mathrm{hmim}]^+$and $[\mathrm{tba}]^+$data.

each of the two liquids at 120 °C and close to its melting point, exhibit indeed pronounced layering features as is shown in Fig. 7.10. In case of $[\mathrm{hmim}]^+$, the feature resembles a dip at around $0.8\,\text{Å}^{-1}$, similar in shape and position to the one observed for $[\mathrm{bmpy}]^+$ at 120 °C. This similarity mirrors the common basic structure of the two cations comprising a ring and one longer side chain. In contrast, the characteristic feature in the reflectivity of $[\mathrm{tba}]^+[\mathrm{fap}]^-$ is strongly shifted towards lower q values and resembles rather a transition between a dip and a peak. The appearance at lower q values already indicates a larger periodicity than for the other two cations, which can be assigned to the bulkier cation, impeding an interdigitation of the side chains.

Strikingly, neither $[\mathrm{hmim}]^+$ nor $[\mathrm{tba}]^+$ display a significant temperature response in their reflectivity data. Apparently, here the increase in entropy induced by the temperature change is not sufficient to trigger a substantial change in interfacial order as in the case for $[\mathrm{bmpy}]^+$. The shared ring-tail geometry of $[\mathrm{bmpy}]^+$ and $[\mathrm{hmim}]^+$ makes it suggestive to account the differing conformational behavior of pyrrolidinium and imidazolium cations for their distinct temperature responses (compare Sec. 3.2): The flipping of the
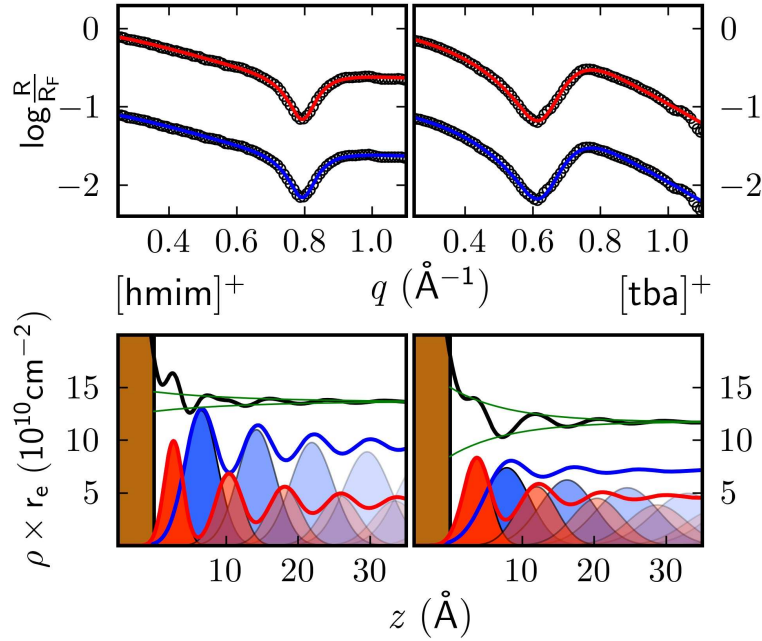
Figure 7.11: Upper panels: best fits to the $[\text{hmim}]^+[\text{fap}]^-$-sapphire (left) and to the $[\text{tba}]^+[\text{fap}]^-$-sapphire interface (right) at low and high temperature. Lower panels: Extracted density profiles for $[\text{hmim}]^+$(left) and $[\text{tba}]^+$(right) at the lower of the two recorded temperatures. Compare Fig. 6.5 for the assignment of the objects in the density profiles.

hydrocarbon tail in and out of the ring plane characteristic for the two main $[\text{bmpy}]^+$ conformers can be expected to drive a structural change stronger than the rotational conformers of $[\text{hmim}]^+$. This heuristic argument is supported by the fact that the induced energy difference per mole, $k_B \Delta T N_A$, is about $1\,kJ\,mol^{-1}$ between lowest and highest temperature and thus of the same order of magnitude as the calculated energetic difference of the $[\text{bmpy}]^+$ conformers.

7.2.1   Real space profiles

All distorted crystal model flavors discussed for the $[\text{bmpy}]^+$ data were also tested against the $[\text{hmim}]^+$ and $[\text{tba}]^+$ data with the best fits always to be obtained for the "cation first" ionic layering. Since all three ionic liquids share the same anion and given the strong evidence in favor of this model from the preceeding in-depth analysis (Sec. 7.1.1) as well as from independent measurements of the contact potential (Sec. 9.2), the other models will not be considered here. An unambiguous exclusion of one or the other model would hardly be possible from the $[\text{hmim}]^+$ and $[\text{tba}]^+$ data anyway due to the smaller data base (two instead of four temperature points) and the insignificant response to temperature changes.
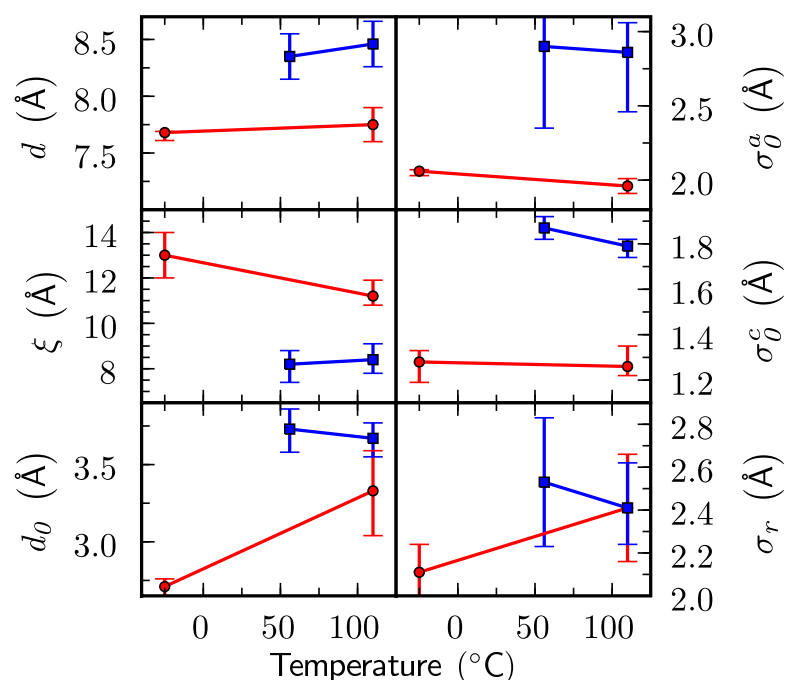
Figure 7.12: Evolution of all model parameters from the $[\text{hmim}]^+[\text{fap}]^-$-sapphire (red) and $[\text{tba}]^+[\text{fap}]^-$-sapphire interface (blue) versus temperature. The error bars represent a confidence interval of 30% around the cost function's minimum, obtained from parameter space maps with respect to the individual parameters (see Sec. 7.1.1).

Fit runs were performed in the same q-space range as for the $[\text{bmpy}]^+[\text{fap}]^-$ data. The upper panels of Fig. 7.11 show the excellent agreement of the resulting reflectivities with the experimental data, the resulting profiles for the lower temperatures are displayed in the lower panels. The extracted model parameters versus temperature are plotted in Fig. 7.12. For $[\text{hmim}]^+$, they are very consistent with the results for $[\text{bmpy}]^+$. d, d_0, $\sigma_0^{c,a}$, and ξ all are within the range defined by the lowest and highest temperature paramter sets of $[\text{bmpy}]^+[\text{fap}]^-$. Practically identical values for $\sigma_0^{c,a}$ give evidence of the close structural relation between both ionic liquids. The double layer spacing, d, again increases in agreement with thermal expansion, and the decay length, ξ, decreases, if only marginally, with temperature. As expected from the reflectivity data, its decrease from approx. $1.7\,d$ at $-30\,^\circ\text{C}$ to approx. $1.5\,d$ at $110\,^\circ\text{C}$ is much less substantial than for $[\text{bmpy}]^+$. Even an unchanging ξ is in agreement with the error margins. Contrasting to the parameter evolution of $[\text{bmpy}]^+[\text{fap}]^-$, the first layer offset, d_0, increases substantially by about 20%. This might also be assigned to the distinct conformational behavior of the two cations. On the other hand, the inherent correlation between d_0 and the interfacial roughness, σ_r, renders an unambiguous assignment impossible. Compared to the average interfacial roughness from fits to all data of about $2.5\,\text{Å}$, the $[\text{hmim}]^+[\text{fap}]^-$ value at $-30\,^\circ\text{C}$, $2.1\,\text{Å}$, is rather
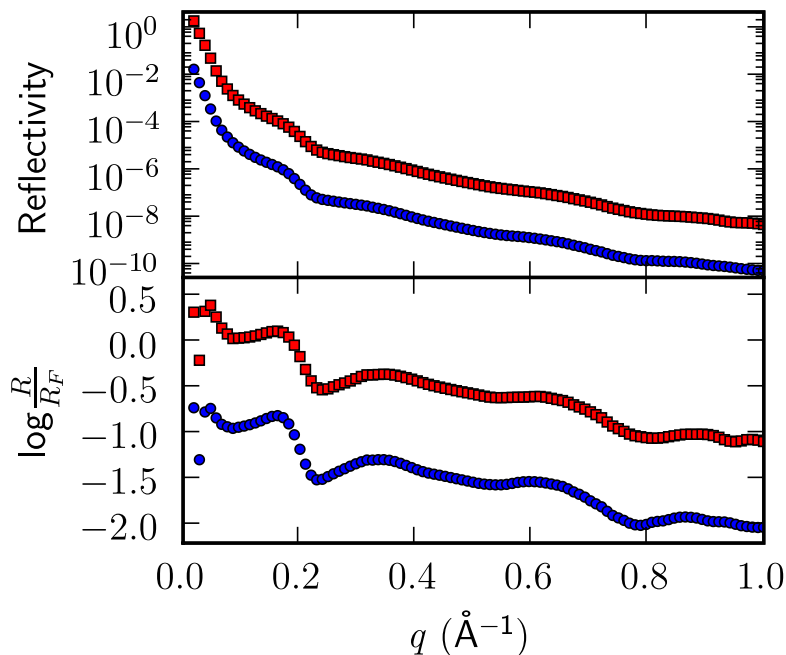
Figure 7.13: Upper panel: Corrected reflectivity curves of the $[\mathrm{c_{18}mim}]^+[\mathrm{fap}]^-$-sapphire interface recorded at 70°C (blue circles, shifted by two orders of magnitude) and 110°C (red squares), respectively. The lower panel shows the same data normalized by the Fresnel reflectivity, R_F.

low, favoring a low value for d_0 in turn. Hence, the observed increase might as well be a correlation artifact, and more data sets would be required to elucidate its origin.

In case of $[\mathrm{tba}]^+[\mathrm{fap}]^-$, the cation structure is fundamentally distinct from the former two's ring-tail buildup. Fitting the data at $56\,^\circ\mathrm{C}$ and at $110\,^\circ\mathrm{C}$ results in two almost identical sets of parameters. Not even d shows a significant response to thermal expansion. The temperature difference between the two curves is, however, only about one third of the range spanned by the two $[\mathrm{hmim}]^+$ data sets. According to thermal expansion, an increase of approx. $0.1\,\mathrm{\mathring{A}}$ in d would be expected – an increase well within the error margins. As suggested by the position of the layering feature, d is considerably higher than for $[\mathrm{bmpy}]^+[\mathrm{fap}]^-$ and $[\mathrm{hmim}]^+[\mathrm{fap}]^-$. Also the cation starting width, σ_0^c, is increased by about one third, reflecting that $[\mathrm{tba}]^+$ is the bulkier cation. The simultaneous increase in the anion starting width, σ_0^a, indicates that $[\mathrm{tba}]^+$ impedes as strong a packing of the ions as observed at the other two ionic liquids' interfaces.

7.3   Cation variation 2: $[\mathrm{c_{18}mim}]^+$

The fourth and last cation that has been investigated in conjunction with $[\mathrm{fap}]^-$ has to be treated differently, as becomes apparent from its peculiar structure (Fig. 3.3). For the

other three cations it might be justified to model their density distributions as Gaussian distributions, for $[\text{c}_{18}\text{mim}]^+$ with its four times longer side chain it certainly is not. Not surprisingly, the reflectivity data displays features uncommon to those observed before (Fig. 7.13): Instead of one pronounced feature, the Fresnel-normalized curve (lower panel) reveals a strong peak already at approx. $0.18\,\text{Å}^{-1}$, followed by a long-stretched plateau peaking at its shoulders at approx. $0.35\,\text{Å}^{-1}$ and $0.65\,\text{Å}^{-1}$. The first peak can be assigned to a periodicity of around $2\pi/0.18\,\text{Å} \approx 35\,\text{Å}$, suggesting that the octadecyl side chain is stretched perpendicular to the interface. Changing the temperature from $70°\text{C}$ (blue circles) to $120°\text{C}$ (red squares) has no significant effect on the data.

7.3.1   Real space profiles

As expected, the distorted crystal model in its original form as applied above was unable to reproduce the reflectivity data, resulting in very poor fits and unphysical parameter sets. Hence, either the model needs to be modified or a new parametrization of the interfacial density profile is required. Several fitting strategies were tested against the data: A multilayer approach using 1 to 5 layers of freely adjustable density followed by bulk liquid yielded acceptable fits even though the strong layering peak at low-q value could not be matched satisfactorily. On the other hand, the resulting profiles exhibited an unphysically large depletion layer at the interface of $10\,\text{Å}$ and more – independent of the number of layers. In a second approach, the binary distorted crystal model was adjusted to a tertiary system, accounting for the cation's ring and tail as individual sub-layers. With the charge centers arranged close to each other (cation ring and anion; controlled by the symmetry parameter, ϵ; see Sec. 6.4.3), the density of the tail was positioned in between the charged layers (again with optional deviations from symmetry). The width of the tail distribution was kept constant, increased according to the ionic distributions, or increased independently in different fit runs. However, none of the different variants could decently fit the data, despite the heavily increased number of free parameters.

More successful was another modification to the original model: Again ring and tail were separated from each other, but now taking the tail's contribution to the overall density as a constant offset, on top of which cation ring and anion were employed to build up the common ionic layering. The symmetry parameter was set free to allow the charges to arrange close to each other. Although this model is similar to the tertiary model introduced above, it requires no additional parameters in comparision to the standard model[5]. The construction of this model raises the question which part of the cation to assign as charge-carrying ring and which as neutral tail. From simulations of the electronic structure of imidazolium-based ionic liquids [151], it is known that the alkyl chain carbon atoms directly bonded to the ring carry significant charge, while the rest of the side chain is neutral. So the obvious separation is to consider the imidazolium ring, the methyl group, and the first link of the octadecyl group as charged "ring part" and the rest as "tail part".

---

[5] aside from the free symmetry parameter, which was fixed in case of the other three cations since its variation did not improve the fit quality there
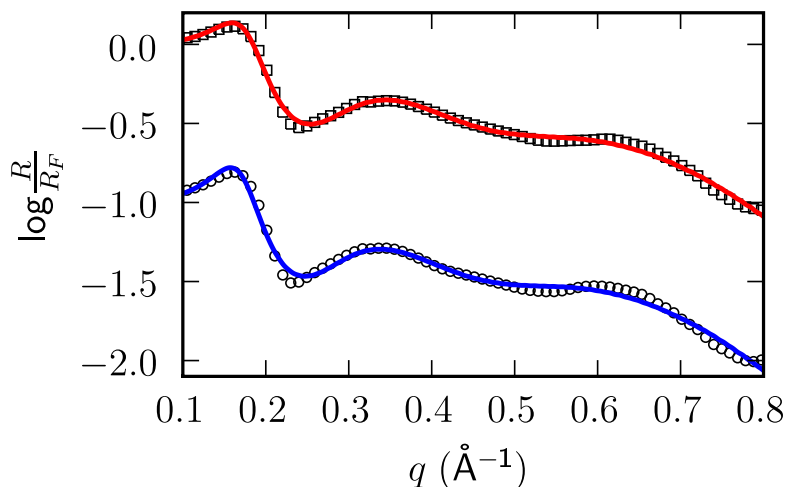
Figure 7.14: Best fits to the reflectivity data from the $[c_{18}mim]^{+}[fap]^{-}$-sapphire interface at 70°C (blue) and 110°C (red) using the "ring-tail" model extension (see text for details).

Other separations were also tested though, for instance taking the imidazolium ring as core charged part and allowing for a continuous variation of the ring:tail ratio by introduction of an additional fit parameter. The best fits were, however, obtained for the "ring plus first C" separation, albeit with no fundamental difference in the outcome. The fits were run in a q range from $0.09\,\text{Å}^{-1}$ to $0.8\,\text{Å}^{-1}$, hence including all noticable reflectivity features particular to this interface. Extending this range towards larger q values unavoidably worsened the fit quality and stability. Figure 7.14 shows the resulting fits normalized by R_F together with the corresponding data. The agreement within the fitted range is excellent; all features are reproduced, and the fits' curvature fairly matches the slope of the data. At $q > 0.8\,\text{Å}^{-1}$, the calculated reflectity does not follow the experimental data anymore but drops immediately instead (see also Fig. 7.18). This and the fact that the fit cannot adjust for an extended fitting range point out the incompleteness of the developed model. It does not account for short-range structural order on the intra-molecular level, e.g. arising from the strongly anisotropic environment experienced by the anion with long alkyl chains on one and the charged cation ring on its other side. On the other hand, it offers a generic arrangement of such an asymmetric ionic liquid at a hard wall that allows for a consistent interpretation of the main features in the reflectivity data.

A summary of the resulting model parameters is given in Tab. 7.1. The double layer spacing, d, of about $33\,\text{Å}$ corresponds to the value deduced from the position of the first peak, giving evidence that this most pronounced feature in the reflectivity data can indeed be assigned to the periodicity of the interfacial structure. The layering starts with the cation ring next to the interface, closely followed by the anion, as the asymmetry parameter, $\epsilon \approx 0.9$, infers. The laterally averaged distance of the centers of cation ring and anion, $(1-\epsilon)d \approx 4\,\text{Å}$, almost exactly matches the corresponding distances observed for $[bmpy]^{+}$ and $[hmim]^{+}$. This is remarkable, for it shows the similar strength and nature of the charge

Table 7.1: Summary of the fit parameters extracted from the $[c_{18}mim]^+[fap]^-$-sapphire interface.

	d (Å)	d_0 (Å)	ϵ	σ_c (Å)	σ_a (Å)	ξ/d	σ_r (Å)
70°C	34.4 ± 3.0	5.0 ± 1.2	0.88	2.8 ± 0.8	5.8 ± 2.1	0.84 ± 0.3	3.0 ± 0.4
110°C	32.9 ± 3.0	5.9 ± 1.6	0.88	2.7 ± 1.1	5.6 ± 1.4	0.82 ± 0.3	3.1 ± 0.6

coupling within these ionic liquids albeit their structural differences. In comparision, the starting values for the ionic Gaussian distributions, $\sigma_0^{c,a}$, are vastly increased, i.e. both cation ring and anion are strongly delocalized already at the interface. Apparently, the presence of the long cation tail inhibits the high degree of interfacial ordering observed for the other systems. The first layer offset, $d_0 \approx 5.7\,\text{Å}$, is higher than for the other systems, reflecting the wider spread of the first cation/anion layer. Then again its value might be biased by the simplified assumption of an isotropic offset layer, which does not consider deviations at the sapphire-liquid crossover. As expected from the practically identical reflectivity curves, the effect of temperature on the fit parameters is negligible within the probed range of $40\,\text{K}$. The overall picture of the $[c_{18}mim]^+[fap]^-$-sapphire interface emerging from this analysis is illustruted in Fig. 7.15 on the basis of the parameter set at $110°C$. Fitting an envelope function to the electron density profile yields a relative decay length, $\xi = 0.84\,d$, of the same order as for the other $[fap]^-$-based ionic liquids. Due to the large periodicity, the absolute range of the layering into the bulk liquid is, however, much higher: Even $100\,\text{Å}$ away from the interface, the deviations from bulk density are still significant. The periodicity itself is in good agreement with findings from Carmichael *et al.* who investigated the thin-film structure of two $[c_{18}mim]^+$-based ionic liquids [78] .

7.4   Liquid structure factors

Bulk liquid scattering data were recorded at each temperature point for all systems using the same setup[6]. Figure 7.16 presents an overview over these data and shows their evolution with temperature. Two issues constrain an interpretation of the characteristic features. The complex nature of $[fap]^-$-based ionic liquids makes a direct assignment of the observed correlation peaks to intermolecular real-space structures from these data alone impossible. Intramolecular structures remain completely unresolveable with the limited accessible q-space range, $q_{max} \approx 3\,\text{Å}^{-1}$, restricting the experimental resolution to distances $> 2\pi/q_{max} \approx 2\,\text{Å}$. Secondly, the scarce coverage of these novel $[fap]^-$-based ionic liquids in literature to date does not allow for an in-depth comparative analysis as conducted for ILs comprising widely studied ions such as $[BF_4]^-$, $[PF_6]^-$, or $[Tf_2N]^-$ [89]. There are, however, some characteristic features that can readily be related to the interfacial structures found in this work: The dominant correlation peaks in all four systems correspond to

---

[6] except for $[bmpy]^+[fap]^-$, where $100°C$ replaces $110°C$, and no LSF data were acquired at $66°C$
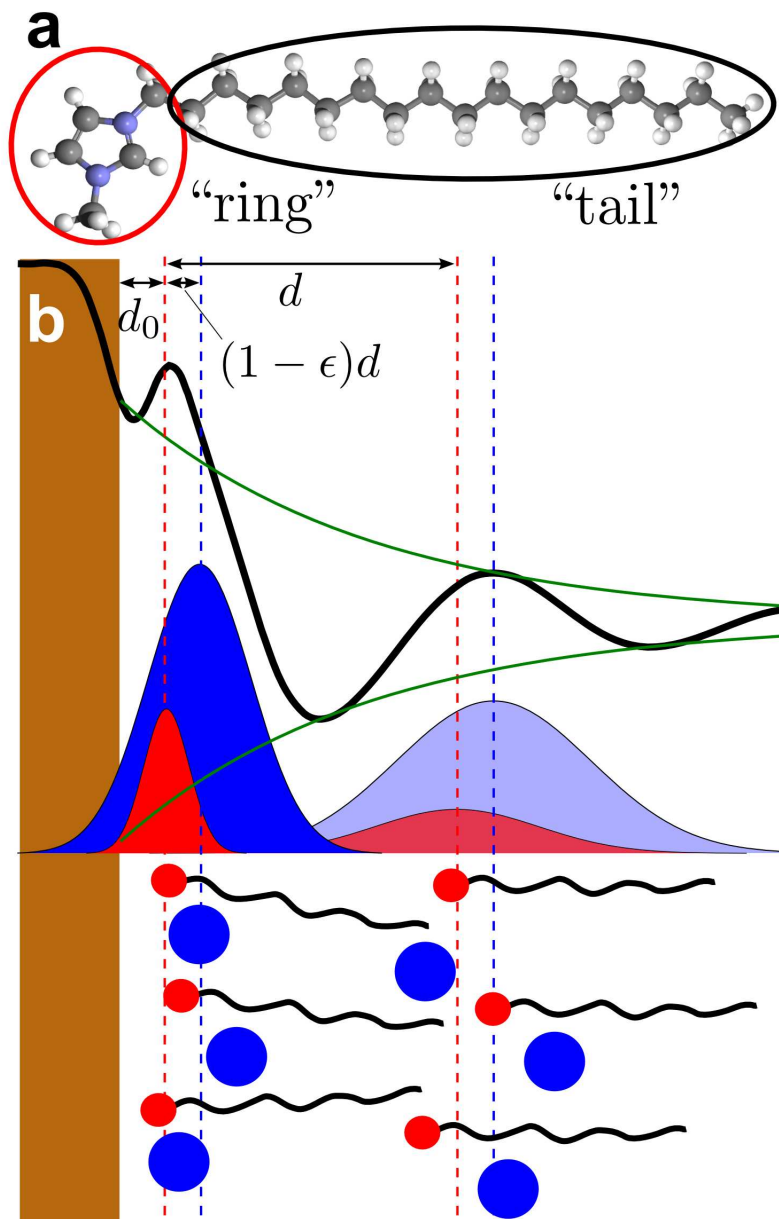
Figure 7.15:   Illustration of the density parametrization employed to fit the $[c_{18}mim]^{+}[fap]^{-}$-sapphire interface. a) Molecular structure of $[c_{18}mim]^{+}$ and its subdivision into a charged "ring" contribution (highlighted by the red circle) and a neutral "tail" contribution (black circle). b) Sketch of the extracted interfacial structure on the basis of the fit parameters at 110°C. Brown bar: sapphire substrate; red and blue lines: partial cation ring and anion density distributions; bold black line: total density profile; green lines: fitted exponential envelope functions to the profile. The vertical dashed lines represent the average positions of cations and anions in the first two adlayers. The first layer offset, d_0, the layer spacing, d, and the cation ring-anion distance, $(1-\epsilon)d$, are indicated. Below the profile, a possible molecular configuration is outlined to visualize the model parametrization.
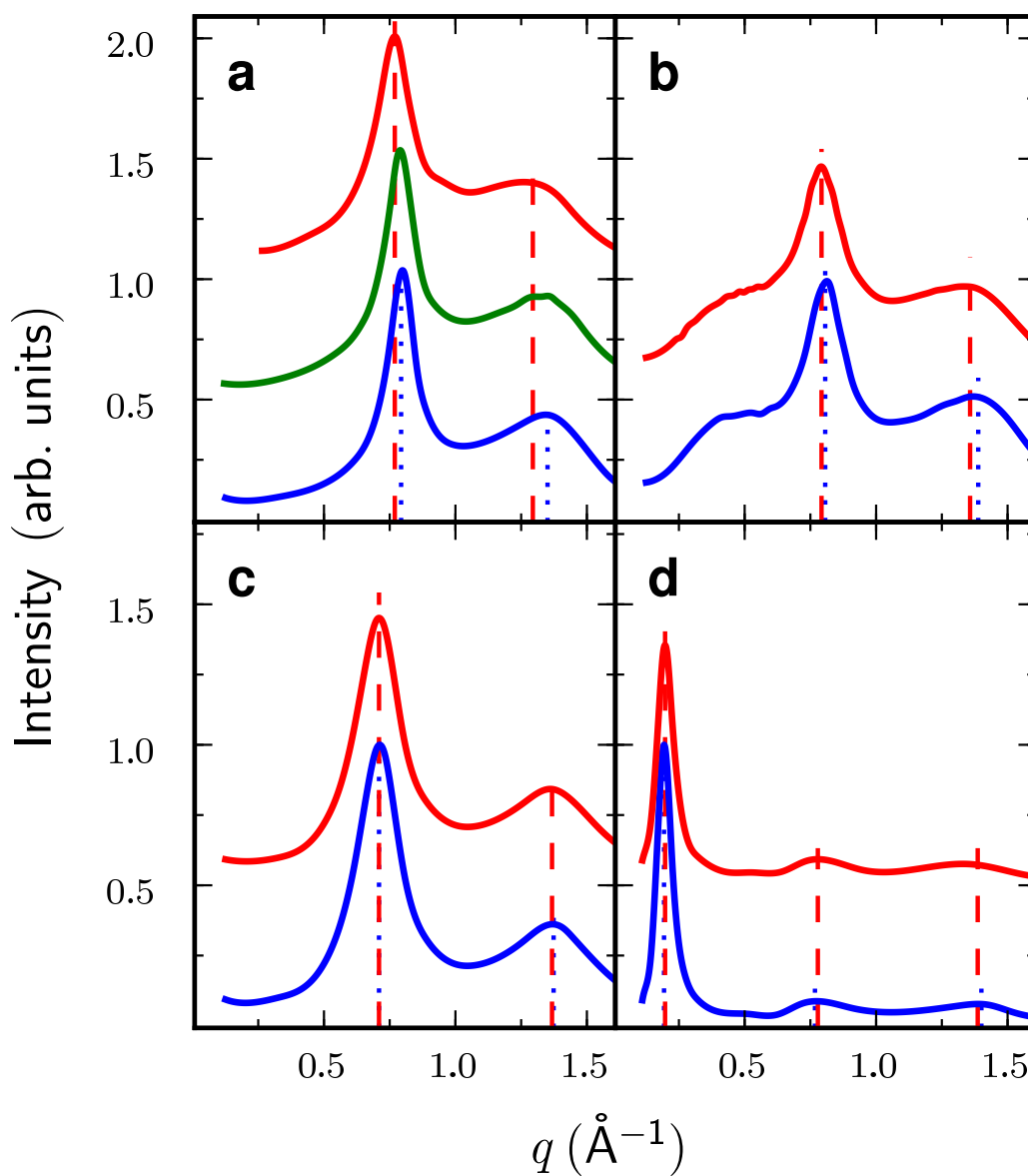
Figure 7.16: Bulk liquid scattering data of all four [fap]$^-$-based ionic liquids at different temperatures: a) [bmpy]$^+$[fap]$^-$at $-15°$C (blue), $8°$C (green), and $100°$C (red); b) [hmim]$^+$[fap]$^-$at $-15°$C (blue) and $110°$C (red); c) [tba]$^+$[fap]$^-$at $55°$C (blue) and $110°$C (red); d) [c$_{18}$mim]$^+$[fap]$^-$at $70°$C (blue) and $110°$C (red). The vertical lines indicate the positions of prominent correlation peaks at low (dotted blue) and at high temperature (dashed red). All curves are normalized to the amplitude of the highest correlation peak in the respective liquid at the lowest temperature and shifted by 0.5 against each other for clarity.

Table 7.2: Comparison of bulk correlations to interfacial structure.

	$[\text{bmpy}]^+$	$[\text{hmim}]^+$	$[\text{tba}]^+$	$[\text{c}_{18}\text{mim}]^+$
q_{bulk} (Å^{-1})	0.79	0.8	0.7	0.19
$2\pi/q_{bulk}$ (Å)	8.0	7.9	9.0	33.2
$\Delta FWHM_{bulk}$ (%)	28	5	2	7
$d_{interface}$ (Å)	7.7	7.7	8.4	34.4
$\Delta\xi$ (%)	-20	-13	-2	n/a

real-space distances that are in good agreement with the corresponding double layer spacings at the interface (compare Tab. 7.2). Molecular dynamics simulations and wide-angle x-ray studies of imidazolium- and pyrrolidinium-based ILs with similarly complex anions find analogous low-q peaks in the liquid structure and assign them to a superposition of anion-anion and cation-cation correlations [152–154], supporting the idea that the interfacial order is driven by intrinsic bulk liquid properties. With increasing temperature, these dominant peaks slightly broaden and shift towards lower q values, reflecting the thermal expansion and decreasing interfacial order due to the increase in entropy as to be expected. In conformance with the changes in the interfacial data, these changes are minor (within a few per cent) for $[\text{hmim}]^+$, $[\text{tba}]^+$ and $[\text{c}_{18}\text{mim}]^+$. For $[\text{bmpy}]^+$, however, the peak width increases by 40%, which is of the same order as the decrease of the decay length characterizing the interfacial ordering. A similar temperature behavior was observed in systems with a different anion; so it appears that the conformational freedom of the pyrrolidinium cation facilitates structural responses to temperature changes both in the bulk liquid as well as at interfaces (see Sec. 3.2 and the discussion of the temperature behavior in the next section).

All four ionic liquids exhibit a broad correlation peak at $q \approx 1.35\,\text{Å}^{-1}$, corresponding to a distance of about $4.7\,\text{Å}$. Despite the structural differences of the four cations, shape, position, and intensity of these peaks are almost identical (compare also Fig. 7.17). Hence, the underlying correlations are likely to arise from intramolecular correlations within the $[\text{fap}]^-$ molecule, such as the correlation between the outer atoms of the three ethyl side chains, and from the first solvation shell around the anion.

7.5 Overview: Cation variation

Figure 7.18 presents an overview over the reflectivity data of the four different $[\text{fap}]^-$-based ionic liquids, showing in each case the Fresnel-normalized curve at the lowest available temperature together with the best fit. The upper three systems comprise cations of similar size and could consistently be fitted with one and the same density parametrization model of the interfacial structure. Even the data of the fourth system, $[\text{c}_{18}\text{mim}]^+[\text{fap}]^-$, is in good agreement with a slight modification to the original model that accounts for
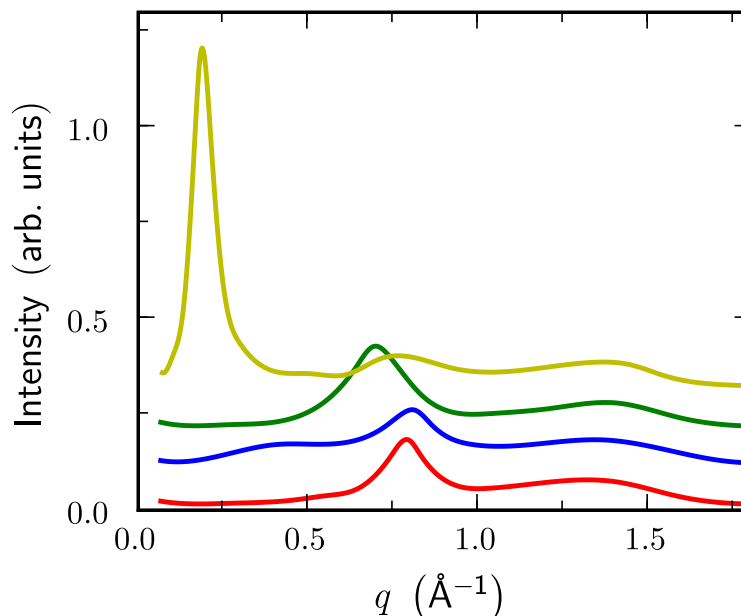
Figure 7.17: Comparison of bulk liquid scattering data from $[\mathrm{bmpy}]^+[\mathrm{fap}]^-$(red), $[\mathrm{hmim}]^+[\mathrm{fap}]^-$(blue), $[\mathrm{tba}]^+[\mathrm{fap}]^-$(green), $[\mathrm{c_{18}mim}]^+[\mathrm{fap}]^-$(yellow), each at the lowest available temperature. The curves are normalized to the first correlation peak of $[\mathrm{bmpy}]^+[\mathrm{fap}]^-$and shifted by 0.5 for clarity.

its cation's strongly differing shape. The extracted density profiles give evidence of pronounced ionic layering reaching several molecular distances into the liquid's bulk structure with decay lengths ranging between one and two double layer spacings. A qualitative comparison to bulk liquid scattering data suggests a close correlation between interfacial and bulk structure because the double layer spacings found in the former match the prevailing spatial correlations in the latter.

The noticable and systematic response to temperature changes of $[\mathrm{bmpy}]^+[\mathrm{fap}]^-$ provided an excellent test of different parametrizations against the data and allowed to rule out both an anion starting layer as well as a checkerboard-type of layering. Independent surface potential measurements (rf. Sec. 9.2) confirm that the formation of the positively charged adlayer is triggered by a radiation-induced negative charge at the sapphire surface. The following propagation of charge density oscillations several nm into the bulk is characteristic to all four $[\mathrm{fap}]^-$-based ionic liquids despite the structural differences of their cations. This confirms the importance of long-range Coulombic interactions for the configurational energy of the system as predicted by molecular dynamics simulations [155]. It also contradicts the classical mean-field theory (MFT) of the electrical double layer (EDL), which predicts the formation of a compact inner layer ("Helmholtz layer") and a diffuse outer layer ("Stern layer"). Although SFG and vibrational Stark effect data
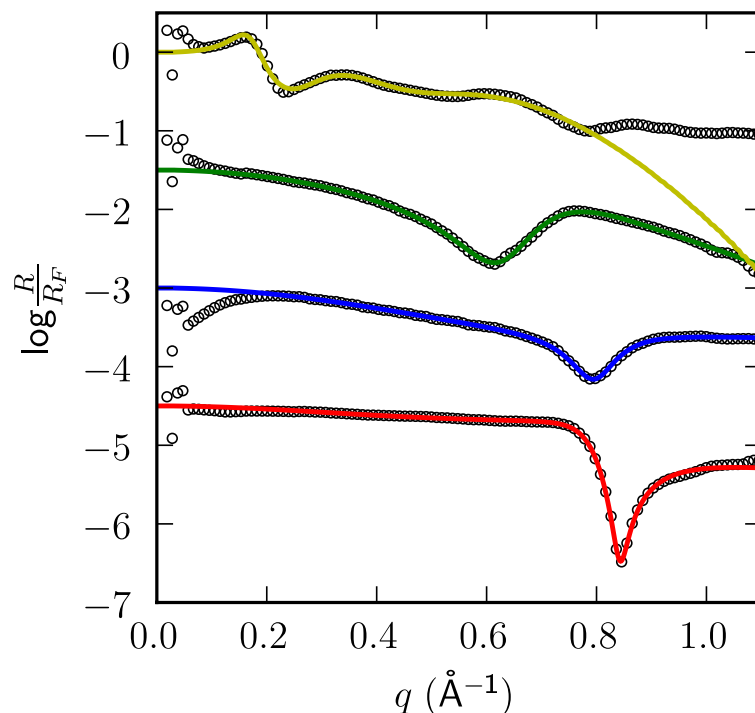
Figure 7.18: Corrected and Fresnel-normalized reflectivity curves of all four $[\text{fap}]^-$-based ionic liquids together with best fits: $[\text{bmpy}]^+[\text{fap}]^-$ at $-15°$C (red), $[\text{hmim}]^+[\text{fap}]^-$ at $-25°$C (green), $[\text{tba}]^+[\text{fap}]^-$ at $56°$C (yellow), and $[\text{c}_{18}\text{mim}]^+[\text{fap}]^-$ at $-25°$C (blue).

support the validity of the classical approach even for ionic liquids [156], our results underline the impact of short-range correlations and finite-volume effects neglected in MFT on the structure of such strongly correlated systems.

An extended MFT, accounting for these effects[157], and recent molecular dynamics simulations [158, 159] predict the observed exponentially damped oscillatory behavior and assign it to *overscreening* of the surface charge, i.e. the latter is overcompensated by the ions of the first adlayer; this in turn triggers a slightly less pronounced overcompensation in the subsequent counterionic layer, and so forth. With a lateral ion density of approx. one per 16 Å^2 in case of $[\text{bmpy}]^+[\text{fap}]^-$, the surface charge density, σ_S, should be below $\sigma_{max} \approx 100\,\mu\text{C/cm}^2$, which is a reasonable assumption. For $\sigma_S > \sigma_{max}$, the IL's dense-packing limit impedes full compensation, resulting in a less sharp, "bulkier" ionic adlayer. Called *lattice saturation*, this phenomenon might still lead to charge density oscillations, though somewhat less pronounced. The interpretation of additional data on doping effects, however, is strongly in favor of an overscreened system (Sec. 8.1.1).

The pyrrolidinium-based system was the only one with a significant temperature dependence. This is most likely to be assigned to the presence of two sterically quite different conformers of $[\text{bmpy}]^+$, whose energetic difference is of the same order as the differences

in entropy induced by the temperature variation. In consequence, the balance between both conformers might gradually be altered during the temperature runs and thus initiate the observed structual changes: The decay length, ξ, diminishes linearly with increasing temperature – a result readily assigned to a loss of interfacial order due to increasing entropy. The same trend was observed in molecular dynamics simulations of NaCl melts in the strong-coupling regime [160]. Nevertheless, it is contrary to the mean-field Debye-Hückel theory, which predicts the opposite temperature dependence, giving further evidence for the non-portability of Poisson-Boltzmann approaches for diluted solutions to purely ionic systems. The lack of comparable conformational changes in $[\text{hmim}]^+$ offers a heuristic explanation for the different temperature response of these structually similar cations (see Sec. 3.2). Both cations were also studied in combination with a different anion, $[\text{Tf}_2\text{N}]^-$ [89], revealing again a temperature effect solely for the pyrrolidinium-based system and hence backing this assumption.

Although information on the capacitance of the EDL for IL-metal interfaces cannot directly be related to the IL-insulator interface of this study, a rough estimate for the total capacitance, C_t, can be obtained by thinking of it as a serial connection of a "compact" contribution from the first adlayer, C_c, and a "diffuse" contribution from the decaying oscillations, C_d:

$$\frac{1}{C_t} = \frac{1}{C_c} + \frac{1}{C_d} \,. \tag{7.1}$$

Approximating the partial capacitances as parallel plate capacitors of distance d_0 and ξ, respectively, yields

$$C_{c,d} = \frac{\epsilon_0 \epsilon_r}{d}, \ d = \{d_0, \xi\} \,, \tag{7.2}$$

with ϵ_0 the vacuum permittivity and ϵ_r the relative permittivity of the ionic liquid. These equations correlate the model parameters ξ and d_0 with the EDL capacitance. For $[\text{bmpy}]^+$ $[\text{fap}]^-$ at the lowest temperature and a typical estimate for the relative permittivity, $\epsilon_r \approx 10$ [161], a value of about $5\,\mu F/cm^2$ is obtained for C_t, which increases by some 30% at the highest temperature. Despite the crudeness of the applied approximations, the result is of the same order as experimental values for other systems [61, 69, 156]. An increase in capacitance with temperature was recently found for a variety of different ionic liquids by cyclic voltammetry [61] and is also a known phenomenon for high-temperature molten salts [162]. Its origin remains subject to discussion, but a loss of ionic association has been suggested as driving mechanism in the strong-coupling regime [163], being in perfect agreement with the reasoning for the decreasing decay length made above. Viewed from this direction, the seemingly surprising result of a negative temperature dependence of d_0 for $[\text{bmpy}]^+[\text{fap}]^-$ fits well into the picture as it also contributes to the increase in C_t.

Chapter 8

The effect of doping on the $[\mathrm{bmpy}]^+[\mathrm{fap}]^-$-sapphire interface

The data on the effects of doping on the interfacial structure of $[\mathrm{bmpy}]^+[\mathrm{fap}]^-$ were all acquired at $8°\mathrm{C}$ in the same experimental session as the corresponding data set from the neat IL, which served as the reference system. Two considerations led to chosing this temperature: The lower the temperature, the stronger the layering tendency, making induced changes easier to detect; on the other hand, staying well above the freezing point of water was important to avoid icing of the chamber mount.

In the next section, the data from binary mixtures of $[\mathrm{bmpy}]^+[\mathrm{fap}]^-$ with propylene carbonate is presented and discussed in detail, including the introduction of a model extension necessary to account for the dopant. Thereafter, its applicability to the data of the second solvent, triethylene glycol, is tested, followed by a discussion of the data from salt doping. The chapter concludes with an overview over the impact of doping on the interfacial structure.

8.1 Propylene carbonate (PC)

Data sets were acquired for four different molecular PC:IL ratios: 1:5, 1:2, 2:1, and 5:1. Figure 8.1 juxtaposes bulk liquid scattering and reflectivity data together with the corresponding data from the neat ionic liquid. In the bulk structure, the amplitude of the first correlation peak diminishes linearly with increasing solvent concentration (see inset of Fig. 8.1). Noticeably, the peak position does not alter significantly at the same time, indicating that the underlying correlations between like ions (compare Sec. 7.4) become indeed weaker upon doping but without a change in the corresponding spatial distances. Hence, while the ions still try to arrange in the same network as in the neat liquid, their correlations are suppressed by the introduced dopant. The mere reduction of ionic liquid in the scattering path is much too small to solely account for the diminishing peak.

Contrasting the first one, the second correlation peak, assigned to intramolecular and intermolecular correlations of the anion, does not appear to change systematically upon
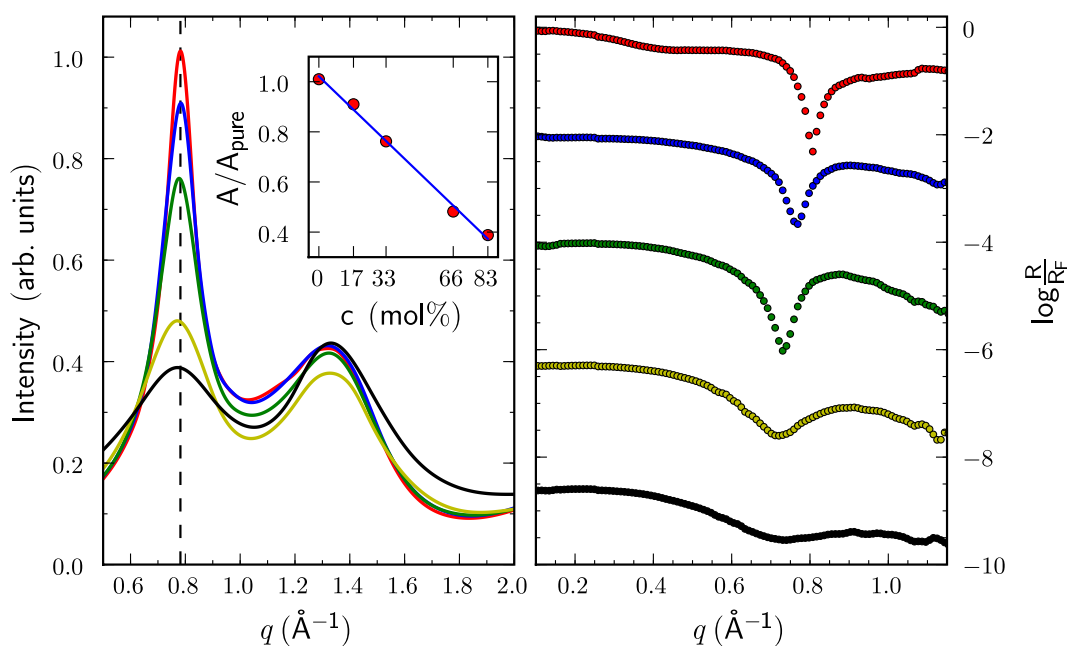
Figure 8.1: Bulk liquid scattering (left) and ionic liquid-sapphire reflectivity data (right) for binary PC:$[\text{bmpy}]^+[\text{fap}]^-$ mixtures, recorded at $8°\text{C}$. Red: pure ionic liquid; blue: 1:5 mixture (1 mole PC, 5 mole IL); green: 1:2; yellow: 2:1; black: 5:1. The vertical dashed line at $q = 0.78\,\text{Å}$ in the bulk scattering data marks the position of the first correlation peak in the pure liquid. In the inset, the amplitude of the first peak (red circles), normalized by the amplitude for the pure IL, is plotted versus the mole fraction of PC together with a linear regression (blue line). The reflectivity curves are shifted by two orders of magnitude against each other for clarity.

doping. These relatively weak mid-range correlations appear to remain unaffected by the dopant. The latter seems neither to have an influence on the conformation of the anion nor on the relatively weak mid-range correlations between anions and cations. This suggests that the dopant is most likely incorporated within charged planes, stretching them laterally and steadily disrupting the predominant centroid-centroid correlations with increasing concentration. On the other hand, the complex correlation network of the comprising three molecules cannot possibly be explained by the bulk data available alone. Therefore, the interpretations given above can only be regarded as plausible rather than conclusive.

Along with the linear loss of the predominant bulk correlation, the layering feature in the reflectivity data vanishes with increasing solvent concentration, accompanied by a shift towards lower q values. At the highest recorded concentration, 5:1, there is practically no structure left on the reflectivity curve, so the initially present interfacial order seems to be effectively removed.

8.1.1 Real space profiles

An extended density model

In order to quantify the evident screening effect of doping on the interfacial structure, the dopant needs to be included in the density parametrization developed for the neat ionic liquid. In the most simple approach the dopant is accounted for by means of a homogeneous offset layer with a partial density according to its volume fraction. At the same time, the area densities of the anion/cation Gaussian distributions are reduced correspondingly, yielding the following total electron density perpendicular to the interface:

$$\rho(z) = (2\pi)^{-1} \sum_{n=0}^{\infty} (1 - v_d) \left[\frac{\rho_c}{\sigma_n^c} e^{-\frac{1}{2}\left(\frac{d_0 + nd - z}{\sigma_n^c}\right)^2} \right.$$
$$\left. + \frac{\rho_a}{\sigma_n^a} e^{-\frac{1}{2}\left(\frac{d_0 + (n+\epsilon)d - z}{\sigma_n^a}\right)^2} \right] + (\rho_s - v_d\rho_d)\,\text{erf}\left(\frac{-z}{\sqrt{2}\sigma_s}\right) + v_d\rho_d\,. \qquad (8.1)$$

with v_d and ρ_d the volume fraction and the density of the solvent, respectively, and all other parameters as defined in Sec. 6.4.3. v_d is evaluated as

$$v_d = \frac{x_d M_d / \rho_d}{x_d M_d / rho_d + (1 - x) M_{IL} / \rho_{IL}}\,, \qquad (8.2)$$

assuming that the binary ionic liquid-solvent mixture comprises an ideal mixture[1]. x_d is the molar fraction of the dopant and $M_{d,IL}$ the molar weights of dopant and ionic liquid. This model describes the ionic liquid-sapphire interface for different dopant concentrations without any additional free fitting parameter at the cost of neglecting possible segregation or site-specific adsorption of the dopant molecules. Given the limited number of distinct features in the reflectivity data, further parametrization would hardly yield clear fitting results with physically meaningful parameters. Still, this approach seems reasonable since the dopant molecules are expected to screen the ionic charges from each other and should hence be laterally distributed in a homogeneous fashion. SFG measurements at the free surface of IL-benzene mixtures show that the presence of dopant molecules is always in agreement with its concentration in the mixture [166], which also suggests an isotropic distribution. Furthermore, the initial cation layer was shown to be surface charge-induced (rf. Sec. 9.2 and discussion in the next section), so it is likely that no solvent enrichment takes place at the interface and thus no inhomogeneity is to be expected. Figure 8.2 exemplifies the parametrization model with its individual constituents by means of the dataset obtained for the 1:2 mixture.

Parameter refinement

Employing the model extension introduced above, the four different PC:IL mixtures were fitted in the same q-space range as the neat ionic liquid, from $0.25\,\text{Å}^{-1}$ to $1.05\,\text{Å}^{-1}$. Fig-

---

[1] Experimental data and theoretical predictions for various binary mixtures of ionic liquids yield excess molar volumes of $V^E = V - V_{ideal}$ in a range between approx. $-1\frac{cm^3}{mol}$ and $0\frac{cm^3}{mol}$[164, 165]. Considering ideal molar volumes of several hundrets of cm^3 per mole, these deviations can indeed be neglected.
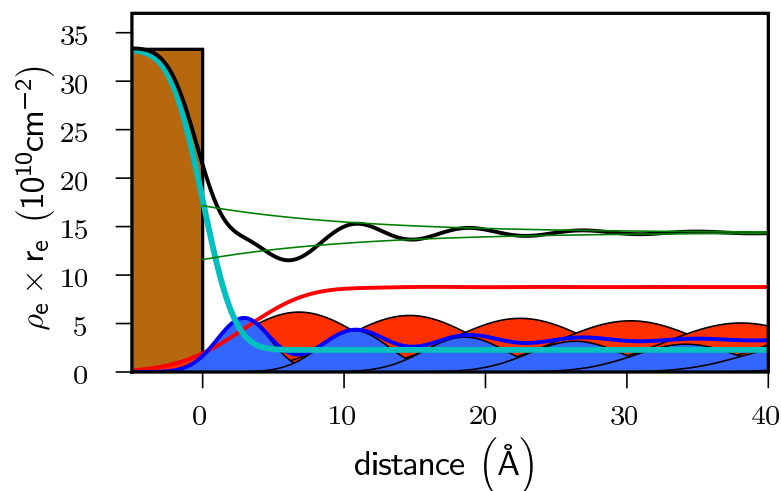
Figure 8.2: Extended model for the electron density profile across the interface including doping with molecular solvents. The dopant is taken into account as a constant offset layer (cyan full line) with a density representing its volume fraction. Cation (red) and anion (blue) densities are reduced accordingly. The total density profile (black) is the sum of the three partial densities. Brown bar: electron density of the sapphire substrate without roughness. The exponentially damped envelope function of the resulting total profile is shown in green.

ure 8.3 compares the resulting reflectivity curves to the data: The fits are in excellent agreement with the data for all mixtures and appear to reproduce the reflectivity features even better than the corresponding fit for the neat liquid does (red curve). Given the fact that no additional fitting parameters were required, this is quite astonishing.

The normalized and reduced density profiles are shown in Fig. 8.4 together with exponential fits to the envelope functions. The layering tendency decreases strongly with increasing dopant concentration as visualized by the vertical dotted lines representing a drop of the oscillations below one percent of the bulk densities. Figure 8.5 summarizes the evolution of all fitting parameters versus the mole fraction of PC. The decay length, ξ, decreases linearly with dopant concentration. At the highest concentration, $x_{mol} = 0.83$, ξ is reduced to a mere 30% of the neat IL's value. At the same time, there is a clear tendency towards smaller double layer spacings, d, with increasing PC concentration. The variation of the other parameters is rather inconclusive, partly conditional on the decreasing significance of the individual parameters for the fit quality. With less and less structure in the reflectivity data, this is not unexpected. d_0 and σ_c, however, are within the same range as for the neat liquid, whereas σ_a increases strongly although the large error bars indicate the fit's decreasing sensitivity to its variation. The roughness is systematically lower than for all neat liquid data sets but cannot be directly compared to the latter due to the integration of the solvent offset layer into the parametrization (compare Fig. 8.2).
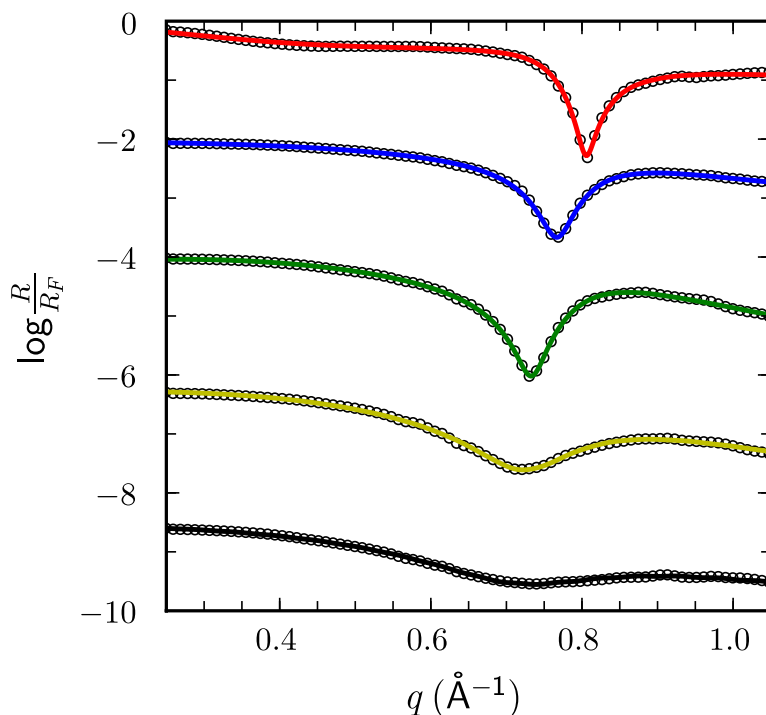
Figure 8.3: Corrected reflectivity curves from binary PC:$[\mathrm{bmpy}]^{+}[\mathrm{fap}]^{-}$ mixtures at the liquid-sapphire interface versus vertical momentum transfer together with the best fits, recorded at $8°\mathrm{C}$. Red: pure ionic liquid; blue: 1:5 mixture (1 mol PC, 5 mol IL); green: 1:2; yellow: 2:1; black: 5:1. The curves are shifted by two orders of magnitude against each other for clarity.

8.1.2   Discussion

The scenario for the impact of solvent doping on the interfacial structure emerging from the two systematic trends in the parameter evolution, linear decrease in ξ and negative trend of d, is outlined in Fig. 8.6: The solvent molecules increase the lateral distance between ions of like charge, screening them from each other. In order to compensate for the corresponding increase of the cation-anion distance in adjacent layers, oppositely charged layers move closer together, hence reducing the layering periodicity. The Coulomb attraction, however, diminishes gradually with increasing dilution of the ionic liquid by the dopant, which in turn implies a faster decay of the interfacial ordering.

It has been suggested that different structural regimes will be found as the concentration of a molecular solute is changed from dilute to dominant [164, 167–169]: Acting site-specific at first, aggregation on the domains of highest affinity should occur with increasing concentration, resulting in the formation of distictive local environments before becoming the dominant part of the mixture and eventually fully disrupting the ionic network. No indication for such a transition between different solvation regimes could be
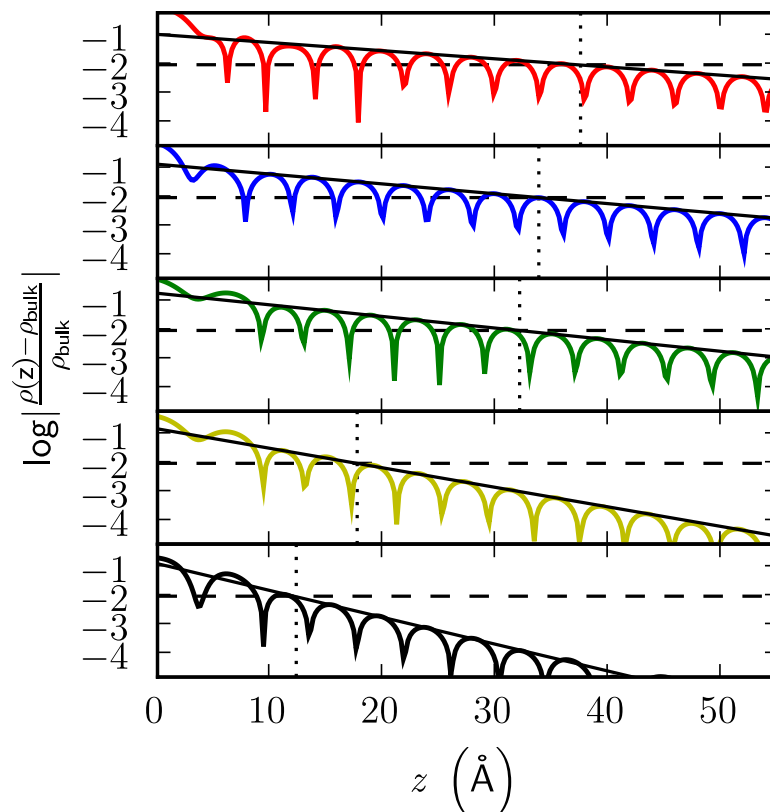
Figure 8.4: Extracted electron density profiles perpendicular to the IL-sapphire interface from binary PC:$[\text{bmpy}]^+[\text{fap}]^-$ mixtures. Red: pure ionic liquid; blue: 1:5 mixture (1 mol PC, 5 mol IL); green: 1:2; yellow: 2:1; black: 5:1. For the purpose of comparison, the absolute deviations from bulk density are shown on a logarithmic scale, and a threshold, set to 1% deviation from bulk density, is marked (dashed lines). The decay in layering strength is clearly visible in the increasing slope of the fitted exponential envelope functions to the profiles (solid black lines).

found here. Quite the contrary, the linearity of the decrease in decay length suggests a continuous process. Although an aggregation of PC outside the ionic network cannot be excluded from the data due to the lack of information on the lateral structure, the quite effective screening of the charges suggests otherwise.

Unlike the lateral ion-ion distance at the interface, the cation-cation distance in the bulk liquid does not expand upon doping. Apparently, the ions try to keep their prefered distance even at very high dopant concentrations. Whereas neutron diffraction studies on an IL-benzene mixture found an expansion of the ionic structure [82, 170, 171], similar non-expansive behavior was predicted in molecular dynamics simulations of binary IL-alcohol mixtures [172], where the alcohol molecules are accomodated within the ionic network without establishing network structures on their own. The correlation strength,
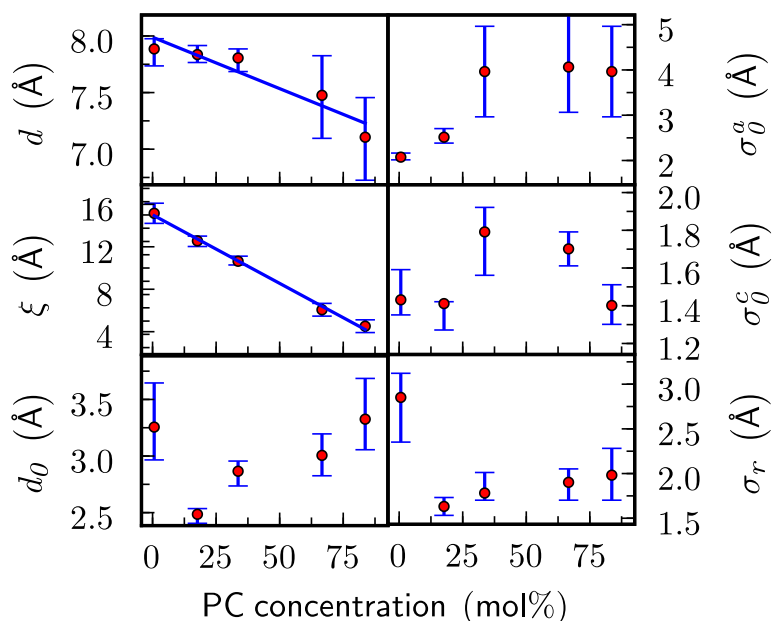
Figure 8.5: Evolution of all model parameters for PC:$[\text{bmpy}]^+[\text{fap}]^-$ mixtures versus mol fraction. The error bars represent a confidence interval of 30% around the cost function's minimum, obtained from parameter space maps with respect to the individual parameters (see Sec. 7.1.1). Double layer spacing, d, and decay length, ξ, are shown together with a linear regression (blue lines).
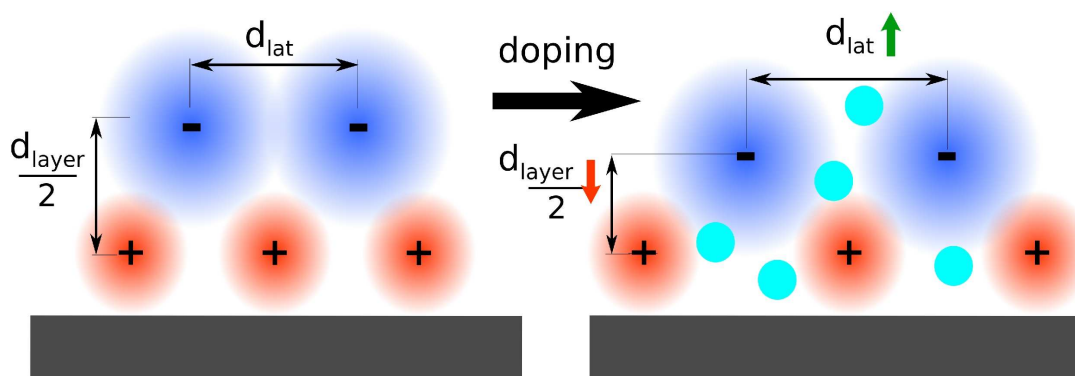
Figure 8.6: Schematic interpretation of the effect of doping with molecular solvents on the interfacial structure of $[\text{bmpy}]^+[\text{fap}]^-$. Aggregating mainly in charged slabs, the solvent molecules (turquios) increase the lateral distance between cations (red) and anions (blue). In order to compensate for the increased anion-cation distance, the spacing of the charged layers perpendicular to the interface is in turn reduced.

however, is weakened systematically with dopant concentration as the linear decrease in amplitude of the corresponding first correlation peak in the bulk liquid structure shows. Instead of expanding the network structures when screening like charges in the bulk liquid, a PC molecule annihilates the correlation between two cations or anions, respectively, highlighting the short-range H-bonding nature of these correlations (Sec. 7.4). Seggregation of PC molecules in separated domains can, again, not be excluded [167, 173]. The data provide no support for such an assumption, though.

The formation of an ionic-counterionic layering is assigned to a negative sapphire surface charge (rf. to Secs. 7.5 and 9.2). If its charge density were higher than the maximum lateral cation density, a constant dopant offset layer would effectively dilute the first cation adlayer and hence contradict electrostatics. Additional fit runs were performed allowing the fit to increase the cation density within the first adlayer at the cost of dopant concentration. The best fits, however, yielded no increase of the cation density for any PC:IL ratio. This suggests that the surface charge is highly overcompensated in the neat ionic liquid, triggering long-range charge density waves (*overscreening*, see Sec. 7.5). In consequence, the presence of the dopant, even in the very first layer, does not implicate an electrostatic penalty.

8.2 Triethylene glycol (TEG)

The binary mixtures of $[\text{bmpy}]^+[\text{fap}]^-$ with triethylene glycol provide a second model system to test the density parametrization introduced above. Figure 8.7 shows the bulk liquid scattering and reflectivity data from the two probed TEG:IL ratios, 1:5 and 1:2, together with the corresponding data from the neat ionic liquid. As for the PC mixtures, a strong decrease of the first correlation peak's amplitude with increasing dopant concentration is observed in the bulk liquid scattering, again without a significant change of its position in q space. The two different concentrations provide too small a dataset to decide whether this decline is linear or not, but the dopant's impact on the correlations appears to be stronger with increasing concentration: Whereas the peak amplitudes for the TEG/PC:IL 1:5 mixtures are comparable, the TEG 1:2 value has already diminished to the corresponding value of the PC 2:1 mixture (compare the insets of Figs. 8.1 and 8.7). The trend for the second correlation peak contrasts the observations made for the PC mixtures. Changing only very little at low concentration, it diminishes strongly at the higher concentration, accompanied by a significant shift towards larger q values. This might be assigned to a transition between different solvation regimes as discussed in the previous section. In accordance with the PC data, the layering feature in the reflectivity curves is strongly suppressed with increasing dopant concentration while experiencing a continuous shift towards lower q values.

The TEG reflectivity data were fitted with the same model developed for the PC mixtures, treating the dopant as a constant offset layer. Figure 8.8 compares the fitted reflectivities with the PC curves of corresponding concentrations. The fits reproduce the data for both dopants almost perfectly. In addition, the comparison of TEG and PC reflectiv-
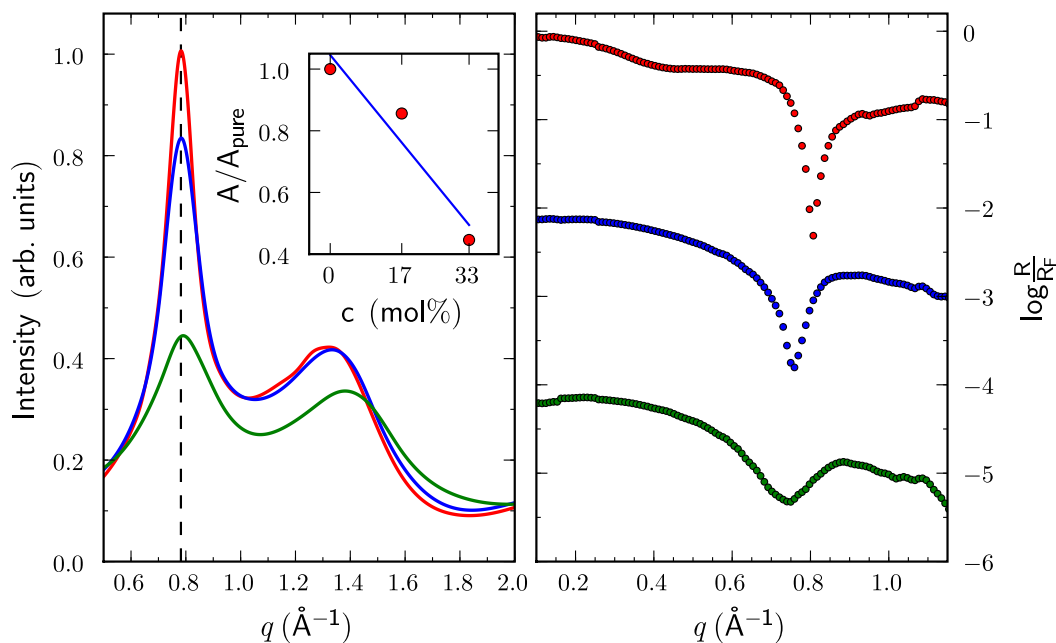
Figure 8.7: Bulk liquid scattering (left) and ionic liquid-sapphire reflectivity data (right) for binary TEG:$[\text{bmpy}]^+$mixtures, recorded at $8°$C. Red: pure ionic liquid; blue: 1:5 mixture (1 mol TEG, 5 mol IL); green: 1:2. The vertical dashed line at $q = 0.78\,\text{Å}$ in the bulk scattering data marks the position of the first correlation peak in the pure liquid. In the inset, the amplitudes of these first peaks (red circles), normalized by the amplitude for the pure IL, are plotted versus the mol fraction of TEG together with a linear regression (blue line). The reflectivity curves are shifted by two orders of magnitude against each other for clarity.

ity data shows the same trend already observed in the bulk data: At a ratio of 1:5, the differences between the layering features regarding position and shape are minor, but at 1:2, the impact of TEG on the reflectivity is much more pronounced than that of PC. The evolution of the two model parameters ξ and d, with dopant concentration quantifies this (Fig. 8.9). Both parameters exhibit a much steeper negative slope for TEG doping than for PC doping, evidencing a more efficient screening behavior of the TEG molecule. Before elaborating on the origin of this difference, Tab. 8.1 gives the evolution of all fitting parameters with TEG concentration for the sake of completeness.

The developed density model is capable of consistently explaining the interfacial data of the binary mixtures with both dopants. Substantial differences in their molecular structure suggest that the simplified model assumption of a constant dopant offset layer presents a viable approach to solvation in $[\text{bmpy}]^+[\text{fap}]^-$. Dopant aggregation within the ionic layers results in an increased lateral ion-ion distance, an increased layering periodicity, and a diminished charge ordering. Since the latter is thought to arise from long-range Coulomb
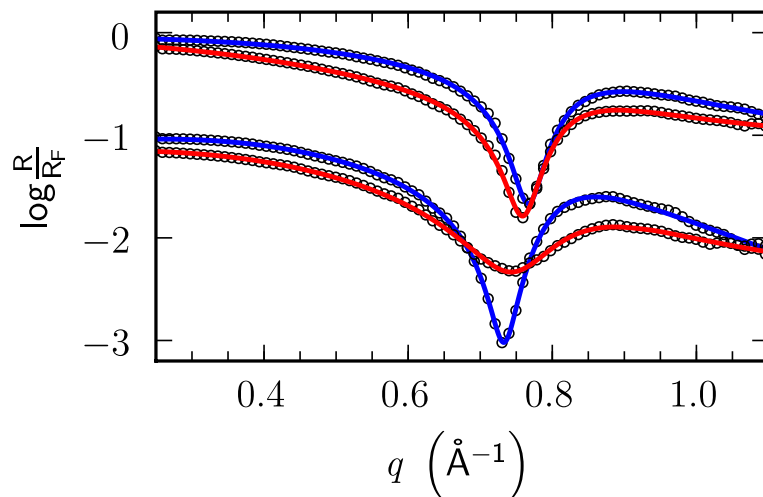
Figure 8.8: Comparison of corrected reflectivity curves from binary PC/TEG:$[\mathrm{bmpy}]^+[\mathrm{fap}]^-$mixtures at the liquid-sapphire interface versus vertical momentum transfer together with the best fits, recorded at $8°$C. The data for the two available TEG mixtures, 1:5 (top) and 1:2 (bottom) are shown, shifted by two orders of magnitude for clarity. Blue: PC:IL mixtures; red: TEG:IL mixtures.
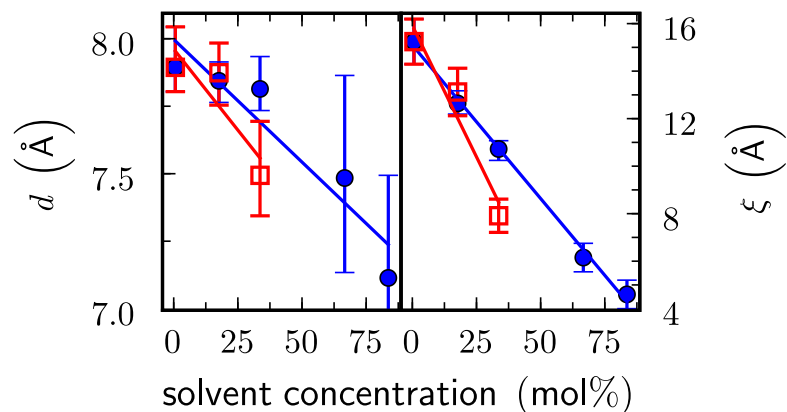
Figure 8.9: Evolution of the double layer spacing, d, and the decay length, ξ, with solvent concentration for PC:IL (blue) and TEG:IL (red) mixtures together with linear regressions (solid lines). The error bars represent a confidence interval of 30% around the cost function's minimum, obtained from parameter space maps with respect to the individual parameters (see Sec. 7.1.1).

Table 8.1: Summary of the fit parameters extracted from the liquid-sapphire interface of binary TEG:$[\text{bmpy}]^+[\text{fap}]^-$mixtures.

|	d (Å)	d_0 (Å)	σ_c (Å)	σ_a (Å)	ξ/d	σ_r (Å)
0	$7.9\pm^{0.1}_{0.2}$	$3.3\pm^{0.4}_{0.3}$	$1.4\pm^{0.2}_{0.1}$	2.1 ± 0.1	$1.9\pm^{0.2}_{0.1}$	$2.9\pm^{0.3}_{0.5}$
17	7.9 ± 0.1	2.5 ± 0.1	$1.4\pm^{0.1}_{0.2}$	2.4 ± 0.1	$1.7\pm^{0.1}_{0.2}$	2.0 ± 0.1
33	7.5 ± 0.2	$2.2\pm^{0.1}_{0.2}$	$1.8\pm^{0.1}_{0.2}$	3.4 ± 1.0	1.1 ± 0.2	$2.0\pm^{0.2}_{0.3}$

forces (rf. Sec. 7.5), the generic mechanism behind the observed doping response seems to be electrostatic Coulomb screening. On the other hand, the difference in screening power is striking. TEG appears to screen more efficiently despite its about three times lower dielectric constant (see Sec. 3.3). Though partly compensated by the higher molar mass of TEG, PC should possess the higher screening power were it only of electrostatic origin. Thus, TEG's higher screening tendency can be assigned to steric effects, i.e. the structure of the molecule and its preferential solvation into the ionic network drive the latter to break up faster than by doping with the PC molecule. Lacking detailed information on the structural arrangement on the molecular level, any reasoning can only be qualitative. It is suggestive, however, that the rod-shaped TEG molecule is more difficult to accommodate within the close-packed ionic network of $[\text{bmpy}]^+[\text{fap}]^-$ than the PC molecule is – in particular with its affinity for H-bonding in its ethylene parts disrupted by the highly polar oxygen sites, which are rather driven towards the charge centers.

8.3   Anion replacement with Cl⁻

The matching chloride salt of $[\text{bmpy}]^+[\text{fap}]^-$,$[\text{bmpy}]^+\text{Cl}^-$, is a hygroscopic, sticky powder at ambient conditions. Blending it with the IL resulted in a rapid increase in viscosity of the resulting mixture. The highest Cl^-:$[\text{fap}]^-$ ratio that could be prepared was 1:2; higher ratios led to solidification of the sample. Reflectivity curves were acquired for a total of five different ratios, 1:20, 1:10, 1:5, 1:3, and 1:2. Figure 8.10 shows the corresponding bulk liquid scattering and reflectivity curves. The bulk liquid scattering exhibits the same generic trend as observed for the doping with molecular solvents: The first correlation peak diminishes linearly with concentration while keeping its position in q space. The slope of this decline is within the range spanned by the two solvents, i.e. the screening impact of anion replacement is of the same order as solvent doping. The second correlation peak does not show a change.

Contrasting the systematic change in the bulk liquid, the reflectivity data displays an erratic behavior. Even though the familar trend towards broadened layering features at lower q values is perceptible, it is broken several times, making it practically impossible to develop a reasonable model parametrization and test its viability against the data. What might be the reason for these seemingly random changes in the datasets? The standardized
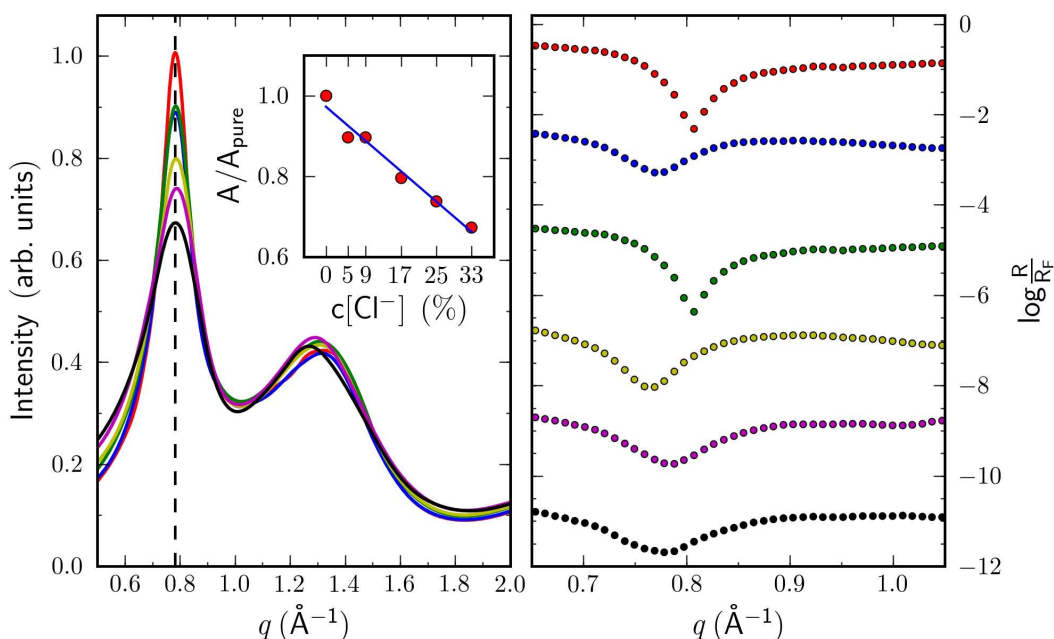
Figure 8.10: Bulk liquid scattering (left) and ionic liquid-sapphire reflectivity data (right) for binary $[\text{bmpy}]^+\text{Cl}^-$:$[\text{bmpy}]^+[\text{fap}]^-$ mixtures, recorded at $8°\text{C}$. Red: pure ionic liquid; blue: 1:20 mixture (1 mol $[\text{bmpy}]^+\text{Cl}^-$, 5 mol $[\text{bmpy}]^+[\text{fap}]^-$); green: 1:10; yellow: 1:5; magenta: 1:3; black: 1:2. The vertical dashed line at $q = 0.78\,\text{Å}$ in the bulk scattering data marks the position of the first correlation peak in the pure liquid. In the inset, the amplitude of the first peak (red circles), normalized by the amplitude for the pure IL, is plotted versus the relative concentration of Cl^- anions together with a linear regression (blue line). The reflectivity curves are shifted by two orders of magnitude against each other for clarity.

sample preparation and measurement protocol (rf. to Sec. 5.3) renders external contamination of several samples within a single dataset implausible. It is more likely that the mixture itself is unstable with a slow decomposition of one of the comprising molecules, which alters its interfacial properties. Depending on the time between preparation and measurement, the results might differ. For the present study, the time tracking during preparation was not accurate enough to elaborate on this possibility. In consequence, further studies, ideally with identical preparation-to-measurement times, are mandatory before any conclusions on the impact of anion replacement on the interfacial structure can be drawn. The trends in the reflectivity data and the evolution of the bulk liquid scattering, however, suggest that the higher mobility of the small atomic Cl^- results in less extended charge-ordering phenomena, generally supporting the idea that higher size asymmetry between the ionic species leads to more effective screening within an ionic liquid system [61, 159, 174].

8.4   Overview: Impact of doping

Two different approaches have been followed to study the impact of doping on the interfacial structure of $[\mathrm{bmpy}]^+[\mathrm{fap}]^-$: Doping with molecular solvents, namely propylene carbonate (PC) and triethylene glycol (TEG), and doping with the matching chloride salt, resulting in a partial substitution of $[\mathrm{fap}]^-$ with Cl^-. The binary mixtures with PC and TEG showed a systematic and consistent response to increasing dopant concentration. On the basis of these data, an extended version of the distorted crystal model was developed and successfully tested against the data. Although subject to the same generic trend, the anion replacement data exhibit an inconsistent evolution with Cl^- concentration, rendering a quantitative analysis impossible.

Despite their significant structural differences, both molecular solvents could be treated as a constant offset layer perpendicular to the interface. The model's two key parameters, decay length, ξ, and double layer spacing, d, decrease with increasing doping concentration. This suggests a preferential dopant aggregation withing the ionic layers, screening like charges; the ion association and, along with it, ξ diminish (compare Fig. 8.6). At the same time, the predominant correlations between like ions in the bulk liquid are systematically weakened but not spatially expanded. It seems that the dopant efficiently disrupts the ionic network without being accomodated within it. In the case of PC, these processes in bulk and at the interface develop linearly with dopant concentration and no transition between different solvation regimes is perceptible. TEG, on the other hand, appears to have an increasing impact with concentration although the database consisting of only two different concentrations is too small to deduce robust conclusions.

There is a remarkable difference in screening power between PC and TEG: Despite its three times lower dielectric constant, the TEG molecule screens more efficiently. Steric effects and site-specific interactions offer a plausible explanation for this deviation from electrostatic behavior. The rod-shaped TEG molecule with its alternating affinity for H-bonding (ethyle groups) and for ionic interactions (oxygen groups) along the chain might be more difficult to accommodate within the ionic liquid network, hence breaking it up faster. Further studies involving more solvents of different structure and composition and theoretical work on the solvation behavior of specific systems are necessary to obtain a better understanding of the screening mechanisms on a molecular level.

Figure 8.11 compares the bulk liquid scattering data of the neat IL with dopant:IL 1:2 mixtures for all three dopants, PC, TEG, and $[\mathrm{bmpy}]^+\mathrm{Cl}^-$, showing that both types of doping, mixtures with molecular solvents and anion replacement, are similar in their effect on the first correlation peak of the bulk liquid. These predominant correlations are strongly suppressed without being spatially expanded. They probably arise from short-range H-bonding, which completely lose their spatial correlation when disturbed by another molecule, independent of its nature. In their influence on the second correlation peak, the dopants differ widely. Whereas PC does not have a significant effect at any concentration, the peak strongly decreases upon doping with TEG, accompanied by a shift towards larger q values. The corresponding spatial distance decreases from $4.8\,\text{Å}$ to $4.5\,\text{Å}$. The complexity of the system inhibits a structural interpretation, but this peak change
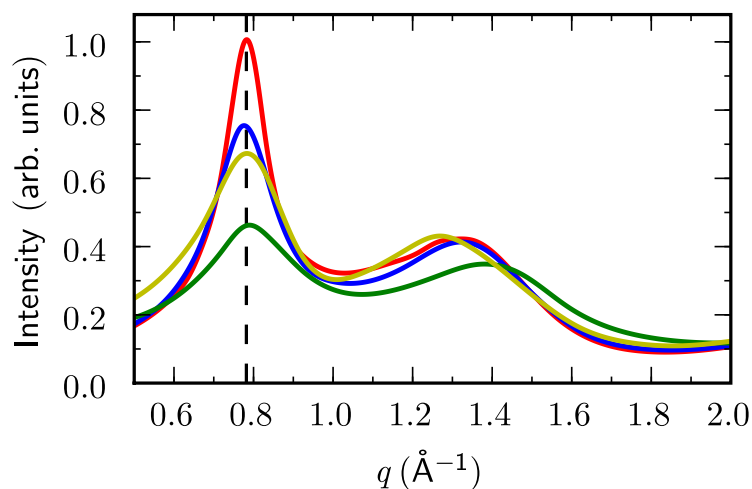
Figure 8.11: Comparison of the bulk liquid scattering data of the neat IL (red) with dopant:IL 1:2 mixtures for all three dopants, PC (blue), TEG (green), and $[\mathrm{bmpy}]^+\mathrm{Cl}^-$ (yellow). The vertical dashed line at $q = 0.78\,\text{Å}$ in the bulk scattering data marks the position of the first correlation peak in the pure liquid.

might be a tracer for a transition between distinct solvation regimes. In the case of anion replacement, the second correlation peak does not diminish but expand by 5%, suggesting a deformation of the underlying ionic network without disrupting it.

Chapter 9

Other results

9.1 External electric fields

The influence of external electric fields on the interfacial structure of ionic liquid-sapphire interfaces was investigated for $[\text{bmpy}]^{+}[\text{fap}]^{-}$ and for $[\text{hmim}]^{+}[\text{fap}]^{-}$. The measurements with the high voltage setup (see Sec. 5.4) suffered from two disadvantages: 1. The IL droplet did not completely cover the substrate along the beam path in order to hinder voltage break-throughs, rendering the data at small q values ($q < 0.2\,\text{Å}^{-1}$) irreproducible. 2. The small elevated platform, on which the substrate was placed, compromised the mechanical stability. In consequence, the alignment was lost several times after the application of an external voltage, U_{ext}. Intensity changes in timescans triggered by changes in U_{ext} could retrospectively be assigned to such instabilities rather than to changes in the reflectivity signal.

The maximum voltage that could be applied before an electrical break-through was approx. $\pm 5\,\text{kV}$. At these voltages, the IL droplet was visibly flattened and covered the whole area above the platform, hence minimizing the electrostatic energy of the system. Contrasting this, no reproducible response of the reflectivity data was observed. Figure 9.1 compares the reflectivity curves acquired over the same substrate area at the highest applied absolute voltages[1] in the order of acquisition (top first). Although the layering feature at approx. $0.8\,\text{Å}^{-1}$ shows a minor broadening, these changes are still well within the range typically observed in subsequent data sets and can be assigned to radiation damage (compare Sec. 6.1).

Since ionic liquids are electrically conducting, the effective electric field at the sapphire surface corresponds to the applied voltage divided by the substrate thickness, $d = 0.4\,\text{mm}$. This yields an applied maximum field strength of $|E| \approx 1.3 \times 10^{7}\,\text{V/m}$. Sample holder and ionic liquid form a parallel plate capacitor with sapphire as dielectric medium of capacitance, $C = \epsilon_0 \epsilon_r A/d$. Using the relation $Q = C \cdot U$, we can estimate the lateral charge

---

[1] no full data set was acquired at $+5\,\text{kV}$
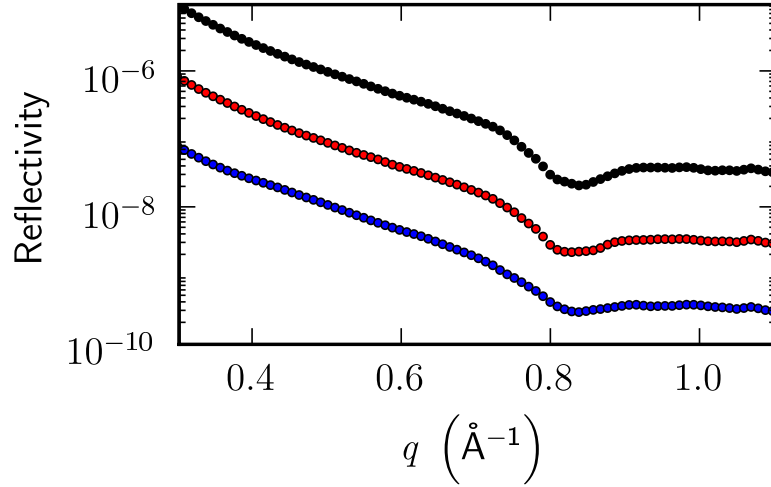
Figure 9.1: Comparison of reflectivity data of the $[\mathrm{hmim}]^+[\mathrm{fap}]^-$ interface with and without external electric fields, recorded at $T = 5°\mathrm{C}$. Black: no external voltage; red: $+3\,\mathrm{kV}$; blue: $-5\,\mathrm{kV}$.

density induced by the applied voltage:

$$\frac{Q}{A} = \frac{C \cdot U}{A} = \frac{\epsilon_0 \epsilon_r U}{d} \tag{9.1}$$

With the relative permittivity of sapphire, $\epsilon_r \approx 10$, this yields a lateral charge density of about 10^{-3} of the ion density in the first adlayer at the interface. So apparently these fields are not high enough to trigger significant changes in the interfacial structure.

The only electric field-induced interfacial changes reported to date were observed in contact angle measurements on a metal substrate coated with an insulating PTFE thin film [103] (see Sec. 3.4). Due to the thin insulating layer, only moderate voltages were necessary to achieve stronger electric fields. The field strengths, at which significant changes in contact angle were seen, were about one order of magnitude above the applied maximum fields in this work.

9.2 Kelvin probe measurements

Using the combined x-ray / Kelvin probe setup described in Sec. 5.5 in a pilot experiment, a series of measurements was carried out to probe charging effects of the x-ray beam: on (i) a bare substrate surface without x-ray illumination, (ii) a bare substrate surface with x-ray illumination, (iii) a substrate covered with IL and without x-ray illumination, and (iv) a substrate covered with ionic liquid under x-ray illumination. These measurements uncovered a strong effect of the x-ray beam on the insulating sapphire substrate. Exposing the bare substrate and the IL-covered substrate to the full microfocused x-ray beam resulted in

a potential drop of -550mV and -1300mV in the Kelvin probe, respectively. The sign and the magnitude of the potential drop at the bare substrate's surface and at the IL-substrate interface clearly demonstrated that the substrate surface gets noticeably charged by the x-ray beam exposure, suggesting that the observed layering at the IL-sapphire interface is triggered by a negatively charged sapphire surface.

Part IV

Conclusions

Chapter 10

Summary

This thesis reports a molecular-resolution x-ray reflectivity study of the interfacial structure of ionic liquids at a sapphire hard wall. Ionic liquids comprise organic ions and are liquid at room temperature. As a materials class, they possess unique physiochemical properties. The vast number of thinkable cation/anion combinations offers a handle to tailor these properties to match specific tasks and opens a wide range of technological applications for ionic liquids, for instance as electrolytes in high-performance fuel cells or as thermal fluids. Many of these applications involve processes at interfaces with solids. Therefore, a detailed understanding of the interfacial structure and its dependence on the constituent molecules is an important factor for improving existing applications and developing new ones. The present study contributes to this understanding by providing the highest-resolution structural information on such interfaces reported to date.

X-ray reflectivity is an ideal tool to gain access to deeply buried solid-liquid interfaces. Employing the High Energy Micro Diffraction setup (HEMD) at beamline ID15A at the European Synchrotron Radiation Facility (ESRF), the focus of this work was twofold: First, to resolve the structure of a new group of ionic liquids based on a specific anion, $[\text{fap}]^-$, at ultra-smooth sapphire substrates with molecular resolution in order to elucidate the nature and extent of the interfacial order. A layering model was proposed for a quantitative description of the electron density profile perpendicular to the interface and was found to be in excellent agreement with the data. Characteristic to all probed systems is a pronounced ionic layering that starts with a cation layer. Secondly, the response of the interfacial structure to the variation of different physical parameters was systematically investigated in order to obtain insights into the underlying ordering mechanisms. The interfacial order decreases linearly both with increasing temperature in neat ionic liquids as well as with increasing doping concentration in binary mixtures. The extent of the entropy effect, however, strongly depends on the cation type.

Complementary to the reflectivity data, bulk liquid scattering experiments were carried out that revealed a close correlation between bulk and interfacial structure. In addition, *in situ* surface-potential measurements suggest that the cation starting layer is triggered by negative surface charges on the sapphire surface.

Radiation-induced effects

The impact of radiation damage on the interfacial structure was thoroughly investigated. Subsequent data acquisition over the same sample area lead to a smearing of the layering features in the reflectivity data, which is an indication of radiation-induced random disruption of interference patterns. The changes in the reflectivity follow an exponential saturation function, with a time constant of the order of 10^2 s to 10^3 s, depending both on the ionic liquid and on the temperature. The radiation damage, however, is localized and does not spread to non-irradiated regions of the interface in time. An elaborate measurement protocol was set up in order to exclude any influence of radiation damage on the data.

Independent *in situ* Kelvin probe measurements of the sapphire surface with and without irradiation uncovered a strong effect of the x-ray beam on the insulating surface: Both for the bare substrate as well as for an IL-covered substrate, the surface potential dropped instantaneously when the interface was subjected to the full beam, indicating a radiation-induced negative surface charge.

The impact of cation type and temperature on the interfacial order

Four different cations, the imidazolium-based $[hmim]^+$ and $[c_{18}mim]^+$, the pyrrolidinium-based $[bmpy]^+$, and $[tba]^+$ (rf. to Sec. 3.2) were probed in conjuction with the $[fap]^-$ anion. Three of these, $[bmpy]^+$, $[hmim]^+$, and $[tba]^+$, are of similar dimensions, and the interfacial order of the derived ionic liquids could satisfacorily be explained with the binary distorted crystal model. It describes the laterally averaged cation and anion densities as Gaussian distributions of increasing widths for increasing distance from the interface, yielding exponentially damped charge-density oscillations perpendicular to the interface. Although other approaches were tested against the data, the nature of the interfacial layering could unambigeously be determined as fully symmetric ionic-counterionic layering starting with a cation layer, the positive starting layer triggered by the negative charge on the sapphire surface. The interfacial order decays on a length scale between one and two layering periodicities and extends several nm into the bulk of the liquid. Similar behavior of ionic liquids at charged walls has been observed in molecular dynamics simulations and predicted within the framework of an extended mean-field theory, accounting for short-range correlations and excluded-volume effects. Classical mean-field Poisson-Boltzmann approaches neglect such influences and fail to explain the observed phenomena.

The fourth cation, $[c_{18}mim]^+$, has a very distinct geometry in comparison to the other three. Its four times longer side chain splits it into a charged imidazolium group ("ring" part) and a neutral side chain ("tail" part), which makes it hardly possible to ascribe a single Gaussian density distribution to it. Consequently, the above model approach does not fit the data. An extended model, a trilayer model with asymmetric charges and a separating neutral "tail", reproduces the most prominent features of the reflectivity data. Although it neglects the intramolecular structure within $[c_{18}mim]^+$ cation, this model provides insights into the generic arrangement of highly anisotropic ionic liquids at solid interfaces. The

charge-countercharge distance perpendicular to the interface is in good agreement to the corresponding distances found for the other liquids. This shows the similar nature and strength of charge-coupling mechanisms in these liquids albeit their structural differences.

Only the $[\mathrm{bmpy}]^+$-based system exhibits a significant temperature effect: With increasing temperature, the decay length decreases linearly, by some 40% over a temperature range of $125\,\mathrm{K}$. The induced entropy change is of the same order as the energy difference between two structurally quite different pyrrolidinium conformers, suggesting that balance shifts between these conformers trigger the entropy-induced loss of interfacial order. Based on first-order assumptions for the electric double layer (EDL) capacitance, the observed temperature effect on the structure could be assigned to an increase of the EDL capacitance with temperature, which is consistent with cyclic voltametry studies. For the imidazolium cation of similar size, $[\mathrm{hmim}]^+$, however, no such temperature effect was observed, despite the similar structure of both cations. The lack of comparable conformational changes in $[\mathrm{hmim}]^+$ offers a heuristic explanation for this unequal response, highlighting the importance of steric effects on the interfacial order.

The bulk liquid scattering experiments reveal a very close correspondance of the interfacial layering periodicities to the predominant bulk correlations between like ions. Hence, the interfacial order appears to be driven by bulk liquid properties. In concordance with the temperature behavior at the interface, the only significant temperature response, apart from thermal expansion, was found for $[\mathrm{bmpy}]^+[\mathrm{fap}]^-$. The increase in width of the corresponding correlation peak with temperature is of the same order as the decrease in layering strength at the interface over the same temperature span.

Doping effects

Two different doping strategies were followed to study the impact of Coulomb screening on the interfacial ordering of ionic liquids: Doping with molecular organic solvents, propylene carbonate (PC) and triethylene glycol (TEG), and the fractional replacement of the $[\mathrm{fap}]^-$ anions with atomic counterparts. Both result reduced layering features in the reflectivity data even though only the solvent doping yielded consistent datasets that allowed to refine the layering model to account for the dopant. The best fits, in excellent agreement with the data, were obtained with a simple approach that includes the dopant as a constant dielectric background without the need for additional fitting parameters. The fact that a variable dopant concentration within the first adlayer does not improve the fit quality indicates that overscreening effects are the main trigger for the observed charge-density oscillations.

Ordering strength and layering periodicity decrease with increasing dopant concentration. This indicates a lateral aggregation of the dopant within the ionic layers, separating like charges from each other. The ion association and, thus, the interfacial ordering strength diminish. At the same time, the Coulomb attraction between the outstretched ions reduces the distance between adjacent ionic layers. Along with the interfacial order, the bulk correlations between like ions are reduced with increasing dopant concentration, but not spatially expanded. This is consistent with simulations predicting an accomodation of

the dopant molecules within the ionic network without establishing independent network structures. The linear relation between concentration and ordering strength provides no evidence for the presence of different solvation regimes.

Despite the structural differences, the refined model applied to both molecular dopants. This suggests that the observed screening phenomena represent generic mechanisms. The differences in screening power between PC and TEG, however, show the important role of steric and site-specific effects. The far stronger impact of TEG on the interfacial structure is likely to stem from its rod-like shape with alternating polar and non-polar sites.

Conclusion

High energy x-ray reflectivity allowed to study buried ionic liquid interfaces on the molecular scale with unprecedented resolution. Intrigueing features of the interfacial ordering of ionic liquids based on the $[\text{fap}]^-$ anion at a charged wall were unraveled, such as the formation of alternating ionic sub-layers with exponentially decaying order, protruding several nm into the bulk of the liquid. Being the first robust experimental proof of the existence of static charge-density oscillations at charged ionic liquid interfaces, the results of this work provide important input for a better theoretical understanding of the electric double layer in undiluted ionic systems.

Extent and nature of the observed layering were characteristic to all four probed liquids, despite structually quite different cation types. Therefore, this layering is expected to be a generic feature of complex ionic liquids at charged interfaces. Nevertheless, the differences in temperature response, that were assigned to distinct conformational behaviors, point out the importance of steric effects for the structural arrangement both in bulk and at interfaces. The same holds true for the screening potential of molecular solvents in binary mixtures, where steric influences offer a plausible explanation for the far higher screening power of triethylene glycol in comparison with propylene carbonate. Although the extracted laterally averaged structures do not give insights into site-specific interactions on the molecular scale they offer an experimental benchmark to test simulation data against. Hence, they might help developing new molecular force fields that could eventually allow to resolve the underlying screening mechanisms on a molecular level.

Altogether, it was shown that ionic liquids at charged interfaces show complex ordering phenomena and that systematic parameter variation offers the possibility to study the underlying physics on a molecular scale. The steadily increasing number of commercially available ionic liquids allows us to probe specific aspects of the interfacial ordering. In combination with molecular dynamics simulations on the same systems and new theoretical approaches, this will deepen our understanding of ionic liquids at interfaces and become a driving factor for application development. The outcome of this work is a step in this direction.

Chapter 11

Outlook

Open questions and interesting starting points for future research on ionic liquid interfaces are outlined in the following.

Influence of the substrate surface

In order to secure well-defined experimental conditions, all experiments in this study were carried out with identically prepared, highly hydrophilic sapphire surfaces. Further studies with differently terminated surfaces are required to elucidate the influence of the substrate surface on the interfacial ordering mechanism. The comparison between hydrophilic and hydrophobic substrates could help understanding the role of ion-substrate interactions; metallic substrates could be used to avoid a radiation-induced surface charge. The challenge is to find suitable alternative substrates of sufficient smoothness and chemical stability. Liquid mercury is a feasible metallic option that fulfills these requirements even though some technical issues need to be resolved first.

The influence of much higher external electric fields could be probed, if suitable thin insulating films on top of conducting substrates were at hand. Electric field-induced changes of the interfacial order, for instance a reversal of the charge in the first adlayer, might provide a handle to disentangle electrostatic Coulomb interactions from Van der Waals and H-bonding interactions. Unfortunately, thin films with rms roughnesses in the ångström region have not been reported to date. With improving technology and expertise, however, polymer thin films are being produced with increasing smoothness, so that these might become promising candidates in the future. In addition, such polymer films would have a lower electron density than at least some ionic liquids which opens the possibility to probe the lateral ion structure in the first adlayer with grazing incidence x-ray diffraction.

Database extension

A systematic extension of the ionic liquids database would improve our understanding of the relationship between molecular structure and interfacial properties. The impact of side chain lengths on the layering tendency could be studied in more detail, in particular for

the imidazolium backbone. This might give insights into the interplay of competing interactions: An Increasing cation size improves the Coulomb screening, hence weakening the ionic correlation network. On the other hand, longer side chains lead to stronger dispersive interactions between these chains and eventually to more pronounced correlations. Data points for very small side chains and for intermediate lengths between the already available data (6 and 18 carbons, respectively) might give insight into the interplay of the competing interactions and would allow to compare the interfacial behavior to chain length-dependent bulk properties.

It is also desireable to verify the observed conformational differences between imidazolium and pyrrolidinium on cations with exactly the same side chain configuration and to probe the effect of anion variation on at least one of the cations. The afore-mentioned role of ion-substrate interactions could potentially also be approached from the ionic liquid side. Functionalized ions with distinct absorption behavior, for instance an H-bonding and a non-H-bonding cation, could be compared in their impact on the layering tendency.

The commercial availability of adapted ionic liquids remains an impeding factor even though the number of procurable liquids increases steadily. Alternatively, a cooperation with either the vendor or with a laboratory with the expertise to synthesize the required high-purity ionic liquids on demand could be aspired.

Solvent doping should be studied in different binary mixtures, with both different ionic liquids as well as with different solvents, in order to test the proposed interfacial structure model. Preferentially, solvents with experimental or simulation data available should be covered. Since it is difficult to find solvents that are fully miscible and exhibit a low vapor pressure at the same time, the experimental conditions could be improved to allow for reproducable studies of volatile solvents, e.g. by decreasing the sample chamber volume or by establishing saturated atmospheres. Having this done, acetonitrile would be the first-choice candidate to probe due to its technological relevance and the wealth of reported studies. Inconsistencies in the acquired data for the other doping strategy, anion replacement, make it necessary to repeat the experiments under reproducable conditions as outlined in Sec. 8.3.

Kelvin probe measurements

The Kelvin probe measurements presented in this work were pilot studies but indicated already the enormous potential of the combined x-ray/Kelvin probe approach. A vacuum-tight setup would avoid noise from air scattering in the beam path and signal drifts stemming from water adsorption/desorption at the bottom side of the substrate and at the Kelvin needle. This would improve the reproducability and hence facilitate the quantitative analysis of the recorded signals. The absolute values of the potential changes at the bare and the IL-covered substrate could then be compared and interpreted for different ionic liquids. In case of binary mixtures, this might provide additional information on the interfacial adsorption and could help refining the proposed density parametrization.

Other methods

The ionic liquids employed in this study have only recently been synthesized and are thus scarsely covered in literature. For our understanding of interfacial processes, it would be enormously fruitful to tackle the same systems with different experimental approaches. Sum-frequency generation and direct-recoil spectroscopy, for instance, have provided insights on the orientational arrangement of different ionic liquids at hard walls. An obstacle for comparative studies is, however, the presence of a radiation-induced surface charge in the x-ray experiments. *In situ* approaches as developed for the Kelvin probe experiments, might be a promising option for future projects. For the same reason, molecular dynamics simulations on the same or at least similarly complex systems are highly desireable.

Bibliography

[1] M. Mezger, H. Schröder, H. Reichert, S. Schramm, J. Okasinski, S. Schöder, V. Honkimäki, M. Deutsch, B.M. Ocko, J. Ralston, M. Rohwerder, M. Stratmann, and H. Dosch. Molecular layering of fluorinated ionic liquids at a charged sapphire (0001) surface. *Science*, **322** 424–8, (2008). See p. 9

[2] H. Schröder, R. Roth, M. Mezger, H. Reichert, S. Schramm, J. Okasinski, S. Schöder, D. Pontoni, and H. Dosch. Solvent-induced screening of ionic liquids at a sapphire hard wall. *to be submitted*. See p. 9

[3] P. Walden. Molecular Weights and Electrical Conductivity of Several Fused Salts. *Bull. Acad. Sci. St. Petersburg*, pages 405–422, (1914). See p. 9, 16

[4] F. H. Hurley. Electrodeposition of Aluminum. US pat. 4,446,331, (1948). See p. 17

[5] R.A. Osteryoung J. Robinson. An Electrochemical and Spectroscopic Study of Some Aromatic Hydrocarbons in the Room Temperature Molten Salt System Aluminum Chloride-n-Butylpyridinium Chloride. *J. Am. Chem. Soc.*, **101** 323, (1979). See p. 17

[6] D. Appleby, C. L. Hussey, K. R. Seddon, and J. E. Turp. Room-temperature ionic liquids as solvents for electronic absorption spectroscopy of halide complexes. *Nature*, **323** 614–616, (1986). See p. 17

[7] F. Endres and S. Zein El Abedin. Air and water stable ionic liquids in physical chemistry. *Phys. Chem. Chem. Phys.*, **8** 2101–16, (2006). See p. 17, 19

[8] J. Wilkes and J. Zaworotko. Air and water stable 1-ethyl-3-methylimidazolium based ionic liquids. *J. Chem. Soc., Chem. Commun.*, pages 965–967, (1992). See p. 17

[9] A. V. Plakhotnyka, L. Ernst, and R. Schmutzler. Hydrolysis in the system LiPF-propylene carbonate-dimethyl carbonate-HO. *J. Fluorine Chem.*, **126** 27–31, (2005). See p. 17, 35

[10] H. Weingärtner. Understanding ionic liquids at the molecular level: facts, problems, and controversies. *Angew. Chem. Int. Ed.*, **47** 654–70, (2008). See p. 18, 19

[11] A. R. Katritzky, R. Jain, A. Lomaka, R. Petrukhin, U. Maran, and M. Karelson. Perspective on the Relationship between Melting Points and Chemical Structure. *Crystal Growth & Design*, **1** 261–265, (2001). See p. 18

[12] I. Krossing. Semi-Empirical Methods to Predict the Physical Properties of Ionic Liquids: An Overview of Recent Developments. *Z. Phys. Chem.*, **220** 1343, (2006). See p. 18

[13] P. Wasserscheid and W. Keim. Ionic Liquids – New "Solutions" for Transition Metal Catalysis. *Angew. Chem. Int. Ed.*, **39** 3772–3789, (2000). See p. 18

[14] M. Van Valkenburg, R. Vaughn, M. Williams, and J. Wilkes. Ionic Liquid Heat Transfer Fluids. *Paper presented at the Fifteenth Symposium on Thermophysical Properties*, (2003). See p. 18

[15] Merck KGaA. Data sheets. *http://www.ionicliquids-merck.de*, (2008). See p. 18, 38, 40

[16] U. Schröder, J. Wadhawan, R. Compton, F. Marken, P. Suarez, C. Consorti, R. de Souza, and J. Dupont. Water-induced accelerated ion diffusion: voltammetric studies in 1-methyl-3-[2,6-(S)-dimethylocten-2-yl]imidazolium tetrafluoroborate, 1-butyl-3-methylimidazolium tetrafluoroborate and hexafluorophosphate ionic liquids. *New J. Chem.*, **24** 1009–1015, (2000). See p. 18

[17] D. R. MacFarlane, P. Meakin, J. Sun, N. Amini, and M. Forsyth. Pyrrolidinium Imides: A New Family of Molten Salts and Conductive Plastic Crystal Phases. *J. Phys. Chem. B*, **103** 4164, (1999). See p. 18

[18] N. Ignat'ev, U. Welz-Biermann, A. Kucheryna, G. Bissky, and H. Willner. New ionic liquids with tris(perfluoroalkyl)trifluorophosphate (FAP) anions. *J. Fluorine Chem.*, **126** 1150–1159, (2005). See p. 18, 35, 38, 40

[19] P. Walden. Über den Zustand geschmolzener Salze. *Z. Phys. Chem.*, **157** 389–421, (1931). See p. 19

[20] *Handbook of Chemistry and Physics*. CRC Press LLC, http://www.hbcpnetbase.com/, 78. edition, (2008). See p. 19

[21] L. S. Garca-Coln, L. F. del Castillo, and P. Goldstein. Theoretical basis for the Vogel-Fulcher-Tammann equation. *Phys. Rev. B*, **40** 7040–7044, (1989). See p. 19

[22] J. P. Hansen and I. R. McDonald. Self-diffusion and electrical conductance in a simple molten salt. *J. Phys. C: Solid State Phys.*, **7** L384, (1974). See p. 19

[23] H. Tokuda, K. Hayamizu, K. Ishii, M. Abu Bin Hasan Susan, and M. Watanabe. Physicochemical Properties and Structures of Room Temperature Ionic Liquids. 1. Variation of Anionic Species. *J. Phys. Chem. B*, **108**, (2004). See p. 19

[24] R. F. de Souza, J. C. Padilha, R. S. Goncalves, and J. Dupont. Room temperature dialkylimidazolium ionic liquid-based fuel cells. *Electrochem. Commun.*, **5** 728, (2003). See p. 19

[25] U. Bach, D. Lupo, P. Comte, J. E. Moser, F. Weissortel, J. Salbeck, H. Spreitzer, and M. Grätzel. Solid-state dye-sensitized mesoporous TiO_2 solar cells with high photon-to-electron conversion efficiencies. *Nature*, **395** 583, (1998). See p. 19

[26] P. Wang, Q. Dai, S. Zakeeruddin, M. Forsyth, D. MacFarlane, and M. Grätzel. Ambient Temperature Plastic Crystal Electrolyte for Efficient, All-Solid-State Dye-Sensitized Solar Cell. *J. Am. Chem. Soc.*, **126** 13590–13591, (2004). See p. 19

[27] T. Predel, E. Schlücker, P. Wasserscheid, D. Gerhard, and W. Arlt. Ionic Liquids as Operating Fluids in High Pressure Applications. *Chem. Eng. Technol.*, **30** 1475–1480, (2007). See p. 19

[28] B. R. Hinderliter, K. N. Allahar, G. P. Bierwagen, D. E. Tallman, and S. G. Croll. Thermal Cycling of Epoxy Coatings Using Room Temperature Ionic Liquids. *J. Electrochem. Soc.*, **155** C93–C100, (2008). See p. 19

[29] D. S. Silvester and R. G. R. G. Compton. Electrochemistry in Room Temperature Ionic Liquids: A Review and Some Possible Applications. *Z. Phys. Chem.*, **220** 1247, (2006). See p. 19

[30] S. Ono, S. Seki, R. Hirahara, Y. Tominari, and J. Takeya. High-mobility, low-power, and fast-switching organic field-effect transistors with ionic liquids. *Appl. Phys. Lett.*, **92** 103313, (2008). See p. 19

[31] A. Fernicola, B. Scrosati, and H. Ohno. Potentialities of ionic liquids as new electrolyte media in advanced electrochemical devices. *Ionics*, **12** 95–102, (2006). See p. 19

[32] N. V. Plechkova and K. R. Seddon. Applications of ionic liquids in the chemical industry. *Chem. Soc. Rev.*, **37** 123–50, (2008). See p. 20

[33] P. Wasserscheid and T. Welton. *Ionic Liquids in Synthesis*. WILEY-VCH , Weinheim, (2008). See p. 20

[34] T. Welton. Ionic liquids in catalysis. *Coord. Chem. Rev.*, **248** 2459, (2004). See p. 20

[35] T. L. Beck, M. E. Paulatis, and L. R. Pratt. *The Potential Distribution Theorem and Models of Molecular Solutions*. Cambridge University Press, Cambridge, UK, (2006). See p. 22

[36] M. Deetlefs, C. Hardacre, M. Nieuwenhuyzen, A. H. Padua, O. Sheppard, and A. K. Soper. Liquid Structure of the Ionic Liquid 1,3-Dimethylimidazolium Bis{(trifluoromethyl)sulfonyl}amide. *J. Phys. Chem. B*, **110** 12055, (2006). See p. 24, 25, 36

[37] C. Hardacre, J. D. Holbrey, M. Nieuwenhuyzen, and T. G. A. Youngs. Structure and solvation in ionic liquids. *Acc. Chem. Res.*, **40** 1146–55, (2007). See p. 24

[38] C. Hardacre, S. McMath, D. Bowron, and A. Soper. Structure of molten 1,3-dimethylimidazolium chloride using neutron diffraction. *J. Chem. Phys.*, **118** 273–278, (2003). See p. 24, 25

[39] B. L. Bhargava, M. L. Klein, and S. Balasubramanian. Structural correlations and charge ordering in a room-temperature ionic liquid. *ChemPhysChem*, **9** 67–70, (2008). See p. 24

[40] G. Hura, J. Sorenson, R. Glaeser, and T. Head-Gordon. A high-quality x-ray scattering experiment on liquid water at ambient conditions. *J. Chem. Phys.*, **113** 9140–9148, (2000). See p. 24

[41] T. Fujimori, K. Fuji, R. Kanzaki, K. Chiba, H. Yamamoto, Y. Umebayashi, and S. Ishiguro. Conformational structure of room temperature ionic liquid N-butyl-N-methyl-pyrrolidinium bis(trifluoromethanesulfonyl) imide – Raman spectroscopic study and DFT calculations. *J. Mol. Liq.*, **131-132** 216–224, (2007). See p. 25, 38

[42] A. Triolo, A. Mandanici, O. Russina, V. Rodriguez-Mora, M. Cutroni, C. Hardacre, M. Nieuwenhuyzen, H. Bleif, L. Keller, and M. Ramos. Thermodynamics, Structure, and Dynamics in Room Temperature Ionic Liquids: The Case of 1-Butyl-3-methyl Imidazolium Hexafluorophosphate ([bmim][PF6]). *J. Phys. Chem. B*, **110** 21357–21364, (2006). See p. 24

[43] A. D. Graves and D. Inman. The electrical double layer in molten salts, Part 2. The double-layer capacitance. *J. Electroanal. Chem.*, **25** 357–372, (1970). See p. 26

[44] F. H. Stillinger and J. G. Kirkwood. Theory of the Diffuse Double Layer. *J. Chem. Phys.*, **33** 1282–1290, (1960). See p. 26

[45] M. J. Regan, E. H. Kawamoto, S. Lee, P. S. Pershan, N. Maskil, M. Deutsch, O. M. Magnussen, B. M. Ocko, and L. E. Berman. Surface Layering in Liquid Gallium: An X-Ray Reflectivity Study. *Phys. Rev. Lett.*, **75** 2498–2501, Sep (1995). See p. 28, 29, 75

[46] W. J. Huisman, J. F. Peters, M. J. Zwanenburg, S. A. de Vries, T. E. Derry, D. Abernathy, and J. F. van der Veen. Layering of a liquid metal in contact with a hard wall. *Nature*, **390** 379–381, (1997). See p. 28, 29

[47] L. Cheng, P. Fenter, K. L. Nagy, M. L. Schlegel, and N. C. Sturchio. Molecular-Scale Density Oscillations in Water Adjacent to a Mica Surface. *Phys. Rev. Lett.*, **87** 156103, (2001). See p. 28

[48] F. F. Abraham. The interfacial density profile of a Lennard-Jones fluid in contact with a (100) Lennard-Jones wall and its relationship to idealized fluid/wall systems: A Monte Carlo simulation. *J. Chem. Phys.*, **68** 3713–3716, (1978). See p. 28

[49] O. M. Magnussen, B. M. Ocko, M. J. Regan, K. Penanen, P. S. Pershan, and M. Deutsch. X-Ray Reflectivity Measurements of Surface Layering in Liquid Mercury. *Phys. Rev. Lett.*, **74** 4444–4447, (1995). See p. 28, 75

[50] W. A. Curtin. Density-functional theory of the solid-liquid interface. *Phys. Rev. Lett.*, **59** 1228–1231, (1987). See p. 28

[51] G. A. Chapela, G. Saville, S. M. Thompson, and J.S. Rowlinson. Computer simulation of a gas-liquid surface. Part 1. *J. Chem. Soc., Faraday Trans.*, **73** 1133–1144, (1977). See p. 28

[52] A. Braslau, P. S. Pershan, G. Swislow, B. M. Ocko, and J. Als-Nielsen. Capillary waves on the surface of simple liquids measured by x-ray reflectivity. *Phys. Rev. A*, **38** 2457–2473, (1988). See p. 28

[53] B. M. Ocko, X. Z. Wu, E.B. Sirota, S. K. Sinha, and M. Deutsch. X-ray reflectivity study of thermal capillary waves on liquid surfaces. *Phys. Rev. Lett.*, **72** 242–245, (1994). See p. 28

[54] C.-J. Yu, A. G. Richter, A. Datta, M. K. Durbin, and P. Dutt. Observation of Molecular Layering in Thin Liquid Films Using X-Ray Reflectivity. *Phys. Rev. Lett.*, **82** 2326–2329, (1999). See p. 28

[55] D. Beysens and M. Robert. Thickness of fluid interfaces near the critical point from optical reflectivity measurements. *J. Chem. Phys.*, **87** 3056–3061, (1987). See p. 29

[56] E. Sloutskin, B. Ocko, L. Tamam, I. Kuzmenko, T. Gog, and M. Deutsch. Surface Layering in Ionic Liquids: An X-ray Reflectivity Study. *J. Am. Chem. Soc.*, **127** 7796–7804, (2005). See p. 30

[57] J. Bowers, M. C. Vergara-Gutierrez, and J. R. Webster. Surface Ordering of Amphiphilic Ionic Liquids. *Langmuir*, **20** 309, (2004). See p. 30

[58] C. Santos and S. Baldelli. Surface Orientation of 1-Methyl-, 1-Ethyl-, and 1-Butyl-3-methylimidazolium Methyl Sulfate as Probed by Sum-Frequency Generation Vibrational Spectroscopy. *J. Phys. Chem. B*, **111** 4715–4723, (2007). See p. 29

[59] S. Rivera-Rubero and S. Baldelli. Surface Characterization of 1-Butyl-3-methylimidazolium Br^-, I^-, PF_6^-, BF_4^-, $(CF_3SO_2)_2N^-$, SCN^-, $CH_3SO_3^-$, $CH_3SO_4^-$, and $(CN)_2N^-$ Ionic Liquids by Sum Frequency Generation. *J. Phys. Chem. B*, **110** 4756–4765, (2006). See p. 29

[60] T. Iimori, T. Iwahashi, K. Kanai, K. Seki, J. Sung, D. Kim, H. Hamaguchi, and Y. Ouchi. Local structure at the air/liquid interface of room-temperature ionic liquids probed by infrared-visible sum frequency generation vibrational spectroscopy: 1-alkyl-3-methylimidazolium tetrafluoroborates. *J. Phys. Chem. B*, **111** 4860–6, (2007). See p. 29

[61] V. Lockett, R. Sedev, C. Bassell, and J. Ralston. Angle-resolved X-ray photoelectron spectroscopy of the surface of imidazolium ionic liquids. *Phys. Chem. Chem. Phys.*, **10** 1330, (2008). See p. 29, 103, 115

[62] G. Law, P. Watson, A. Carmichael, and K. Seddon. Molecular composition and orientation at the surface of room-temperature ionic liquids: Effect of molecular structure. *Phys. Chem. Chem. Phys.*, **3** 2879–2885, (2001). See p. 30

[63] G. Law and P. Watson. Surface orientation in ionic liquids. *Chem. Phys. Lett.*, **345** 1–4, (2001). See p. 30

[64] T. Gannon, G. Law, P. Watson, A. Carmichael, and K. Seddon. First Observation of Molecular Composition and Orientation at the Surface of a Room-Temperature Ionic Liquid. *Langmuir*, **15** 8429–8434, (1999). See p. 30

[65] B. Bhargava and S. Balasubramanian. Layering at an Ionic Liquid-Vapor Interface: A Molecular Dynamics Simulation Study of [bmim][PF6]. *J. Am. Chem. Soc.*, **128** 10073–10078, (2006). See p. 30

[66] R. M. Lynden-Bell and M. Del Pópolo. Simulation of the surface structure of butyl-methylimidazolium ionic liquids. *Phys. Chem. Chem. Phys.*, **8** 949–54, (2006). See p. 30

[67] E. Sloutskin, R. Lynden-Bell, S. Balasubramanian, and M. Deutsch. The surface structure of ionic liquids: Comparing simulations with x-ray measurements. *J. Chem. Phys.*, **125** 174715–174715, (2006). See p. 30

[68] G. Luo, S. Malkova, J. Yoon, D. G. Schultz, B. Lin, M. Meron, I. Benjamin, P. Vanysek, and M. L. Schlossman. Ion distributions near a liquid-liquid interface. *Science*, **311** 216–8, (2006). See p. 31

[69] C. Aliaga, C. Santos, and S. Baldelli. Surface chemistry of room-temperature ionic liquids. *Phys. Chem. Chem. Phys.*, **9** 3683–3700, (2007). See p. 31, 42, 103

[70] C. Romero and S. Baldelli. Sum Frequency Generation Study of the Room-Temperature Ionic Liquids/Quartz Interface. *J. Phys. Chem. B*, **110** 6213–6223, (2006). See p. 31

[71] C. Romero, H. Moore, T. Lee, and S. Baldelli. Orientation of 1-Butyl-3-methylimidazolium Based Ionic Liquids at a Hydrophobic Quartz Interface Using Sum Frequency Generation Spectroscopy. *J. Phys. Chem. C*, **111** 240–247, (2007). See p. 31

[72] J. Rollins, B. Fitchett, and J. Conboy. Structure and Orientation of the Imidazolium Cation at the Room-Temperature Ionic Liquid/SiO2 Interface Measured by Sum-Frequency Vibrational Spectroscopy. *J. Phys. Chem. B*, **111** 4990–4999, (2007). See p. 31

[73] B. D. Fitchett and J. C. Conboy. Structure of the Room-Temperature Ionic Liquid/SiO2 Interface Studied by Sum-Frequency Vibrational Spectroscopy. *J. Phys. Chem. B*, **108** 20255, (2004). See p. 31

[74] C. Aliaga and S. Baldelli. A Sum Frequency Generation Study of the Room-Temperature Ionic Liquid-Titanium Dioxide Interface. *J. Phys. Chem. C*, **112** 3064, (2008). See p. 31

[75] S. Rivera-Rubero and S. Baldelli. Surface Spectroscopy of Room-temperature Ionic Liquids on a Platinum Electrode: A Sum Frequency Generation Study. *J. Phys. Chem. B*, **108** 15133, (2004). See p. 31

[76] N. Nanbu, Y. Sasaki, and F. Kitamura. In situ FT-IR spectroscopic observation of a room-temperature molten salt | gold electrode interphase. *Electrochem. Commun.*, **5** 383, (2003). See p. 31

[77] R. Atkin and G. G. Warr. Structure in Confined Room-Temperature Ionic Liquids. *J. Phys. Chem. C*, **111** 5162, (2007). See p. 31, 32

[78] A. J. Carmichael, C. Hardacre, J. D. Holbrey, M. Nieuwenhuyzen, and K. R.Seddon. Molecular layering and local order in thin films of 1-alkyl-3-methylimidazolium ionic liquids using X-ray reflectivity. *Mol. Phys.*, **99** 795, (2001). See p. 31, 32, 97

[79] S. Chen, G. Wu, M. Sha, and S. Huang. Transition of ionic liquid [bmim][PF6] from liquid to high-melting-point crystal when confined in multiwalled carbon nanotubes. *J. Am. Chem. Soc.*, **129** 2416–7, (2007). See p. 31

[80] S. Maolin, Z. Fuchun, W. Guozhong, F. Haiping, W. Chunlei, C. Shimou, Z. Yi, and H. Jun. Ordering layers of $[\text{bmim}][\text{PF}_6]$ ionic liquid on graphite surfaces: molecular dynamics simulation. *J. Chem. Phys.*, **128** 134504, (2008). See p. 32, 33

[81] C. Pinilla, M. G. Del Pópolo, J. Kohanoff, and R. M. Lynden-Bell. Polarization relaxation in an ionic liquid confined between electrified walls. *J. Phys. Chem. B*, **111** 4877–84, (2007). See p. 32, 33

[82] R. M. Lynden-Bell, M. G. Del Pópolo, T. G. A. Youngs, J. Kohanoff, C. G. Hanke, J. B. Harper, and C. C. Pinilla. Simulations of ionic liquids, solutions, and surfaces. *Acc. Chem. Res.*, **40** 1138–45, (2007). See p. 31, 109

[83] B. L. Bhargava, S. Balasubramanian, and M. L. Klein. Modelling room temperature ionic liquids. *Chem. Commun.*, pages 3339–51, (2008). See p. 31

[84] O. J. Lanning and P. A. Madden. Screening at a Charged Surface by a Molten Salt. *J. Phys. Chem. B*, **108** 11069, (2004). See p. 33

[85] S. K. Reed, O. J. Lanning, and P. A. Madden. Electrochemical interface between an ionic liquid and a model metallic electrode. *J. Chem. Phys.*, **126** 084704, (2007). See p. 33

[86] L. Liu, S. Li, Z. Cao, Y. Peng, G. Li, T. Yan, and X.-P. Gao. Well-Ordered Structure at Ionic Liquid/Rutile (110) Interface. *J. Phys. Chem. C*, **111** 12161, (2007). See p. 33

[87] C. Pinilla, M. G. Del Pópolo, R. M. Lynden-Bell, and J. Kohanoff. Structure and dynamics of a confined ionic liquid. topics of relevance to dye-sensitized solar cells. *J. Phys. Chem. B*, **109** 17922–7, (2005). See p. 33

[88] P. Madden. private communication. (2008). See p. 33

[89] S. Schramm. Density profiles of Ionic Liquids at a Hard Wall. Diploma thesis, Institut für Theoretische und Angewandte Physik der Universität Stuttgart, (2008). See p. 35, 61, 63, 72, 97, 103

[90] F. Endres. Ionic Liquids: Promising Solvents for Electrochemistry. *Z. Phys. Chem.*, **218** 255, (2004). See p. 35

[91] S. Zhang, N. Sun, X. He, X. Lu, and X. Zhang. Physical Properties of Ionic Liquids: Database and Evaluation. *J. Phys. Chem. Ref. Data*, **35** 1475, (2006). See p. 38

[92] L. Carballeira, I. Perez-Juste, and C. van Alsenoy. Theoretical Study of Pyrrolidine: Revised Conformational Energies and Vibrational Assignments. *J. Phys. Chem. A*, **106** 3873, (2002). See p. 36

[93] P. v. R. Schleyer. Introduction: Aromaticity. *Chem. Rev.*, **101** 1115, (2001). See p. 39

[94] P. v. R. Schleyer. Introduction: Delocalization-Pi and Sigma. *Chem. Rev.*, **105** 3433, (2005). See p. 39

[95] J. D. Holbrey, W. M. Reichert, M. Nieuwenhuyzen, S. Johnson, K. R. Seddon, and R. D. Rogers. Crystal polymorphism in 1-butyl-3-methylimidazolium halides: supporting ionic liquid formation by inhibition of crystallization. *Chem. Commun.*, page 1636, (2003). See p. 39

[96] S. Hayashi, R. Ozawa, and H. Hamaguchi. Raman Spectra, Crystal Polymorphism, and Structure of a Prototype Ionic-liquid [bmim]Cl. *Chem. Lett.*, **32** 498, (2003). See p. 39

[97] R. W. Berg, M. Deetlefs, K. R. Seddon, I. Shim, and J. M. Thompson. Raman and ab Initio Studies of Simple and Binary 1-Alkyl-3-methylimidazolium Ionic Liquids. *J. Phys. Chem. B*, **109** 19018, (2005). See p. 39

[98] G. H. Wrodnigg, J. O. Besenhard, and M. Winter. Cyclic and acyclic sulfites: new solvents and electrolyte additives for lithium ion batteries with graphitic anodes? *J. Power Sources*, **97-98** 592–595, (2001). See p. 40

[99] D. L. Foster, W. K. Behl, and J. Wolfenstine. The effect of various electrolyte additives on reversible Li-graphite intercalation. *J. Power Sources*, **85** 299, (2000). See p. 40

[100] Y. J. Kim, Y. Matsuzawa, S. Ozaki, K. C. Park, C. Kim, M. Endo, H. Yoshida, G. Masuda, T. Sato, and M. S. Dresselhaus. High Energy-Density Capacitor Based on Ammonium Salt Type Ionic Liquids and Their Mixing Effect by Propylene Carbonate. *J. Electrochem. Soc.*, **152** A710, (2005). See p. 40

[101] T. Nishida, Y. Tashiro, and M. Yamamoto. Physical and electrochemical properties of 1-alkyl-3-methylimidazolium tetrafluoroborate for electrolyte. *J. Fluorine Chem.*, **120** 135, (2003). See p. 40

[102] A. Jarosik, S. R. Krajewski, A. Lewandowski, and P. Radzimski. Conductivity of ionic liquids in mixtures. *J. Mol. Liq.*, **123** 43, (2006). See p. 40

[103] S. Millefiorini, A. Tkaczyk, R. Sedev, J. Efthimiadis, and J. Ralston. Electrowetting of Ionic Liquids. *J. Am. Chem. Soc.*, **128** 3098–3101, (2006). See p. 41, 42, 119

[104] J. Als-Nielsen and D. McMorrow. *Elements of Modern X-ray Physics*. John Wiley & Sons Ltd., Chichester, (2001). See p. 44, 50

[105] M. Tolan. *X-Ray Scattering from Soft-Matter Thin Films*. Springer, Berlin, (1999). See p. 44, 45, 50, 72

[106] T. Head-Gordon and G. Hura. Water Structure from Scattering Experiments and Simulation. *Chem. Rev.*, **102** 2651–2670, (2002). See p. 44

[107] B. L. Henke, E. M. Gullikson, and J. C. Davis. X-Ray Interactions: Photoabsorption, Scattering, Transmission, and Reflection at $E = 50 - 30,000\,\text{eV}$, $Z = 1 - 92$. *Atomic Data and Nuclear Data Tables*, **54** 181–342, (1993). See p. 45

[108] The NIST Reference on Constants, Units, and Uncertainty. *http://www.physics.nist.gov/cuu/*, (2006). See p. 45, 77

[109] C. T. Chantler. Detailed Tabulation of Atomic Form Factors, Photoelectric Absorption and Scattering Cross Section, and Mass Attenuation Coefficients in the Vicinity of Absorption Edges in the Soft X-Ray ($Z = 30 - 36$, $Z = 60 - 89$, $E = 0.1\,\mathrm{keV} - 10\,\mathrm{keV}$), Addressing Convergence Issues of Earlier Work. *J. Phys. Chem. Ref. Data*, **29** 597–1048, (2000). See p. 45

[110] H. Dosch. *Critical phenomena at Surfaces and Interfaces (Evanescent X-Ray and Neutron Scattering)*, volume 126 of *Springer Tracts in Modern Physics*. Springer, Berlin, Heidelberg, (1992). See p. 45

[111] J. D. Jackson. *Classical electrodynamics*. Wiley, New York, 3. edition, (1999). See p. 45

[112] D. K. G. de Boer and A. J. G. Leenaers. Probing interface roughness by X-ray scattering. *Physica B*, **221** 18–26, (1996). See p. 48

[113] L. Nevot and P. Croce. Characterization of surfaces by grazing x-ray reflection - Application to study of polishing of some silicate-glasses. *Rev. de Physique Appliquee*, **15** 761–779, (1980). See p. 48

[114] P. Beckmann and A. Spizzichino. *The scattering of Electromagnetic waves From Rough Sufaces*. Pergamon, New York, (1963). See p. 48

[115] L. G. Parratt. Surface Studies of Solids by Total Reflection of X-Rays. *Physical Review*, **95** 359–369, (1954). See p. 49

[116] H. Reichert, V. Honkimäki, A. Snigirev, S. Engemann, and H. Dosch. A new X-ray transmission-reflection scheme for the study of deeply buried interfaces using high-energy microbeams. *Physica B*, **336** 46–55, (2003). See p. 52

[117] S. Engemann. *Premelting at the ice–SiO$_2$ interface - A high-energy x-ray microbeam diffraction study*. PhD thesis, University of Stuttgart, Faculty of Mathematics and Physics, (2005). See p. 52, 72

[118] M. Mezger. *X-ray Studies of the Density Depletion at Hydrophobic Water-Solid Interfaces*. PhD thesis, University of Stuttgart, Faculty of Mathematics and Physics, (2008). See p. 52, 54, 56, 59

[119] S. Schöder. *Substrate-Dependence of teh Ice Premelting at Heterogeneous Interfaces: An X-Ray Scattering Study*. PhD thesis, University of Stuttgart, Faculty of Mathematics and Physics, (2008). See p. 52, 59

[120] P. Suortti, T. Buslaps, V. Honkimäki, M. Kretzschmer, M. Renier, and A. Shukla. Monochromators for High-Energy Synchrotron Radiation. *Z. Phys. Chem.*, **215** 1419–1435, (2001). See p. 52

[121] P. Suortti and C. Schulze. Fixed-exit monochromators for high-energy synchrotron radiation. *J. Synchrotron Rad.*, **2** 6–12, (1995). See p. 53

[122] B. Lengeler, C. Schroer, M. Richwin, J. Tümmler, M. Drakopoulos, A. Snigirev, and I. Snigireva. A microscope for hard x rays based on parabolic compound refractive lenses. *Appl. Phys. Lett.*, **74** 3924–3926, (1999). See p. 53

[123] S. Engemann, H. Reichert, H. Dosch, J. Bilgram, V. Honkimäki, and A. Snigirev. Interfacial Melting of Ice in Contact with SiO_2. *Phys. Rev. Lett.*, **92** 205701, (2004). See p. 54

[124] M. Mezger, H. Reichert, S. Schöder, J. Okasinski, H. Schröder, H. Dosch, D. Palms, J. Ralston, and V. Honkimäki. High-resolution in situ x-ray study of the hydrophobic gap at the water-octadecyl-trichlorosilane interface. *Proc. Natl. Acad. Sci. U.S.A.*, **103** 18401–4, (2006). See p. 54, 75

[125] L. H. Schwartz and J. B. Cohen. *Diffraction from Materials*. Academic Press, New York, (1977). See p. 56

[126] K. Fischer. Neues Verfahren zur maßanalytischen Bestimmung des Wassergehaltes von Flüssigkeiten und festen Körpern. *Angew. Chem. Int. Ed.*, **48** 394–396, (1935). See p. 60

[127] R. Schlink P. A. Bruttel. *Water determination by Karl Fischer Titration*. Metrohm AG, (2003). See p. 60

[128] W. H. Gitzen. *Alumina as a ceramic material*. The American Ceramic Society, (1970). See p. 63

[129] S. Luo and C. Wong. Effect of UV/Ozone Treatment on Surface Tension and Adhesion in Electronic Packaging. *IEEE Trans. Compon. Packag. Technol.*, **24** 43–49, (2001). See p. 63, 64

[130] P. J. Eng, T. P. Trainor, G. E. Brown, G. A. Waychunas, M. Newville, S. R. Sutton, and M. L. Rivers. Structure of the Hydrated Al_2O_3 (0001) Surface. *Science*, **288** 1029–1033, (2000). See p. 64

[131] J. Ahn and J. W. Rabalais. Composition and structure of the Al_2O_3 (0001)(1x1) surface. *Surf. Sci.*, **388** 121–131, (1997). See p. 64

[132] L. Pauling. *The Nature of the Chemical Bond*. Cornell University Press, 3. edition, (1960). See p. 64

[133] S. Yee, R.A. Oriani, and M. Stratmann. Application of a kelvin microprobe to the corrosion of metals in humid atmospheres. *J. Electrochem. Soc.*, **138** 55, (1991). See p. 65

[134] M. Pfeiffer, K. Leo, and N. Karl. Fermi level determination in organic thin films by the kelvin probe method. *japp*, **80** 6880, (1996). See p. 65

[135] J. H. Hubbel and S. M. Seltzer. Tables of X-Ray Mass Attenuation Coefficients and Mass Energy-Absorption Coefficients. Technical report, National Institute of Standards and Technology, (1996). http://physics.nist.gov/PhysRefData/XrayMassCoef/cover.html. See p. 68

[136] J. Corbett. Radiation damage, defects and surfaces. *Surf. Sci.*, **90** 205–239, (1979). See p. 68

[137] J. Fryer. Effect of temperature on radiation damage to aromatic organic molecules. *Ultramicroscopy*, **40** 163, (1992). See p. 69

[138] B. J. Ciliax, K. L. Kirk, and R. D. Leapman. Radiation damage of fluorinated organic compounds measured by parallel electron energy loss spectroscopy. *Ultramicroscopy*, **48** 13–25, (1993). See p. 69

[139] R. Egerton. Chemical measurements of radiation damage in organic samples at and below room temperature. *Ultramicroscopy*, **5** 521–523, (1980). See p. 69

[140] H. C. Box and H. G. Freund. Conformations of the Free Radical in Irradiated α-Aminoisobutyric Acid. *J. Chem. Phys.*, **44** 2345, (1966). See p. 69

[141] P. E. Gill. Algorithms for the Solution of the Nonlinear Least-Squares Problem. *SIAM Journal on Numerical Analysis*, **15** 977, (1978). See p. 75

[142] T. Weise. *Global Optimization Algorithms - Theory and Application*. Self-Published, Second. edition, sep 23, (2008). Online available at http://www.it-weise.de/. See p. 75

[143] L. Ingber. Simulated annealing: Practice versus theory. *Math. Comput. Model.*, **18** 29–57, (1993). See p. 75

[144] L. Ingber. Adaptive Simulated Annealing (ASA). http://www.ingber.com, (2004). See p. 75

[145] M. Mezger, H. Reichert, I. B. Ramsteiner, A. Udyansky, O. Shchyglo, V. N. Bugaev, H. Dosch, and V. Honkimäki. Temperature and concentration dependence of the effective pair interaction parameters in Ni-Pd from high-energy x-ray diffuse scattering. *Phys. Rev. B*, **73** 184206, (2006). See p. 75

[146] M. J. Regan, P. S. Pershan, O. M. Magnussen, B. M. Ocko, M. Deutsch, and L. E. Berman. X-ray reflectivity studies of liquid metal and alloy surfaces. *Phys. Rev. B*, **55** 15874–15884, (1997). See p. 75

[147] O. M. Magnussen, B. M. Ocko, M. Deutsch, M. J. Regan, P. S. Pershan, D. Abernathy, G. Grübel, and J.-F. Legrand. Self-assembly of organic films on a liquid metal. *Nature*, **384** 250, (1996). See p. 75

[148] K. Nishikawa, Y. Sakamoto, and T. Iijima. Accuracy of intensity measurement by use of an area detector with a photostimulable phosphor screen, as confirmed by measuring scattering intensity from a liquid. *Jpn. J. Appl. Phys.*, **30** 1303–1306, (1991). See p. 77

[149] A. van Oosterom and J. Strackee. The Solid Angle of a Plane Triangle. *IEEE Trans. Biomed. Eng.*, **30** 125, (1983). See p. 78

[150] R. Fletcher. *Practical methods of optimization*. Wiley, New York, 2. edition, (1987). See p. 86

[151] P. A. Hunt, B. Kirchner, and T. Welton. Characterising the electronic structure of ionic liquids: an examination of the 1-butyl-3-methylimidazolium chloride ion pair. *Chemistry (Weinheim an der Bergstrasse, Germany)*, **12** 6762–75, (2006). See p. 95

[152] S. Fukuda, M. Takeuchi, K. Fujii, R. Kanzaki, T. Takamuku, K. Chiba, H. Yamamoto, Y. Umebayashi, and S. Ishiguro. Liquid structure of n-butyl-n-methylpyrrolidinium bis-(trifluoromethanesulfonyl) amide ionic liquid studied by large angle x-ray scattering and molecular dynamics simulations. *J. Mol. Liq.*, **143** 2, (2008). See p. 100

[153] O. Borodin and G. D. Smith. Structure and dynamics of N-methyl-N-propylpyrrolidinium bis(trifluoromethanesulfonyl)imide ionic liquid from molecular dynamics simulations. *J. Phys. Chem. B*, **110** 11481–90, (2006). See p. 100

[154] K. Fujii, Y. Soejima, Y. Kyoshoin, S. Fukuda, R. Kanzaki, Y. Umebayashi, T. Yamaguchi, S. Ishiguro, and T. Takamuku. Liquid structure of room-temperature ionic liquid, 1-Ethyl-3-methylimidazolium bis-(trifluoromethanesulfonyl) imide. *J. Phys. Chem. B*, **112** 4329–36, (2008). See p. 100

[155] M. G. Del Pópolo and G. A. Voth. On the Structure and Dynamics of Ionic Liquids. *J. Phys. Chem. B*, pages 1744–1752, (2004). See p. 101

[156] S. Baldelli. Probing electric fields at the ionic liquid-electrode interface using sum frequency generation spectroscopy and electrochemistry. *J. Phys. Chem. B*, **109** 13049–51, (2005). See p. 102, 103

[157] A. A. Kornyshev. Double-layer in ionic liquids: paradigm change? *J. Phys. Chem. B*, **111** 5545–57, (2007). See p. 102

[158] M. V. Fedorov and A. A. Kornyshev. Towards understanding the structure and capacitance of electrical double layer in ionic liquids. *Electrochim. Acta*, **53** 6835–6840, OCT 1 (2008). 58th Annual Meeting of the International-Society-of-Electrochemisty, Banff, CANADA, SEP 10-14, 2007. See p. 102

[159] M. V. Fedorov and A. A. Kornyshev. Ionic liquid near a charged wall: structure and capacitance of electrical double layer. *J. Phys. Chem. B*, **112** 11868–72, (2008). See p. 102, 115

[160] P. Keblinski, J. Eggebrecht, D. Wolf, and S. R. Phillpot. Molecular dynamics study of screening in ionic fluids. *J. Chem. Phys.*, **113** 282, (2000). See p. 103

[161] C. Wakai, A. Oleinikova, M. Ott, and H. Weingärtner. How polar are ionic liquids? Determination of the static dielectric constant of an imidazolium-based ionic liquid by microwave dielectric spectroscopy. *J. Phys. Chem. B*, **109** 17028–30, (2005). See p. 103

[162] M. Rovere and M. P. Tosi. Structure and dynamics of molten salts. *Rep. Prog. Phys.*, **49** 1001–1081, (1986). See p. 103

[163] M. Holovko, V. Kapko, D. Henderson, and D. Boda. On the influence of ionic association on the capacitance of an electrical double layer. *Chem. Phys. Lett.*, **341** 363368, (2001). See p. 103

[164] J. N. Canongia Lopes, M. F. Costa Gomes, and A. A. H. Pádua. Nonpolar, polar, and associating solutes in ionic liquids. *J. Phys. Chem. B*, **110** 16816–8, (2006). See p. 106, 108

[165] E. Gómez, N. Calvar, I. Domínguez, and A. Domínguez. Physical properties of the ternary mixture ethanol + water + 1-hexyl-3-methylimidazolium chloride at 298.15 K. *Phys. Chem. Liq.*, **44** 409–417, (2006). See p. 106

[166] C. S. Santos and S. Baldelli. Gas-Liquid Interface of Hydrophobic and Hydrophilic Room-Temperature Ionic Liquids and Benzene: Sum Frequency Generation and Surface Tension Studies. *J. Phys. Chem. C*, **112** 11459–11467, (2008). See p. 106

[167] A. A. H. Pádua, M. F. Costa Gomes, and J. N. A. Canongia Lopes. Molecular solutes in ionic liquids: a structural perspective. *Acc. Chem. Res.*, **40** 1087–96, (2007). See p. 108, 111

[168] J. N. A. Canongia Lopes and A. A. H. Pádua. Nanostructural organization in ionic liquids. *J. Phys. Chem. B*, **110** 3330–5, (2006). See p. 108

[169] J. Lachwa, P. Morgado, J. M. S. S. Esperana, H. J. R. Guedes, J. N. Canongia Lopes, and L. P. N. Rebelo. Fluid-Phase Behavior of {1-Hexyl-3-methylimidazolium

Bis(trifluoromethylsulfonyl) Imide, $[C_6mim][NTf_2]$, + C2-C8 n-Alcohol} Mixtures: Liquid-Liquid Equilibrium and Excess Volumes. *J. Chem. Eng. Data*, **51** 2215, (2006). See p. 108

[170] J. D. Holbrey, W. M. Reichert, M. Nieuwenhuyzen, O. Sheppard, C. Hardacre, and R. D. Rogers. Liquid clathrate formation in ionic liquid-aromatic mixtures. *Chem. Commun.*, page 476478, (2003). See p. 109

[171] M. Deetlefs, C. Hardacre, M. Nieuwenhuyzen, O. Sheppard, and A. K. Soper. Structure of ionic liquid-benzene mixtures. *J. Phys. Chem. B*, **109** 1593–8, (2005). See p. 109

[172] G. Raabe and J. Köhler. Thermodynamical and structural properties of binary mixtures of imidazolium chloride ionic liquids and alcohols from molecular simulation. *J. Chem. Phys.*, **129** 144503, (2008). See p. 109

[173] J. Deschamps, M. F. Costa Gomes, and A. A. H. Pádua. Molecular simulation study of interactions of carbon dioxide and water with ionic liquids. *ChemPhysChem*, **5** 1049–52, (2004). See p. 111

[174] Y. Shim, M. Y. Choi, and H. J. Kim. A molecular dynamics computer simulation study of room-temperature ionic liquids. I. Equilibrium solvation structure and free energetics. *J. Chem. Phys.*, **122** 44510, (2005). See p. 115

Danksagung

Mein Dank gilt allen, die mir beim Erarbeiten meiner Dissertation mit Rat und Hilfsbereitschaft zur Seite standen. Insbesondere danke ich

- Herrn Prof. Dr. Helmut Dosch für die Ermöglichung dieser Arbeit und Dr. Harald Reichert für die Betreuung derselben;

- Herrn Prof. Dr. Martin Dressel für die Übernahme des Mitberichts;

- Dr. Markus Mezger und Sebastian Schramm für die gute Zusammenarbeit auf dem Gebiet der ionischen Flüssigkeiten;

- Dr. Sebastian Schöder, Dr. John Okasinski, Dr. Sandrine Dourdain und Dr. Dmitry Kukuruznyak für die tatkräftige Unterstützung auf Messkampagnen wie daheim in Stuttgart;

- allen Mitarbeitern der ID15 um Dr. Veijo Honkimäkki und dem Leiter des Chemielabors der ESRF, Dr. Harald Müller;

- Prof. Dr. Moshe Deutsch, Dr. Benjamin Ocko, Dr. Roland Roth und Prof. Dr. Jörg Bilgram für die fruchtbaren Diskussionen und wertvollen Anregungen;

- Dr. János Major für viele Hinweise und die Hilfe bei der Nutzung des Rechenclusters;

- dem erstklassigen technischen Service am Max-Planck-Institut für Metallforschung in Person von Annette Weißhardt, Frank Adams, Arnold Weible, Thomas Meisner, Taufan Zimmer und Helmut Wendel;

- den Leitern der Glaswerkstatt, Helmut Kammerlander, und der mechanischen Werkstatt des ITAP, Michael Schäfer, und deren Mitarbeitern;

- Bekir Salgin, Dirk Vogel, Dr. Florin Turcu, Dr. Michael Rohwerder und Prof. Dr. Martin Stratmann vom Max-Planck-Institut für Eisenforschung für die erfolgreiche Kollaboration bei der Implementierung eines kombinierten Röntgen/Kelvinmethode-Versuchsaufbaus;

- Dr. Sarmimala Hore für die Vermittlung und Anna Jarosik für die Durchführung der Karl-Fischer-Titrationen;

145

- und allen anderen, die zum Gelingen dieser Arbeit beigetragen haben und an dieser Stelle von mir ohne Absicht vergessen worden sind.

Die Jahre am Max-Planck-Institut für Metallforschung waren lehrreich, aufregend und mitunter geprägt von hoher wissenschaftlicher Anspannung. Dass sie mir stets in freudiger Erinnerung bleiben werden, liegt nicht zuletzt an der ausgesprochen guten Atmosphäre innerhalb der Abteilung Dosch, wofür ich all deren Mitarbeitern herzlich danken möchte. Abgesehen von den oben bereits Erwähnten seien hier hervorgehoben: meine Bürokollegen Ruslan und Mélissa, Florian, Max, Vedran, Paulien, Felix und Moritz.

Zu guter letzt gebührt meiner Familie ein großes Dankeschön: meinen Eltern, derer Unterstützung ich mir stets gewiss sein konnte, meinem Bruder, meinen Schwiegereltern, Jan-Bernd, der mittlerweile auch irgendwie zur Familie gehört, und natürlich meiner Frau Eva und unserer Tochter Carlotta, die mir Kraft, Freude und Sinn geben.